TECHNISCHE UNIVERSITÄT MÜNCHEN

TUM School of Engineering and Design

Influence of the Lateral Superstructure Stiffness on the Vehicle Running Behaviour and on the Dynamic Response of the Track

Junyang Zhang

Vollständiger Abdruck der von der TUM School of Engineering and Design der Technischen Universität München zur Erlangung des akademischen Grades eines Doktors der Ingenieurwissenschaften genehmigten Dissertation

Vorsitz: Prof. Dr.-Ing. Rolf Moeckel

Prüfer der Dissertation:

1. Prof. Dr.-Ing. Stephan Freudenstein

2. Prof. Dr.-Ing. Sebastian Stichel

Die Dissertation wurde am 11.05.2021 bei der Technischen Universität München eingereicht und durch die TUM School of Engineering and Design am 09.11.2021 angenommen.

TABLE OF CONTENTS

I

Table of Contents

Abstract

The lateral rail track superstructure stiffness determines the distribution of the lateral wheel loads by the rail and the lateral loads acting on the rail supporting structure and its components. On the other hand, the resulting lateral displacement and rotation of the rail head is changing the rail-wheel contact geometry which is contributing to the characteristic running behaviour of the vehicle.

A numerical modelling and simulation chain with a wide range of applications was developed by this study. Its input data and validation were obtained from the laboratory tests, the field measurements performed in this study and from the previously conducted experiments described in the literature.

One of the developed numerical simulation tools, called the virtual fastening system test, is linking the laboratory test using a single fastening system loaded by a single contact force with the real track scenario. Simulations are showing that the rail head lateral displacements in the virtual laboratory testing tool following categories C, D and E as defined in the standard DIN EN 13481-2 [1] are all greater than under real vehicle-track interaction using the track scenario simulation tool. This confirms that the requirements for performing the laboratory tests are conservatively designed.

The simulations using the track scenario simulation tool and assuming good track geometry quality show that a fastening system with low lateral stiffness helps to better distribute the lateral loads and to reduce the lateral axle box accelerations, while a low rail rotational stiffness (e.g. by low/moderate clamping force) is increasing the lateral accelerations. Tension clamp preloads providing high rail rotational stiffness are beneficial to achieve a higher critical speed (maximum speed along straight section).

Using a stiff rail pad would be one of the most effective measures to limit the rail head lateral displacement, but this comes with a limitation of the vertical and the lateral load distribution.

A favourable solution is the use of a medium-stiff rail pad in combination with a higher tension clamp preload in narrow curves including the transitions, as done e. g. by ÖBB.

A low lateral sleeper support stiffness provided by a soft under-sleeper-pad is also reducing the lateral axle box accelerations. However, the effect on the elastic sleeper-track resistance needs to be considered

1. Introduction

1.1 Background of the research

The lateral track superstructure stiffness of a ballasted track is determined by its structural design defining its elasticity in relation to the wheel-rail contact forces. For standard track design it is influenced by the properties of the rail fastening system and the interface between sleeper and ballast. The lateral superstructure stiffness determines the load distribution by the rail and the loading acting on the superstructure and its components. It also influences the railhead displacement, which can change the wheel/rail contact geometry thus to change the vehicle running behaviour.

This study focusing on the influence of the lateral superstructure stiffness, beside vertical stiffness, on the vehicle running behaviour and the interacted forces caused by the wheel/rail contact on the superstructure.

Design of railway track superstructure using analytical or numerical tools requires detailed information of forces activated by train loads and of the track stiffness properties to demonstrate the load distribution and the stresses within the superstructure. The design has to integrate the vehicle performance to improve the entire rail system, which covers vehicle, track and its interaction effects. This requires a numerical modelling and simulation approach.

The main research content of this documentation is based on the (not published) final report [2] of a 3-year project funded by the Karl Vossloh Foundation (from 2018 to 2020).

1.2 Aims and achievements of the project

A numerical tool was developed to provide suggestions for the optimization of superstructure lateral stiffness and the relevant subsystems (e.g., components in the rail fastening system) with the following criteria:

- Influence of the superstructure lateral stiffness (at rail-sleeper and sleeper-ballast interfaces) on the running behavior of the vehicles (contact forces, axle box acceleration, running stability) in the real track conditions (track quality).

- Dynamic wheel/rail contact forces, depending on the lateral stiffness of the rail fastening system and the lateral sleeper support stiffness, at the same time under consideration of the track alignment, track quality (irregularities), and the real rail and wheel profiles.

- Load distribution into the superstructure, influenced by different superstructure stiffness combinations. Calculation of the deformations and stresses of the superstructure components e.g., rail and tension clamp under dynamic wheel-rail contact forces.

The developed numerical tool is a complex system and consists of many sub-models with full 3D models to fulfill the above-listed requirements. Figure 1 shows the overview of the workflow.
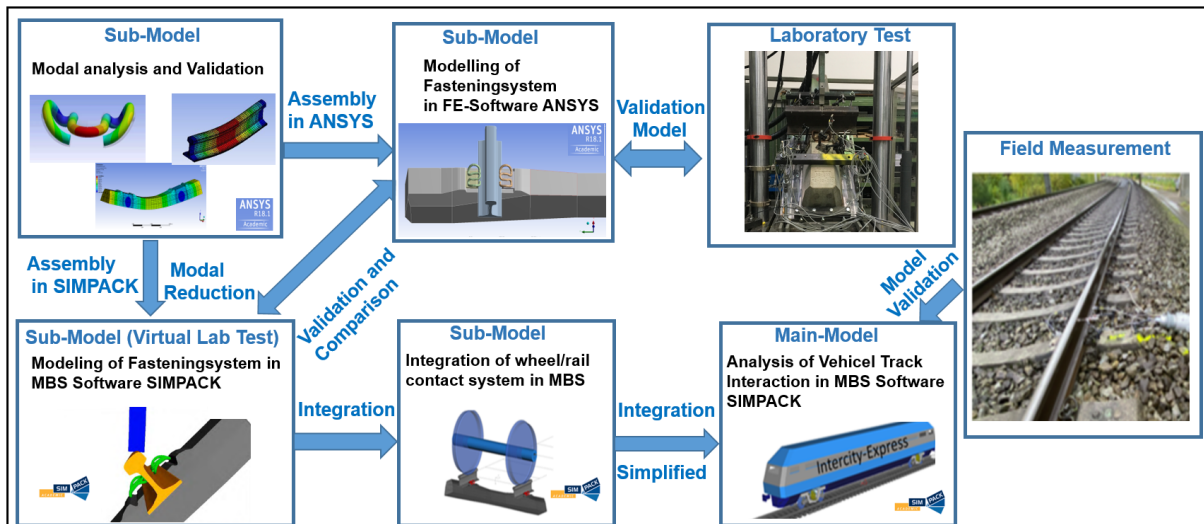

Figure 1: Workflow Overview of the developed numerical tools

1.3 General research approach

First, the numerical models of the superstructure components such as rail, sleeper, tension clamp, etc. are created in the 3D and validated by laboratory tests or using literature. The component assembly process is performed in the MBS software platform SIMPACK [3]. In parallel the fastening system is also set up in FE Software environment ANSYS [4]. Since the functionality for definition of contact conditions in SIMPACK and the ability to carry out the dynamic analysis specially under considering of the rail/wheel contact in ANSYS is limited, the MBS model created in SIMPACK was used to perform the dynamic analysis and the model created in ANSYS was used to check the correctness of boundary conditions in the MBS model.

The fastening system model was verified through different laboratory tests. With respect to further investigations the fastening system modelling workflow can be divided in two different approaches.

Using full 3D tension clamps. The model with a full 3D tension clamp for one support point was developed as a numerical tool that can be used for virtual laboratory tests according to the EN DIN13481-2 [1] standard. The influence of different component properties such as stiffness of rail pads, geometry-related tension clamp preload, and lateral stiffness of the angular guide plate can be determined. The virtual laboratory test showed a good relationship to the real laboratory test and to the real track scenarios. It can be used to optimize the fastening system, e.g. with respect to the tension clamp design (preload, stiffness and natural frequencies) and the stiffness combinations.

Using simplified tension clamps. The verified force and spring values activating the same lateral railhead displacement are replacing the 3D tension clamps. This approach is used for the further connection with rail/wheel contact model und its integration into the dynamic track/vehicle model.

To verify the correctness of the defined wheel-rail contact, a comparison was made between the equivalent conicity determined by the SIMPACK standard module (which cannot take into account the railhead displacement caused by rail rotation) and the model developed in this study.

The general vehicle model verification process (hunting behaviour, critical speed and derailment) was performed using two different vehicle design to examine the quality of the applied vehicle models and correctness of input.

Based on the validated wheel/rail contact model, the rail-wheel contact points were investigated under static conditions of railhead displacement to obtain a primary understanding of the contact mechanism. Static calculation means that the railhead lateral displacement is defined as a fixed value before starting the numeric calculation and the dynamic effect of the railhead lateral displacement during the train crossing cannot be considered. Using a time domain simulation, the complex wheel/rail contact interaction problem in relation to the vehicle running behaviour can be finally solved.

The test scenario of a train running on a curved track is one of the relevant situations. Due to the guidance mechanism of the wheel/rail contact, a significantly higher lateral force is activated along the curve, which results in a larger lateral railhead displacement. The track/vehicle dynamic model is able to determine the actual wheel/rail contact force, contact point and the dynamic interaction between the superstructure and vehicle.

The field measurements performed along the track section Redl/Zipf-Vöcklamarkt (ÖBB line Salzburg to Vienna) were used to validate the track/vehicle dynamic model, in which the vehicle, track alignment and different fastening systems were adjusted according to the measurements along the track section. Based on the through field measurement validated model, the typical train operation scenario with corresponding axle load, curve radius and vehicle speed defined by standard EN DIN 13481 from category C and E which cover the common and extreme load cases were used to perform the sensitive analysis. Different superstructure components such as rail pad, angular guide plate, tension clamp were considered. In addition, the influence of sleeper ballast lateral support stiffness under axle load was also investigated. The results from the model with rigid superstructure without any defined stiffness properties were also performed to give a comparison against the model which is considering the real superstructure stiffness.

The calculated rail/wheel contact forces from the vehicle–track simulation can also be transferred to the virtual laboratory model for comparison with the laboratory test according to the standard DIN EN 13481-2 [1].

On the vehicle side, the wheel/rail contact forces, wheel contact positions on the rail, wheelset lateral displacements and axle box accelerations were used as evaluation criteria.

For the straight track, the performance of the lateral interaction between vehicle and track was investigated. In this study, the linear critical speed which represents the properties of vehicle and wheel/rail contact was determined. Starting from this state, the nonlinear critical speed is used to specify the influence factor, which is considering the lateral superstructure stiffness.

2. Literature Review

2.1 State of the art and improvements through this study

Many research projects dealing with the equivalent conicity and the vehicle running behaviour under certain track geometry conditions (track alignment, track quality) are using Multi-Body Simulations (MBS) based on rigid track models or using simplified superstructure lateral stiffness to study the mechanism of railhead lateral displacement under wheel/rail contact forces [5], [6], [7], [8]. These simplifications are useful for general studies focusing on the vehicle running behaviour. But an evaluation of the track or the rail fastening stiffness with regard to the effect on the vehicle running behaviour and the corresponding load and stress distribution in the track components (e.g. fastening components) requires a full model which describes the detailed mechanisms in the sub-models "track" and "vehicle". Especially a model to study the relationship between the in-service conditions along the real track and the corresponding situation used for the approval test procedures for fastening systems such as EN DIN 13481-2 [1] is missing.

A diagram in [9] shows simulation results of the relationship between the lateral angle guide plate stiffness of the rail fastening and the critical speed of the vehicles for the straight track situation. The detail mechanism of the fastening system, such as the coupled effects of rail head ration caused by rail pad vertical support stiffness and of tension clamp preload on the running behaviour is now investigated by this study. The interaction mechanisms of fastening components, such as

1) the rail lateral resistance provided by angular guide plate, rail pad shear stiffness and tension clamp,

2) the rail rotational resistance provided by rail pad vertical stiffness, tension clamp preload and tension clamp stiffness,

are now modelled in a detail. A relationship is established linking the existing laboratory test used for the fastening system with the corresponding mechanism integrated into the vehicle/track model.

In documentation [10], many laboratory tests and field measurements were carried out and evaluated to investigate the wear reduction on narrow curves by considering of the lateral track

stiffness. Several essential conclusions were given, e.g. it is recommended that an increased clamping force should be used to control the lateral railhead movement.

Since lateral railhead movement and load distributions are also depended on the vertical rail support stiffness (e.g. vertical stiffness of rail pad influences rail rolling significantly). It is necessary to build the numerical model of the fastening system with consideration of the coupled mechanisms in lateral and vertical directions to obtain realistic results that are useful for the development of new components.

In [11], the vehicle-track interaction in the vertical direction is investigated under consideration of the whole vertical track stiffness and track geometry quality. The whole track superstructure (rail, fastening system, sleeper and ballast) is modelled as one linear beam-block which has only vertical modal motion ability.

In [12], numerous laboratory and filed measurements were conducted to investigate the influence of the rail fastening component on the lateral rail displacements and their load distribution. Some of the laboratory and field measurements in the documentation are referenced in this study as input or verification of the numerical modelling.

The documentations [13] [14] [15] [16] give systematic solutions for individual modelling of rail support, sleeper support and its validation through field measurement and laboratory test.

Many laboratory tests to study sleeper lateral resistance of padded or unpadded sleepers in unloaded situations have been investigated in documentation [17]. It helps to give a basic overview of the sleeper lateral resistance for this study.

A model based on the findings of [18] [19] [20] was developed in this study to consider the lateral sleeper resistance stiffness under axle load.

The tension clamp, which supplies the tension force to control the rail roll plays an important role in the railhead lateral displacement. Measurement results in documentation [21] (tension clamp type Skl 15) and [22] (tension clamp type Skl 14 and Skl 21) used for the investigation of the natural frequency behaviour are also used for validation of the model in this study. The modal analysis of the superstructure components (frequencies and modes) is the first step of the model process for superstructure components in this project (see the workflow in Figure 1).

2.2 Definition of terms and methods used in this thesis

2.2.1 Track quality and PSD

The definitions of the track related irregularities used in the simulation of this work are described in Figure 2, according to [23].
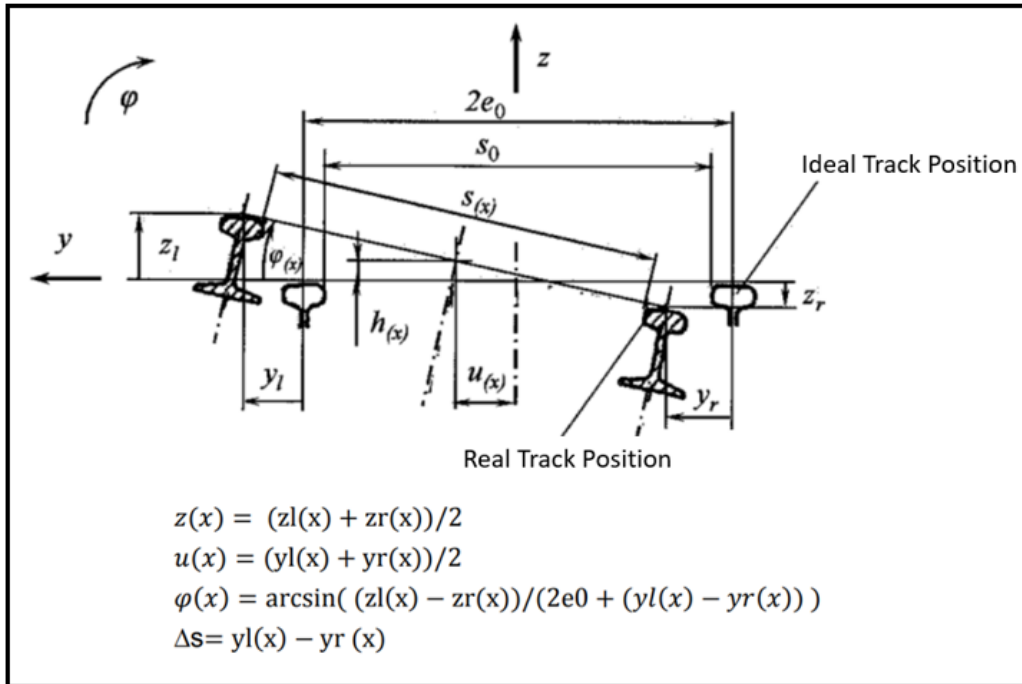

z(x) = (zl(x) + zr(x))/2
u(x) = (yl(x) + yr(x))/2
φ(x) = arcsin((zl(x) − zr(x))/(2e0 + (yl(x) − yr(x))))
Δs= yl(x) − yr (x)

Figure 2: Definitions of track irregularities according to [23]

The track irregularities demonstrated in the frequency domain and classified by PSD are converted into the distance domain track irregularities using the method in [3]. There are several PSD classifications used worldwide, they are summarized as:

- US: FRA DOT 49 CFR part 213 [24]
- China: China Changsha Rail Institute [25]
- China: China Peking Rail Institute [26]
- Germany: Frederich [27]
- Europe and Worldwide: EN 14363 [28] and UIC 518 [29]

In this work, the ERRI B 176 described in [3] is widely used as input for the whole track-vehicle dynamic model. The definition of the PSD classification is described in polynomials as follows:

Vertical: $\qquad Sv(\Omega) = \dfrac{A_v \bullet \Omega c^2}{(\Omega^2 + \Omega r^2) \bullet (\Omega^2 + \Omega c^2)}$ $\qquad$ in m^2/ (rad/m) $\qquad$ (Equation 1)

Lateral: $\qquad Sl(\Omega) = \dfrac{A_A \bullet \Omega c^2}{(\Omega^2 + \Omega r^2) \bullet (\Omega^2 + \Omega c^2)}$ $\qquad$ in m^2/ (rad/m) $\qquad$ (Equation 2)

Cross-Level: $S\varphi(\Omega) = \dfrac{A_v \bullet \Omega c^2 \bullet \Omega^2}{(\Omega^2 + \Omega r^2) \bullet (\Omega^2 + \Omega c^2) \bullet (\Omega^2 + \Omega s^2) \bullet e_0}$ in rad^2/ (rad/m) $\qquad$ (Equation 3)

Where

e_0, is the half distance between the two-wheel tread reference circles,

Ωc, Ωr, Ωs, are the limit frequencies,

Ωc = 0.8246 rad/m,

Ωr = 0.0206 rad/m,

Ωs = 0.4380 rad/m

Coefficient (e_0 =0.75)	Lower level (m rad)	Higher level (m rad)
A_v	4.032 10^{-7}	1.080 10^{-6}
A_A	2.119 10^{-7}	6.125 10^{-7}

2.2.2 CAD, FEM and MBS and modal analysis

In this study, the methods of CAD (the abbreviation of Computer-aided design) [30], FEM (the abbreviation of the finite element method) [31] and MBS (the abbreviation of multibody simulation) [32] were used to establish the whole modelling chain in a co-simulation workflow.

Vibration is a common phenomenon for any physical system. The frequencies at which vibration occur and the vibration shape for the particular frequency depends upon the physical property of the system. Such shapes the system undergoes, when excited at a frequency, results in the so called eigenmodes or normal modes. Modal analysis involves finding out the mode shapes at the corresponding frequencies and are performed through the respective APDL codes in ANSYS [4] in this study.

2.2.3 Modal reduction as used in CAD-FEM-MBS Co-Simulation

Figure 3 [3] shows, that the 3D geometries created by CAD environment, the meshing and the material properties are imported into the FEM environment. In this research they are describing the superstructure elements such as rail, sleeper and tension clamps. Through the modal reduction process, the corresponding files for import into the MBS system were created. In MBS system, e.g. in SIMPACK Software environment, the components will be assembled with the corresponding boundary conditions to fulfil the motion mechanisms for dynamic analysis. The model in MBS environment SIMPACK is a modal reduction from the original model in ANSYS in order to reduce the degrees of freedom to fulfil the limits set by the MBS system. In other words, the model in MBS is a simplified model from the FE model designed for the application of dynamic excitations and for the analysis of the dynamic responses with a suitable calculation effort. Therefore, the FE model had been first validated with the laboratory test and then used to verify the MBS model in SIMPACK (Figure 1; chapter 1.2).
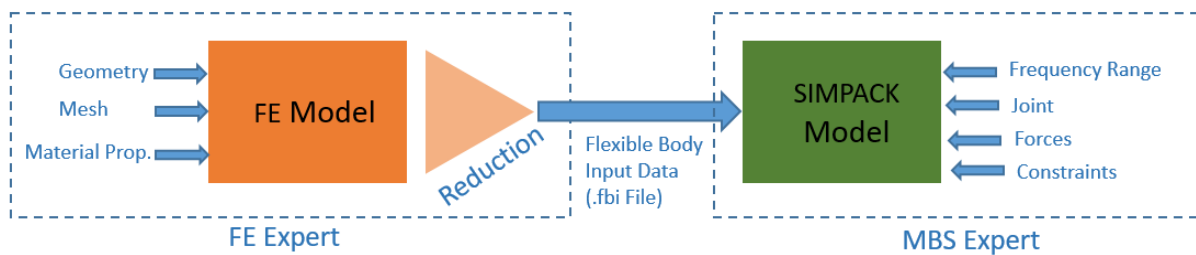

Figure 3: Modal reduction FE to MBS [3]

2.2.4 Ride comfort N_{MV} according to DIN EN 12299 and Wz index according to Sperling's method

There are two main methods to evaluate the passenger comfort worldwide in the application of railway technology, they are the mean value evaluation method according to DIN EN 12299 [33] and Wz index. The Wz index, which also called Sperling index, is a historical method developed in the first original description by Sperling in year 1941 [34] and is still used with the same name worldwide, especially in the non-European countries. One of the published definitions can be found in the documentation [5], the equations are described as follows:

$$W_z = \sqrt[10]{\int_{0.5}^{30} a(f)^3 B(f)^3 df} \qquad \text{(Equation 4)}$$

with

$a(f)$:　amplitude of the spectral component of the car body acceleration corresponding to frequency f

$B(f)$:　acceleration weighting factor

$$(f) = k\sqrt{\frac{1.911f^2+(0.25f^2)^2}{(1-0.277f^2)^2+(1.563f-0.0368f^3)^2}}$$　　　　(Equation 5)

with

　　k = 0.588 for vertical vibration

　　f : frequency of car body acceleration [Hz]

The method defined in DIN EN 12299 is widely used in Europe. In this study, the method defined in DIN EN 12299, so called mean value N_{MV}, was applied to perform the evaluation of the passenger comfort index. The formula was described as following:

$$N_{MV} = 6\sqrt{\left(a_{XP95}^{W_d}{}^2\right) + \left(a_{YP95}^{W_d}{}^2\right) + \left(a_{ZP95}^{W_d}{}^2\right)}$$　　　　(Equation 6)

the a_X, a_Y and a_Z is the root mean square of the longitudinal, lateral and vertical car body acceleration, 95 refers to the quantile of order 95%, and W_d is the weight filters of the longitudinal, lateral, and vertical acceleration.

2.2.5 Definition of RMS value

In this study, the RMS (Root Mean Square) filter was used to evaluate the lateral axle box acceleration. The definition of the RMS defined in [3] is as follows:

This method is summing of all given squared value y, averaging and taking the square root.

$$y_{rms} = \sqrt{\frac{1}{n-1} \sum_{i=1}^{n} (y_i)^2} \qquad \text{(Equation 7)}$$

3. Laboratory experimentation and input data for modelling of fastening system

Various laboratory tests on fastening systems and on the entire track superstructure system were carried out by [12], which can be directly used for input and validation of the model in this work focusing on lateral vehicle/track dynamics. However, this research still requires additional validation of the rail fastening system and its components, especially with respect to the non-linear behavior of rail head displacement under cyclic loading caused by the rail pad properties. This is essential to prepare the input for the time domain simulation in the MBS model. The laboratory tests for the required validation of the numerical models and for obtaining the input data for simulations were carried out at the institute of Road, Railway and Airfield Construction of TU Munich as part of the 3-years project (from 2018 to 2020) funded by the Karl Vossloh Foundation. Chapter 3.1and 3.2 describe the laboratory experimentation process.

3.1 Determination of vertical stiffness of rail pads

Different rail pads e.g., rail pad Zw 700, Zw 687, and Zw 1000, were studied. First, the static stiffness of the different rail pads was determined according to DBS 918 235:2017 [35]. Figure 4 shows the test set up and the test samples. The determined static stiffness of the different pads is shown in Figures 5, 6 and 7.
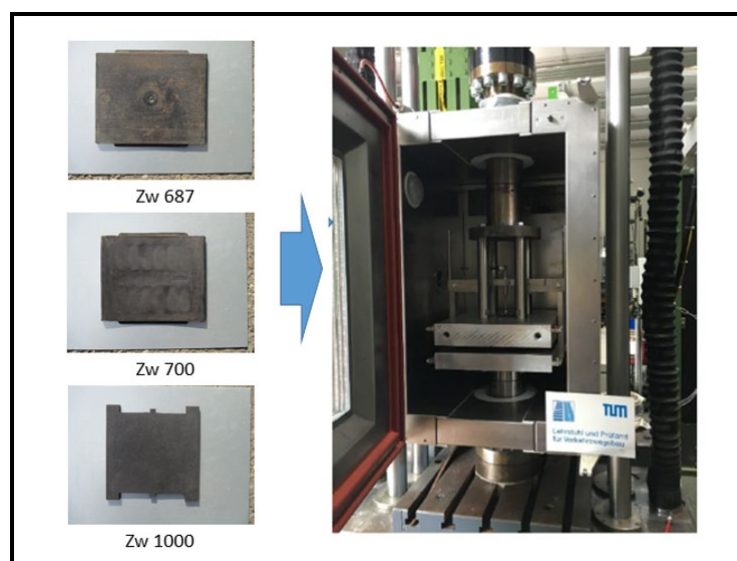

Figure 4: Test set up for the determination of rail pad stiffness and rail pad samples used for testing
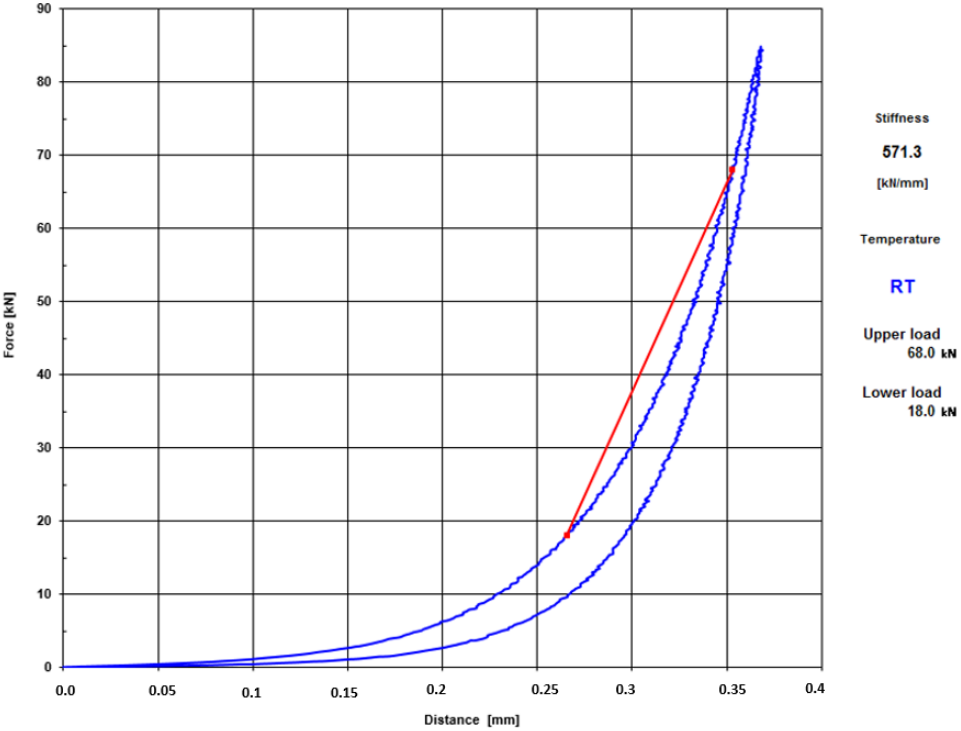
Figure 5: Static stiffness of rail pad Zw 687 according to DBS 918 235:2017
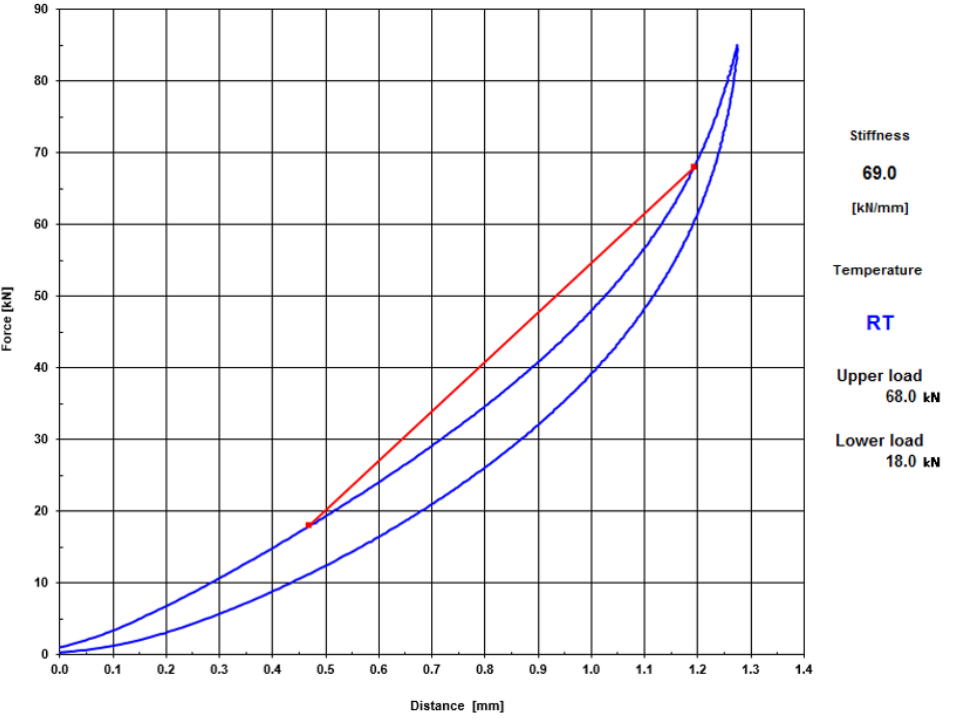
Figure 6: Static stiffness of rail pad Zw 700 according to DBS 918 235:2017
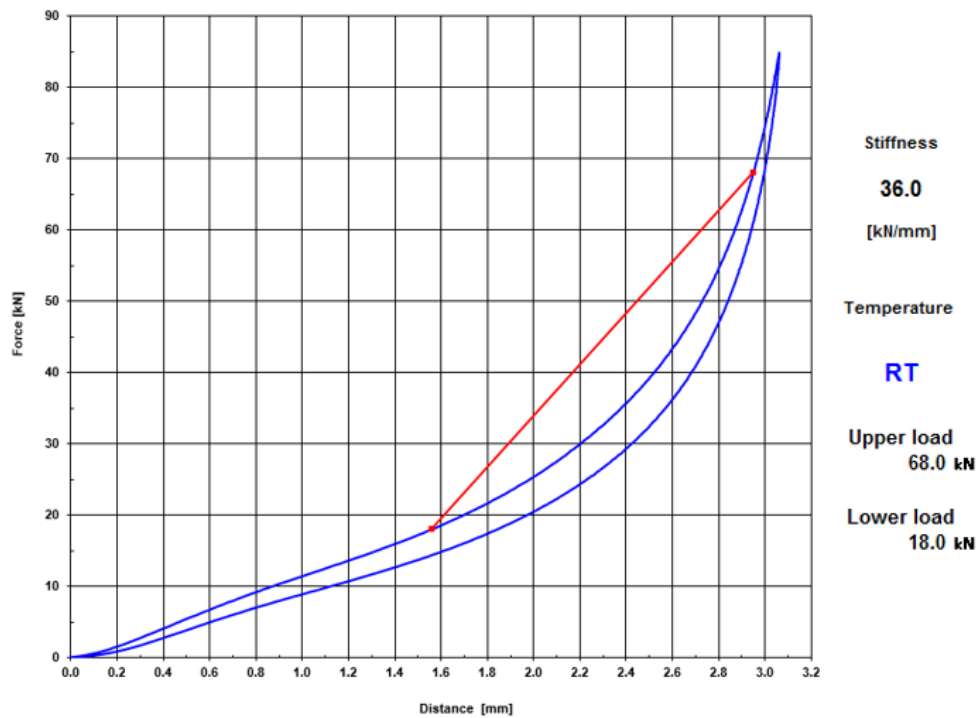
13

Figure 7: Static stiffness of rail pad Zw 1000 according to DBS 918 235:2017

Table 1 summarizes the linear vertical static stiffness calculated according to [35]. Although, for the numerical modelling in this study, the non-linear force-displacement characteristics of the rail pads were used. The linear secant stiffness of the three different rail pad are used for the overview.

Table 1: Summary of linear calculated vertical stiffness of different rail pads

Rail Pad Typ	Linear stiffness in kN/mm
Zw 1000	36
Zw 700	69
Zw 687	571

3.2 Laboratory test on rail fastening system

Vertical cylinder load on rail head with 45 degrees' angle

The interface between the superstructure and vehicle is the wheel/rail contact, which from the superstructure's point of view is directly influenced by the rail head movement.

The tests to investigate the influence of fastening system stiffness on the rail head displacement (caused by lateral and rotation movement of the rail) under angled applied load were conducted on a W 14 rail fastening system with Skl 14 tension clamps as shown in Figure 8. A section of a concrete sleeper type B 70 and a rail profile 60 E2 with a length of 550 mm is used for testing. The test sample (rail fastening system on sleeper) is placed at an angle of 45 degrees relative to the vertical hydraulic cylinder so that a respective lateral load is applied. Under using a 45 degrees' cylinder setting angle related to the rail head, it is resulted in a maximal lateral force/vertical force ration, namely, L/V=1, and to realise a maximal lateral rail head displacement under given loading. The strong non-linear behaviour of rail pad influences the rail displacement under the load, especial in the movement range before the rail foot has a contact with the tension clamp middle bend. The total 12 displacement transducers were installed to determine the vertical and the lateral displacements of the rail and of the tension clamps. The setup of the laboratory test was specially designed for the validation of lateral rail displacement in the FE model. Figure 8 shows the laboratory test setup.

The average values from the transducers on both rail sides were used. This non-linear rail head/foot displacements vs load diagram was determined through given a cylinder load from 0 to 20 kN. It is an important evidence to check the complex modelling mechanism and function considering the non-linear rail pad properties.
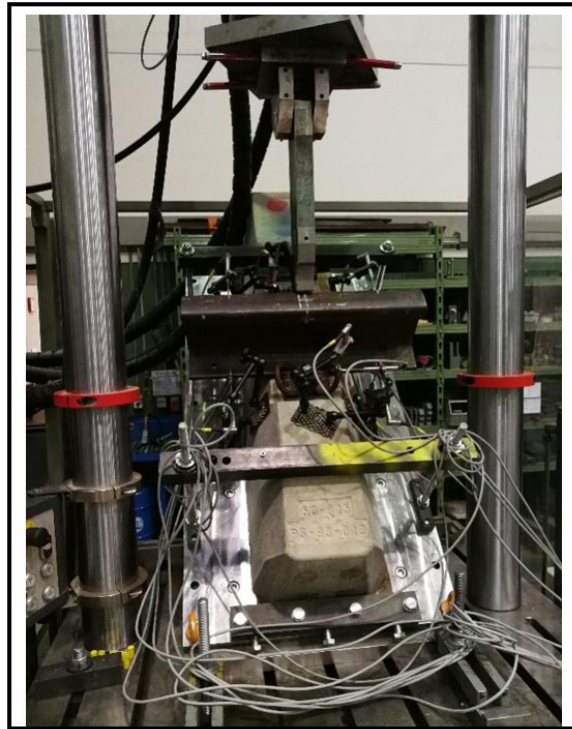
Figure 8: Laboratory test setup of the rail fastening system

Figure 9 shows the diagram of lateral rail head displacement vs vertical cylinder load in the loaded process with the tension clamp Skl 14 using different rail pads, Zw 700 (medium stiff) and Zw 687 (stiff). It should be noted that the results shown in Figure 9 were recorded after 10 loading cycles, so there is already contact between the rail foot and the angle guide plate.
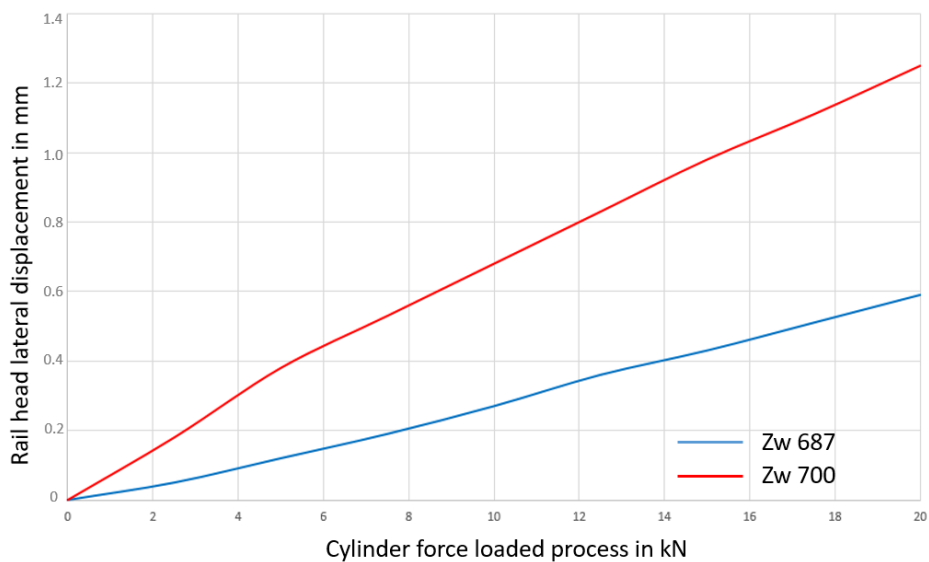

Figure 9: Rail head lateral displacement vs vertical cylinder load using different rail pads

More results gained from the laboratory tests can be found in appendix 1.

A higher cylinder load of 50 kN was also applied on the rail head to investigate the influence of contact between the middle bend of the clamp and the rail foot on the lateral rail head displacement. The test results show that for a large rail rational movement, the contact between the rail foot and tension clamp middle bend lead to a linear behaviour of the rail head lateral displacement with respect to the cylinder load (see appendix 2).

One of the tasks of this research is the calculation of displacement, stress and strain of components caused by loading. The fastening components such as the tension clamp were created as a complete 3D model to realize the geometry optimization. In order to determine the influence of each individual component such as rail pad, angle guide plate and tension clamps on the deformation behaviour of the whole system, a special fastening system using the combination of steel rail pad (not used in tracks) and steel angle guide plate was used as a reference base.

Figure 10 shows the situation of the reference fastening system using the steel angle guide plate and the steel rail pad to study the tension clamp stiffness characteristic isolated from elasticity activated by other components. By this test, the contribution of the tension clamp characteristic to the lateral railhead displacement under a certain load can be determined.
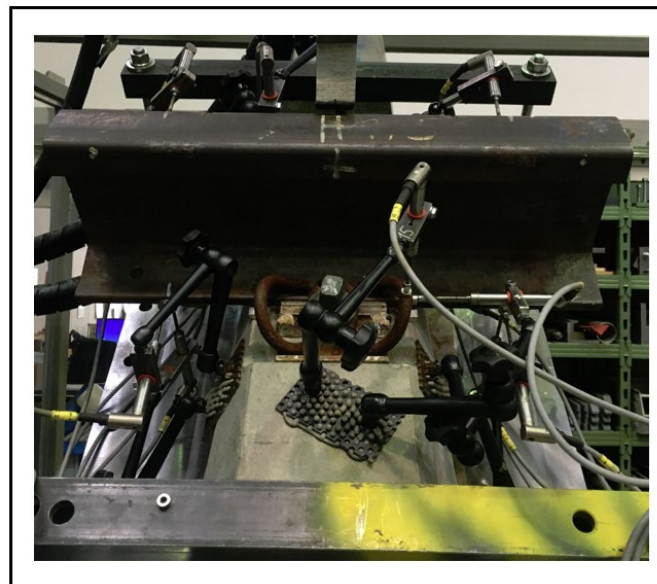

Figure 10: Laboratory test on W 14 rail fastening system using steel angle guide plate and steel rail pad

The transducer sensor installed on the tension clamp parallel to the rail measures the longitudinal displacement of the toes, which is needed to validate the friction value between

the tension clamp toes and the rail foot used in the numerical model. The results of these laboratory tests are provided in the appendix 3.

Determination of the tension clamp lateral and longitudinal resistance of different fastening systems

The tension clamp contributes partly to the lateral rail resistance. In order to understand the effect of the tension clamp in detail, the laboratory tests were carried out. Figure 11 shows the test setup for fastening system Skl 14 as an example.
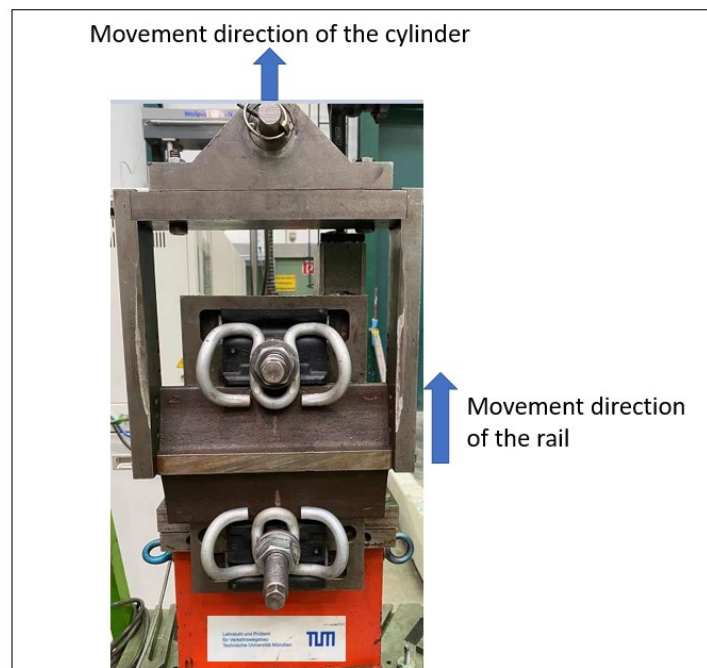

Figure 11: Laboratory test setup for determination of the tension clamp (Skl 14) lateral resistance

In order to obtain a larger free space between the rail foot and the angle guide plate to focus on the resistance behaviour of the tension clamp, beside using the standard angle guide plate (about 0.5 mm gap on each side between rail foot and angle guide plate and about 1 mm gap for both side), the angle guide plates had been milled along the contact area to provide gaps of about 1.5 mm gap on each side between rail foot and angle guide plates. To obtain a stable friction behaviour at the rail foot, a steel plate with lubricant was used to support the rail foot. The rail lateral displacement of the rail and the cylinder force were recorded. The tests were carried out with different types of tension clamps such as Skl 14, Skl 21 and Skl 12. Figure 12 shows the cylinder force vs the rail lateral displacement of Skl 14 as an example. It can be seen that the tension clamp lateral resistance represents a linear behaviour when there is no relative movement between the toes and the rail foot. This linear range can be used for

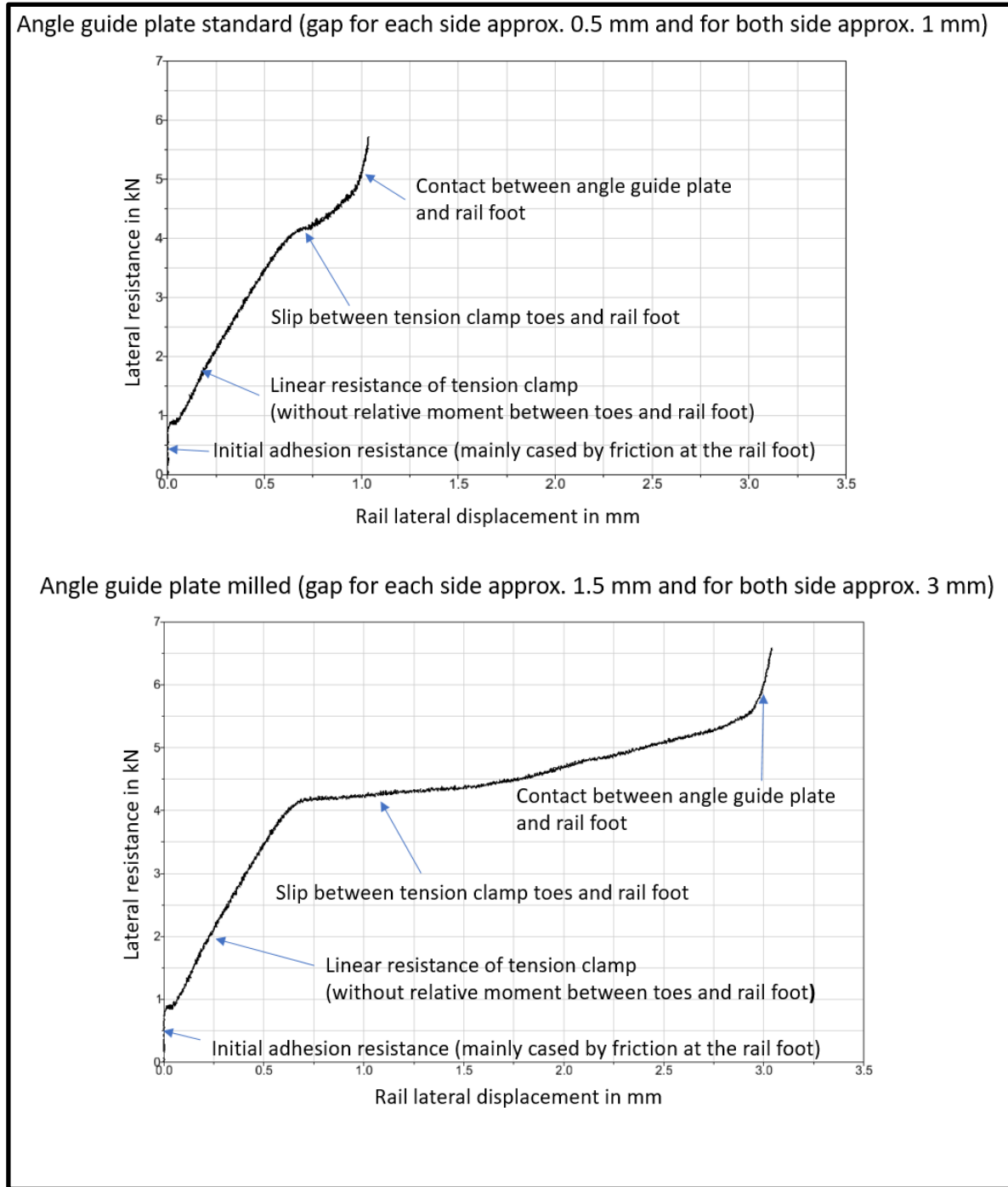determination of the tension clamp lateral spring stiffness to represent the tension clamp resistance property.

Figure 12: Lateral resistance vs rail lateral displacement in a fastening system (Skl 14), angle guide plate standard and milled

To get a better understanding and comparison of the tension clamp resistance behaviour, the tests to determine the longitudinal resistance of the tension clamp were also performed with different tension clamps. Figure 13 shows the laboratory test setup for Skl 14 as an example.
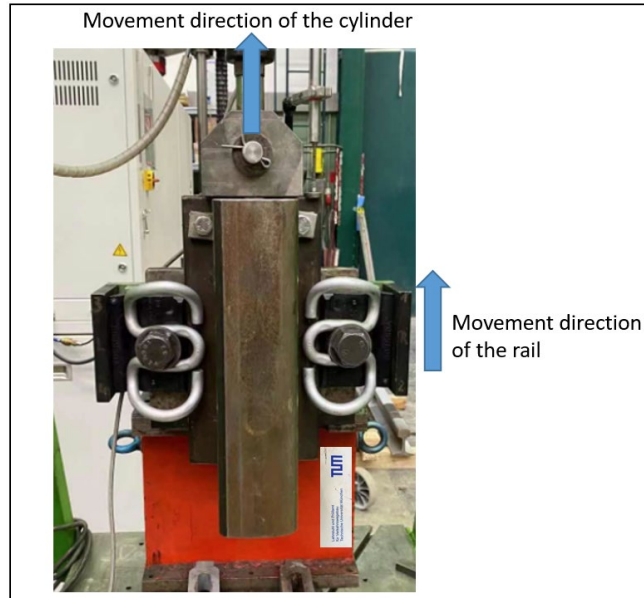
Figure 13: Laboratory test setup for determination of the tension clamp (Skl 14) longitudinal resistance

Figure 14 shows the comparison between the lateral and longitudinal resistance of tension clamp Skl 14 as an example. It can be found that the linear stiffness of the tension clamp in lateral direction is greater than in the longitudinal direction. This can be explained by the geometric situation of the tension clamp in lateral and longitudinal direction.
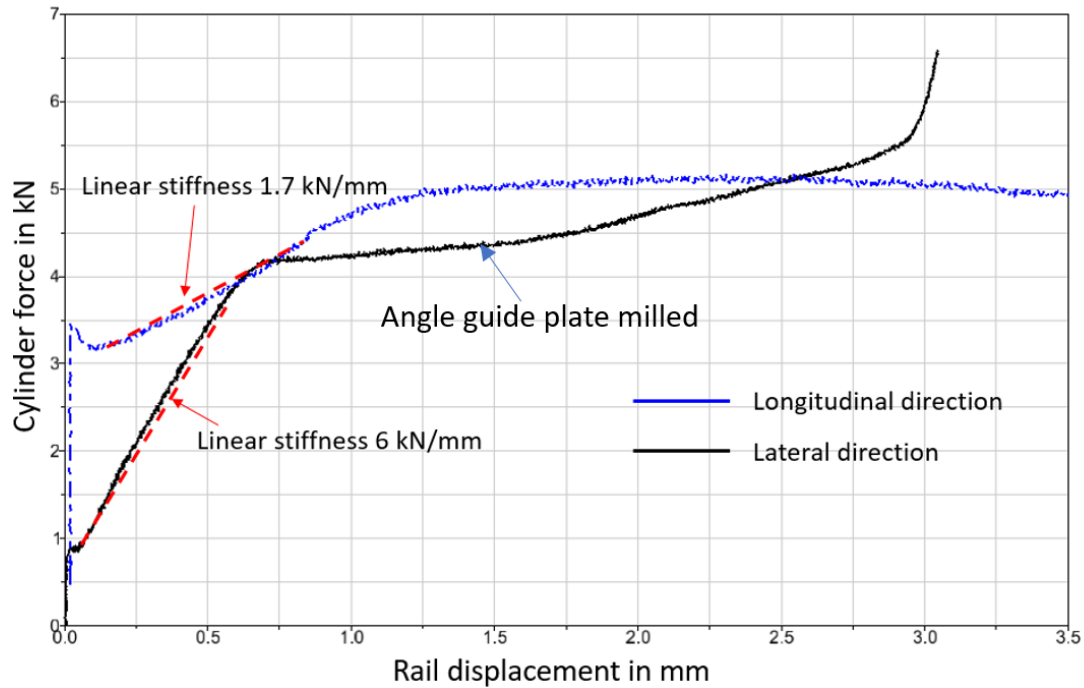
Figure 14: Comparison of the lateral and longitudinal resistance of tension clamps in a fastening system (Skl 14)

Based on the evaluation method described in Figure 14, the evaluation of the measurement results was carried out for different types of tension clamps.

Table 2 summarises the determined mean linear stiffnesses of the different tension clamps in lateral and longitudinal directions.

Table 2: Summary of linear lateral stiffness tension clamp

Tension clamp type	Linear lateral stiffness [kN/mm]	Linear longitudinal stiffness [kN/mm]
Skl 12	5.9	2.3
Skl 14	6.0	1.7
Skl 21	8.1	2.6

The cylinder force vs rail lateral displacement diagrams for tension clamps Skl 12 and Skl 21 are provided in appendices 4 and 5.

Tension clamp properties in vertical direction [12] [36]

In addition to the laboratory test results from this study, the data referenced by [12] [36] are also used as input data for the modelling and calibration of the different tension clamps. The key information of different tension clamp (Skl 28, Skl 14 and Skl 21) is summarized in the following Figure 15. Additional input data referenced by [12] for modelling in this study is described in appendix 6.
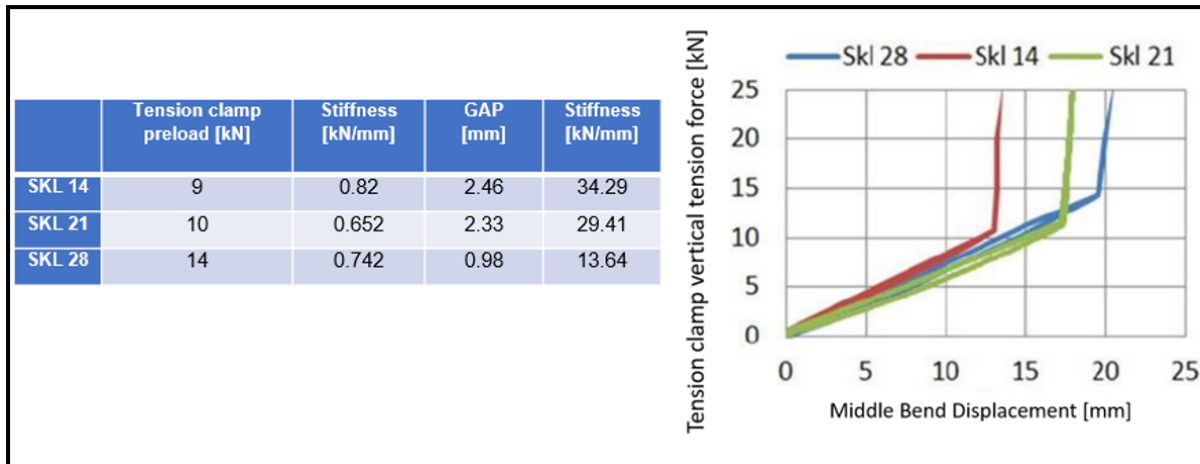
	Tension clamp preload [kN]	Stiffness [kN/mm]	GAP [mm]	Stiffness [kN/mm]
SKL 14	9	0.82	2.46	34.29
SKL 21	10	0.652	2.33	29.41
SKL 28	14	0.742	0.98	13.64

Figure 15: Tension force properties of different tension clamp types [12] [36]

It can be seen that compared to the other tension clamp types Skl 14 and Skl 21, the tension clamp Skl 28 has the maximum tension clamp preload of 14 kN (28 kN for a fastening system), which is realised by the largest middle bend displacement. In practise, the tension clamp Skl 28 is used by ÖBB along the tight curves with radius below 600 m in combination with medium stiff rail pad such as Zw 700 and Zw 900 [10].

4. Field Measurement

4.1 Introduction of the field measurement

The field measurement to validate the track-vehicle dynamic model for this study was performed on 29th October 2020 on the Redl/Zipf-Vöcklamarkt (ÖBB-line Salzburg – Vienna) track section, which is the same track section as described in documentation [12]. Since a large amount of measurements were carried out in [12], the field measurement in this study was performed in selected items aims to support the modelling work.

The measured two sections with the corresponding superstructure components were described in the followings:

Section 1 (km 260,975 to km 261,175): Rail profile 60 E1, W21 (Zw 687a + Skl 21), sleeper type K1 with sleeper pad SLB 3007 G, sleeper spacing a=600 mm and the cant u=160 mm;

Section 2 (km 260,775 to km 260,975): Rail profile 60 E1, W21 (Zw 1000 + Skl 21), sleeper type K1 without sleeper pad, sleeper spacing a=600 mm and the cant u=160 mm.

The overview of the installed measurement sensors and their positions is depicted in Figure 16.
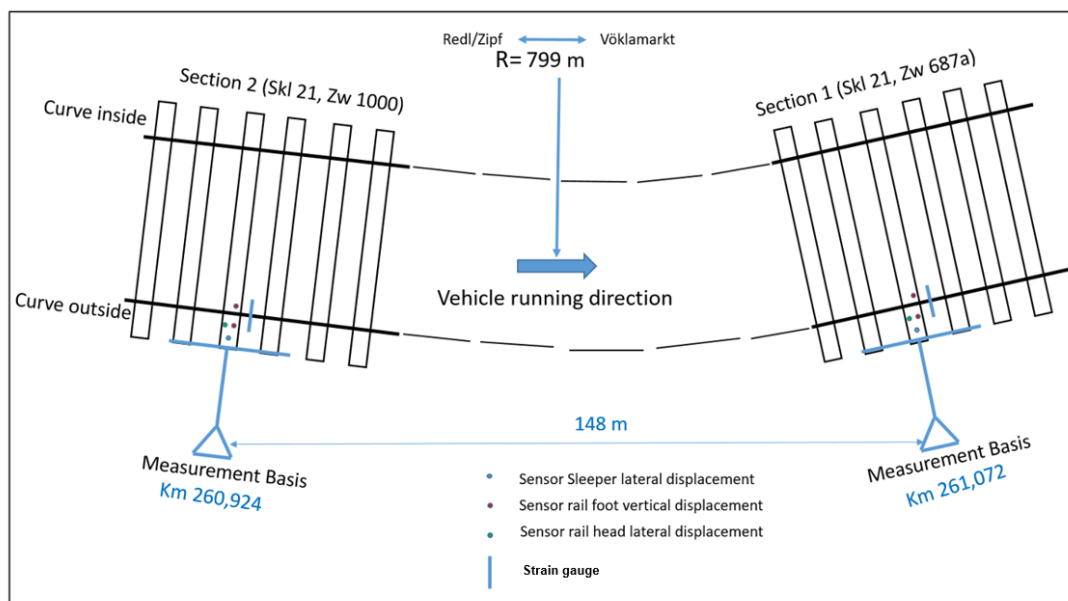
Figure 16: Overview of the installed measurement sensors and their positions

Figure 17 illustrates the field measurement devices of the field measurement.

Figure 17: Illustration of the measurement devices of the field measurement

Two sections had been equipped with sensors to determine the sleeper absolute lateral displacements using rigid reference bases installed outside the track. The sensors to determine the relative rail lateral, vertical and rotational movements were installed between rail and sleeper. The curve radius of the measured section is 799m along the track from Redl/Zipf to Vöcklamarkt. The distance between the two measurement bases installed on the two sections is 148 m.

4.2 Analysis and evaluation of the field measurement

The information of the track cant and track gauge along the measurement section had been received from ÖBB as listed in Table 3.

Table 3: Track information from ÖBB

Position	Cant actual unloaded [mm]	Cant Actual loaded [mm]	Cant Target [mm]	Gauge actual unloaded [mm]	Gauge actual loaded [mm]	Gauge target [mm]
Km 260,920	157	157.9	160	1444	1444	1437
Km 260,925	156	156.9	160	1444	1444	1437
Km 260,930	157	157.0	160	1444	1445	1437
Km 261,070	158	158.4	160	1443	1443	1437
Km 261,075	158	158.8	160	1442	1442	1437
Km 261,080	157	157.9	160	1443	1443	1437

The measured track data of two train passages with locomotive type 1116 by ÖBB Railjet were selected to carry out the evaluation and to verify the simulation results for the track scenario described in section 7.2.

According to the formula $U=11.8*V^2/R-U_f$ [45], where U=160 mm (cant), V=120 km/h (vehicle speed) and R=799 m (radius), the cant deficit U_f is given by $U_f = U-11.8*V^2/R \approx 53$ mm.

The measured vehicle speeds during the passage of the measurement section were 119 km/h and 121 km/h (average 120 km/h).

Figure 18 shows an example of the curve outside rail head lateral displacement during the selected time domain of the locomotive passage in two different fastening systems. One can conclude that the curve outside rail head displacements of both fastening systems are towards to the track outside. The dynamic peak value of the rail head lateral displacement under leading wheelset curve outside is close to 1 mm (low pass filter 100 Hz) at the soft rail fastening system (Skl 21+ Zw 1000) and about 0.7mm at the stiff rail fastening system (Skl 21 + Zw 687a).
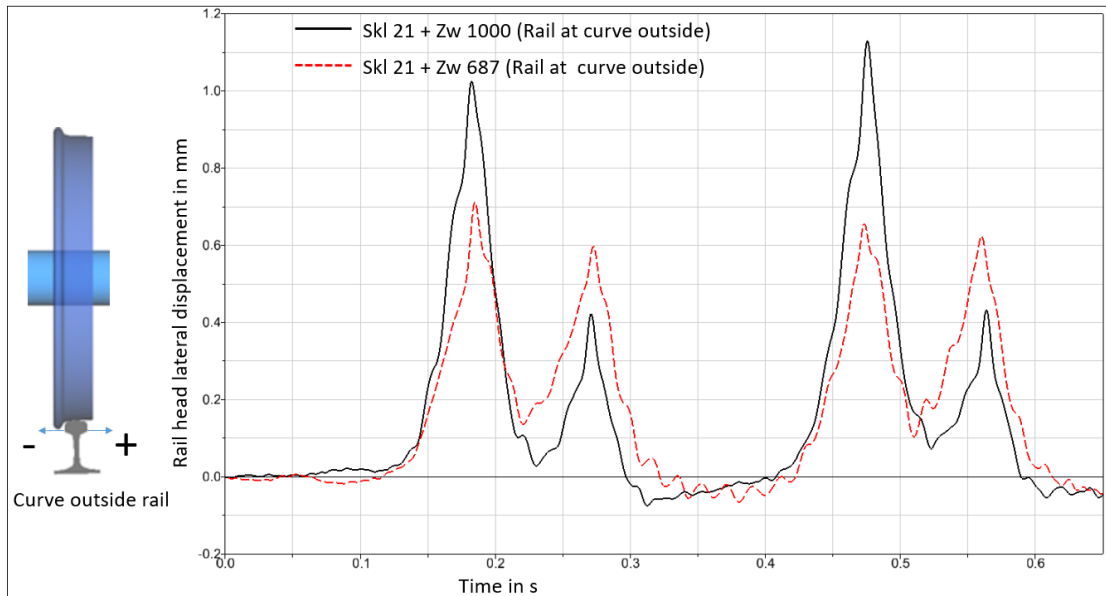
Figure 18: Measured rail head lateral displacement (outside rail) vs. sleeper surface

Figure 19 shows the measured sleeper lateral displacements in different measurement sections with and without sleeper pad. The average dynamic peak under leading wheelset is about 0.2 mm in direction curve outside for both systems, with and without under-sleeper pad (USP), but the lateral displacement of sleeper with sleeper pad is more uniform. Since no significant maximal sleeper lateral displacement was observed in this field measurement section, the difference with and without under-sleeper pad (USP) was neglected in the numerical calculation described in section 7.2.
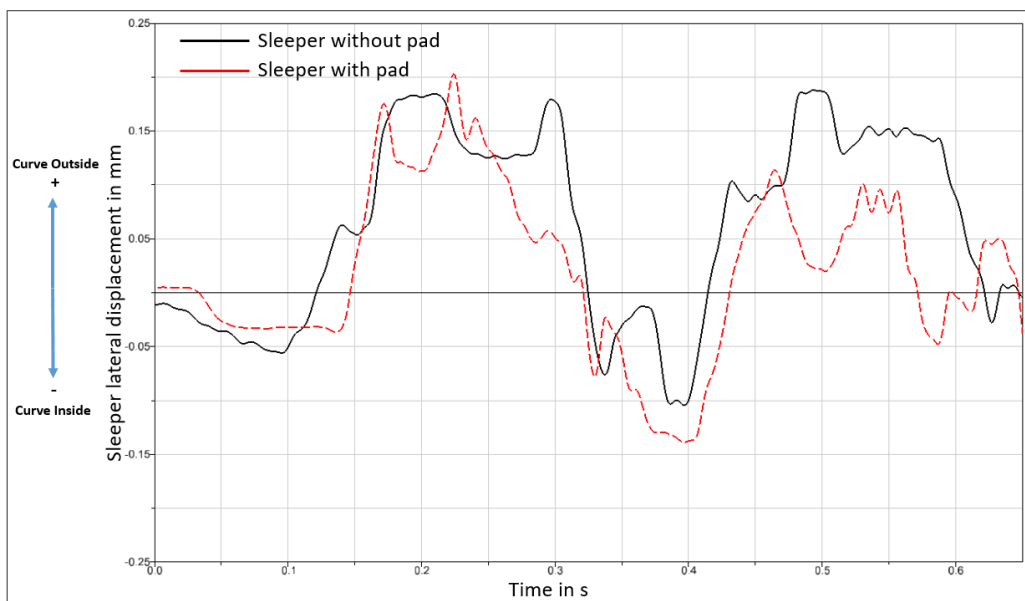
Figure 19: Measured sleeper lateral displacement

Figure 20 illustrates the compared results (low pass filter 100 Hz) measured from the strain gauges at the bottom of the rail foot installed on the section of tension clamp Skl 21 + rail pad Zw 687 as an example.
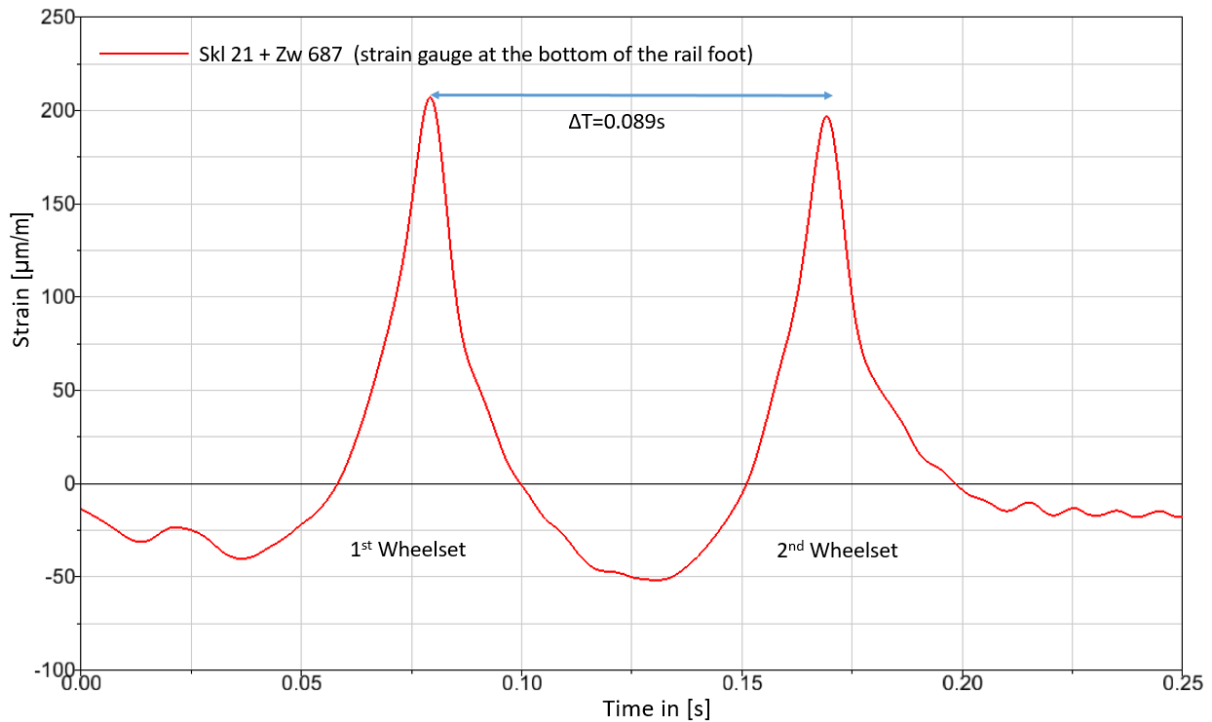
Figure 20: Comparison of the strain values of the different track sections

The focus is on the strain values at the rail foot bottom under the 1st and 2nd wheelset passage of the 1st bogie of the locomotive type 1116. The wheelbase of the bogie is 3 m and the time interval between the two peaks is 0.089 s. Thus, the pass-by speed of the vehicle in this example can be calculated to be about 121 km/h. The other measurement results are provided in appendix 7.

5. Numerical superstructure model and its validation

The numerical tool consists of different models to perform the analysis for different objectives. It can perform the analysis on two main layers of the rail track superstructure, namely the layer of fastening system and the layer of sleeper and its support, considering the whole track.

The fastening system can be either a simplified model that is integrated in the vehicle-track dynamic system model as a sub-model or it can be used as an independent engineering tool by using a full 3D tension clamp to study:

- Tension clamp assembly preload and stiffness under consideration of the geometry,

- Fatigue (stress, strain) analysis of the tension clamp considering the 3-dimensional rail movement under actual wheel/rail contact force.

- Natural frequency analysis of the tension clamp and frequency interference effect with the other connected elements like the rail and the rail support condition.

Figure 21, which was taken partly from Figure 1, clearly illustrates the relationship between the previous chapter 3 and the following sections (chapter 5.1, 5.2, and 5.3).
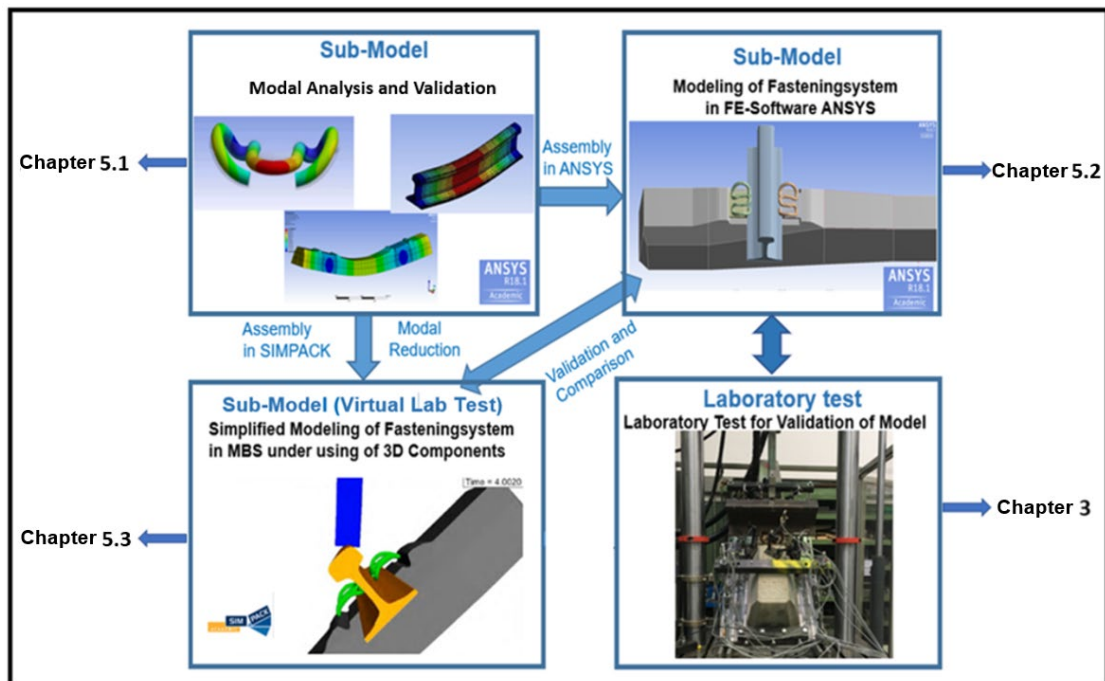
Figure 21: Validation chain of FEM, MBS and laboratory test

The FEM-model can better reproduce the boundary conditions in comparison to the MBS-model. However, the disadvantage of the FEM-model is the unacceptable long calculation time, especially with dynamic loads. To integrate the fastening sub-model into the overall vehicle/dynamic system, it is necessary to use the MBS model in SIMPACK environment. But the possibilities to define the contact conditions according to the real situation in the MBS environment are limited. Therefore, it needs a validated FEM-model to perform varied scenarios to adjust the equivalent contact conditions in MBS-environment. The MBS environment model is using a CAD-FEM-MBS chain, which is developed as an engineering tool to achieve the target aimed in this study.

Some of the selected designs and configurations of rail fastening components are motivated by the required parameter variation for the model validation work (chapter 5.5) and the intended sensitivity analysis (chapters 5.6 and 5.7), but not with regard to the application in specific track sections.

5.1 Modelling of the components

Modelling of the rail

The rail model is designed according to the method described in [15] [16]. The 3D rail model in IGES file format is created using CAD software SolidWorks according to the technical drawing of rail type 60 E2 (Figure 22). Table 4 summarises the values of mass and geometry parameters provided by the manufacturer and of the 3D model. It can be seen that the created 3D rail model has the same properties as the real product. The rail model was imported to FE (finite element) software ANSYS Workbench in STEP file format to perform meshing and modal analysis.
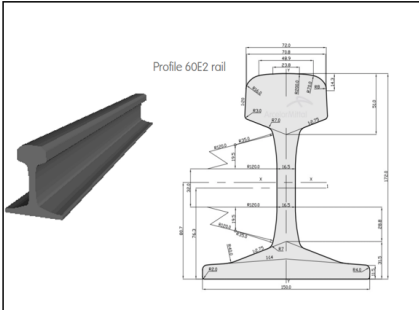
Figure 22: Illustration of 3D rail model and the corresponding 2D drawing for rail 60 E2 [37]

Table 4: Comparison of material and geometry properties of 3D model and manufacturer's specification

	Area (cm^2)	Mass (kg/m)	Moment of Inertia Ixx (cm^4)	Moment of Inertia Iyy (cm^4)
3D Model	76.5	60.06	3023.22	511.30
Manufacturer's specification	76.5	60.05	3023.22	511.30

To validate the modelling for further processing, hammer impact tests were carried out in the laboratory on the rail section 60 E2 with a length of 1.5 meters. Figure 23 shows an example of the sensor response from the hammer impact test at the end of the rail section performed in vertical direction. It can be used to calibrate the numerical model for the natural frequencies and mode shapes. Since the natural frequencies and mode shapes depend closely on the material and geometrical properties such as the elastic modulus E and the area moment of inertia I, the impulse test is an essential and effective method for validating the numerical model.
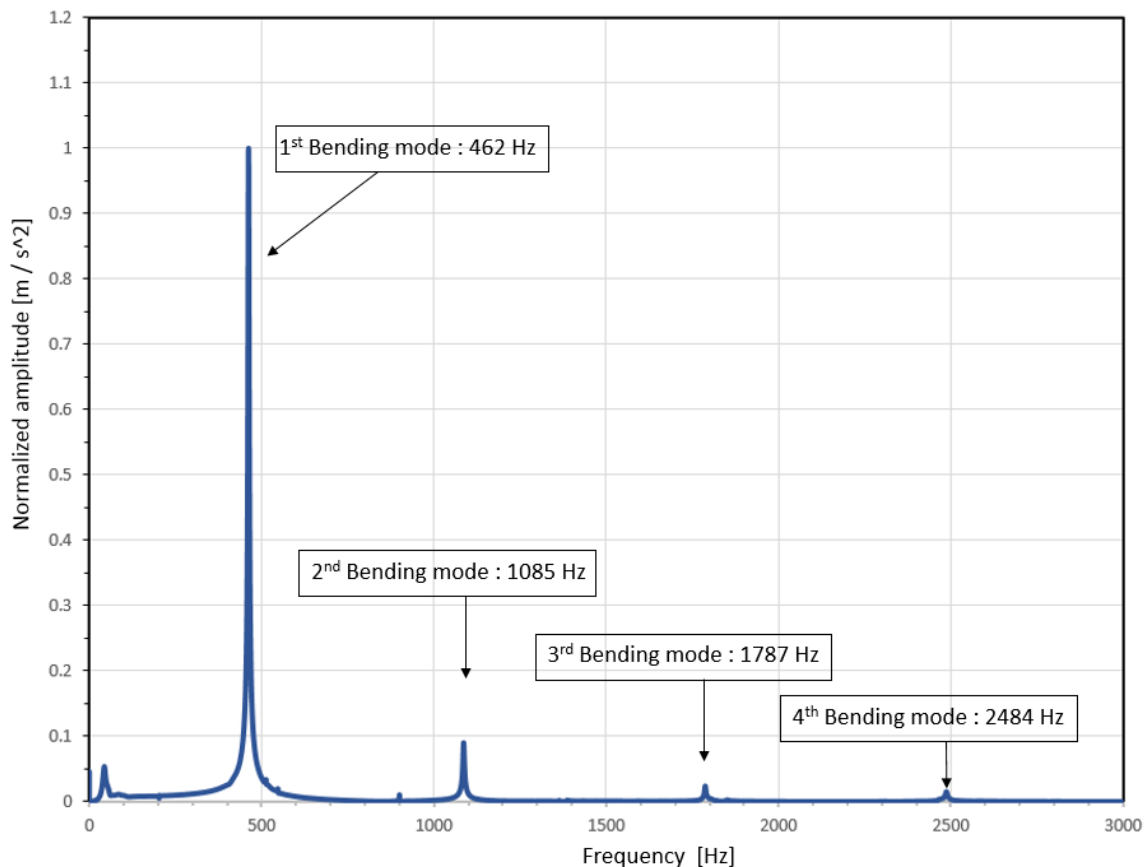
Figure 23: Vertical sensor response of hammer impulse test on the end of the rail section

Table 5 shows the natural frequencies determined by the FE modal analysis for comparison with the measurement. The modal analysis provides the most important dynamic properties. Therefore, it proves that the created 3D model has a good quality.

Table 5: Natural frequencies of FE-Model (ANSYS) and measurement

Mode	Natural frequencies (Hz) rail 60 E2 1.5 m			
	Vertical (ANSYS)	**Vertical Measurement**	**Lateral (ANSYS)**	**Lateral Measurement**
1	455	462	199	202
2	1065	1085	506	511
3	1756	1787	893	894
4	2441	2484	1343	1367

Modelling of sleeper model

The modelling workflow of a sleeper follows the rail modelling procedure.

Figure 24 shows the 3D model of the sleeper.
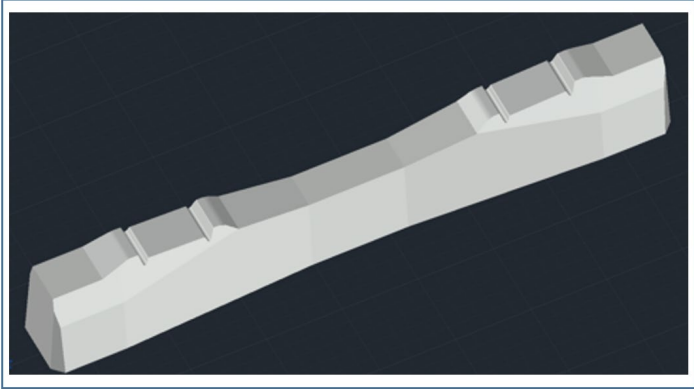
Figure 24: 3D sleeper model (B 70)

The pre-stressing rebars and the interface conditions between the rebars and the sleeper concrete were defined in ANSYS Workbench. The model with pre-stressing rebar bodies shows an increase of about 10 Hz of the sleeper 1st bending frequency compared to the model without rebar bodies [15]. The pre-stressing force effect was handled indirectly by increasing the elastic modulus of the sleeper material properties in the model. Since the geometry of the sleeper is relatively complex, a high meshing quality with ICEM was required with respect to calculation time and accuracy. Figure 25 shows the definition of rebar bodies and the meshing

quality by using the ICEM method. In the end, the model in ANSYS environment was saved as.fbi file and was imported in SIMPACK.
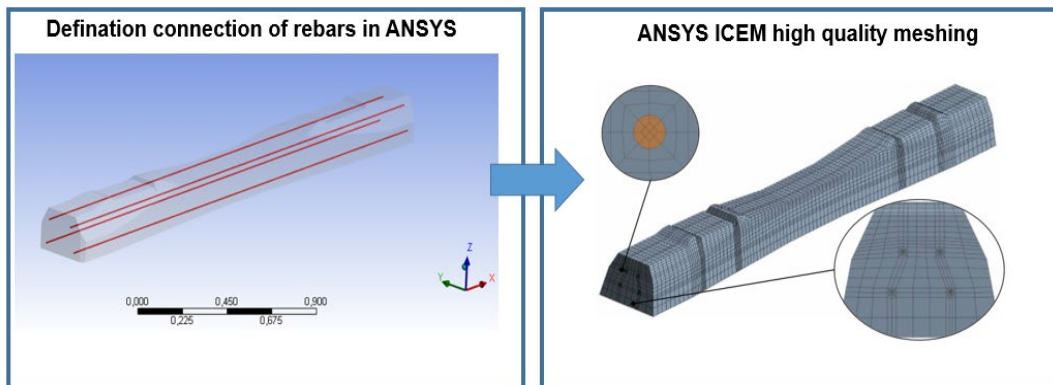
Figure 25: Integration of reinforcement bars and ANSYS ICEM high-quality meshing

The model checking for mass and geometry properties was performed in the MBS software SIMPACK environment (Figure 26).

	Volume [dm^3]	Weight [kg]
Manufacturer's specification (Moll-Betonwerke AG)	approx. 114	280 - 303.5
3D Model in SIMPACK	114.76	296.14
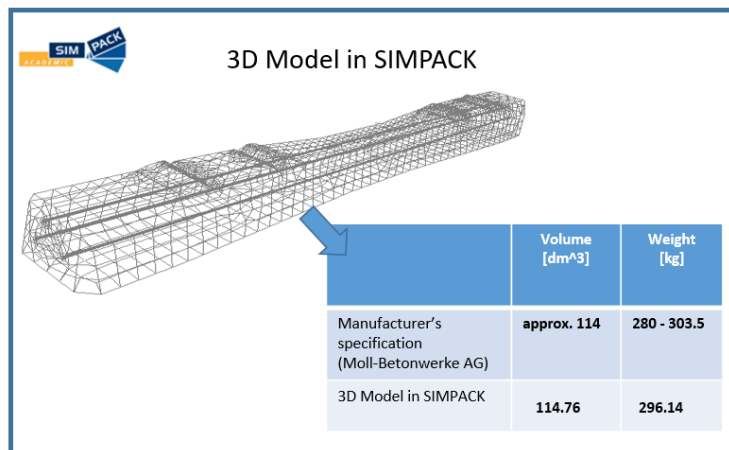
Figure 26: Model information in comparison with manufacturer's specification

The weights of three B 70 sleepers were examined (Figure 27) and the hammer impact test was carried out (Figure 28) to validate the model. The support conditions have an influence on the response of the sleeper with respect to the vertical 1st bending natural frequency in comparison with the rail test sample, since the natural frequency of the sleeper is much lower than the 1st bending natural frequency of the rail sample. Therefore, several support conditions were tested.

Figure 27: Weighing of sleepers
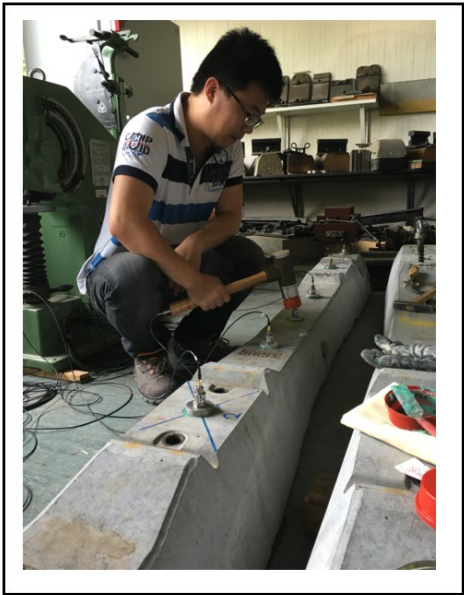
Figure 28: Experimental device and the test process of hammer impact test

Figure 29 shows the support conditions and the positions of the seven acceleration sensors on the sleeper.
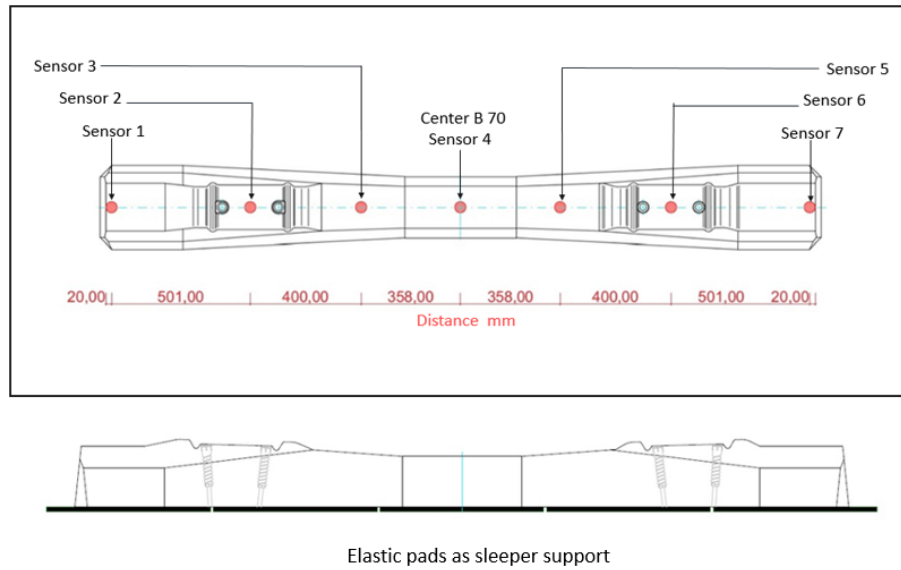
Figure 29: Support conditions and positions of acceleration sensors

One result as an example of sensor 1 can be seen in Figure 30.
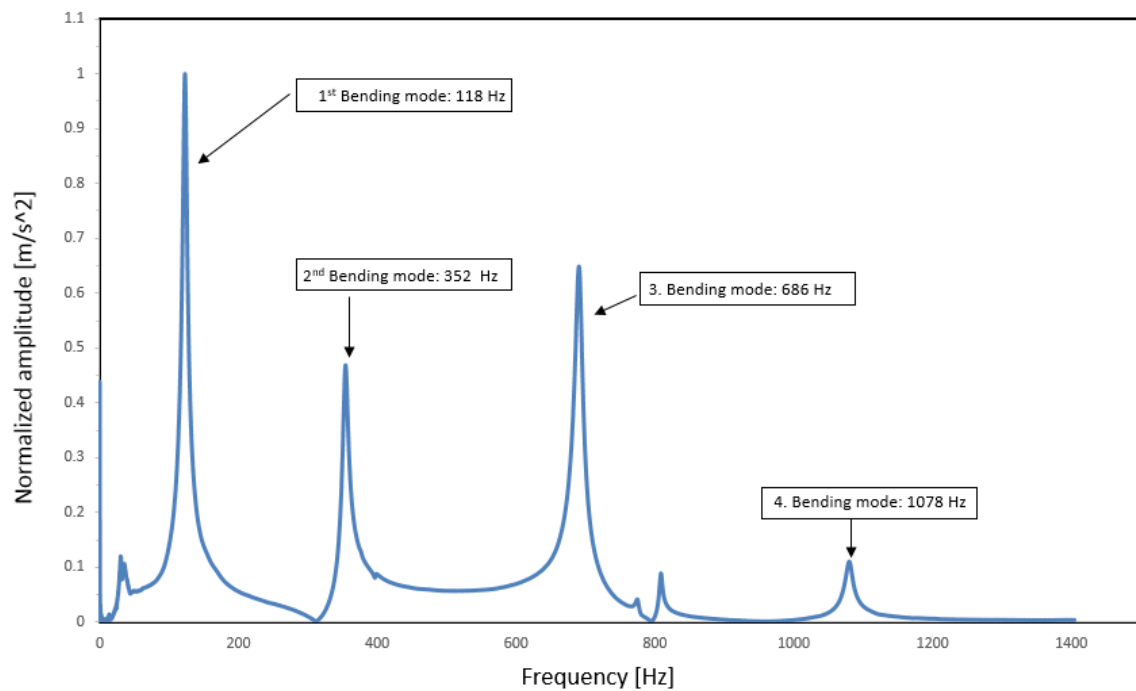
Figure 30: Vertical sensor response of hammer impulse test on sleeper supported on elastic pads

Table 6 collects the natural frequencies from simulation and measurement under different contact conditions.

It can be seen, the values calculated from 3D sleeper model is consistent with the measured data with elastic pad support.

Table 6: Sleeper natural frequencies of FE analysis and measurement

Mode	Vertical natural frequencies (Hz) B 70 sleeper			
	FE (ANSYS)	Experimental support: elastic pads	Experimental support: wood block	Experimental support: hanging
1	118	118	136	115
2	352	352	360	352
3	673	686	688	685
4	1057	1078	1084	1078

Modelling of tension clamp

Figure 31 shows a full 3D tension clamp Skl 14 as an example from the created model database.
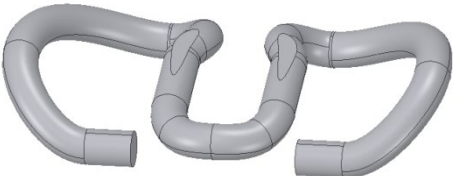
Figure 31: 3D Model of tension clamp Skl 14

The general validation of the tension clamp Skl 14 regarding the natural frequencies and the toe action forces on the rail foot was investigated in [22]. According to the validation experience in this work, the clamp defined as full steel material body will be correct, if the mass and geometry properties are correctly defined, and the meshing is created with good quality. Then the modal analysis by body free motion can be correctly carried out by ANSYS.

The additional challenge of this research is to realize the tension clamp resistance against rail movement under lateral static and dynamic loads. Large deformations cause problems in numeric simulation calculations, which require a higher modelling quality.

A newly developed workflow for modelling tension clamps using FEM – MBS co-simulation is used to calculate the tension force even under large deformation (Figure 32). The approach

can be used to predict the dynamic effect on tension clamp preload caused by railhead lateral displacements.

High-quality meshing is needed. Therefore, hexahedral elements had been used. The ICEM CFD tool or hyper mesh tool guarantees the correctness for further usage of the modal information in the MBS environment.
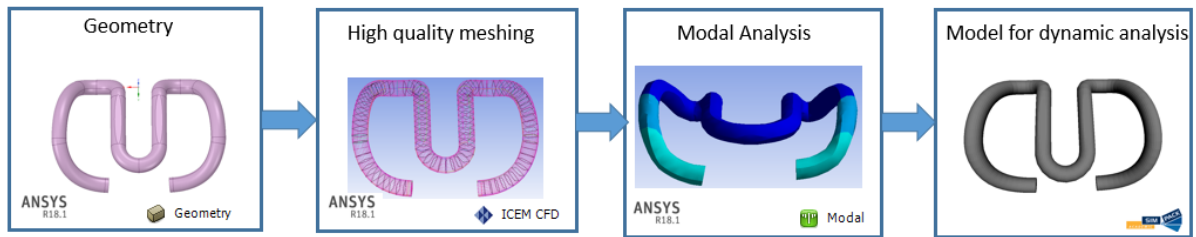
Figure 32: Modelling workflow of tension clamp for dynamic analysis

The details of the definition of the contact conditions and validation processes within the fastening system were explained in section 5.2.

Modelling of angle guide plate

The angle guide plate serves the rail tension clamp as constraint, leads the lateral wheel/rail contact forces into the sleeper. The 3D models of the angle guide plate were created, see Figure 33 as an example in the created database. The material properties which are summarized in [38] for investigation of this topic, see chapter 5.2. Since the angle guide plate plays an essential role in the fastening lateral stiffness, the detailed investigation on the angle guide plate is described in chapter 5.4.3.
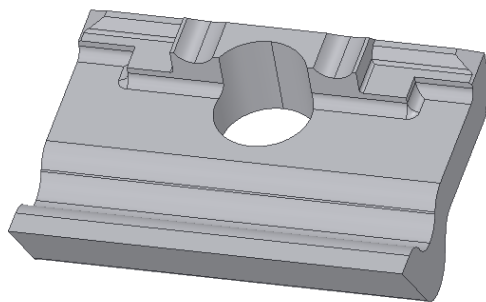
Figure 33: 3D Model of angle guide plate

Modelling of and rail pad

The 3D models of rail pad, see Figure 34 as examples in the created database. The material properties which are summarized in [39] for investigation of this topic, see chapter 5.2.
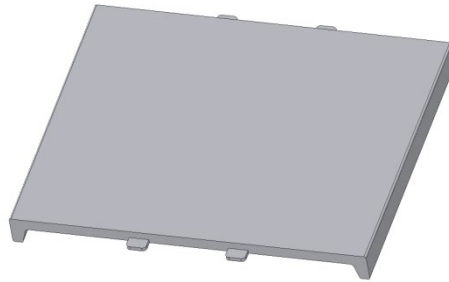
Figure 34: 3D Model of rail pad

It should be noted here that in this study, for modelling purposes, the rail pad is treated as a non-linear spring affecting the vertical and rotational moment of the rail and the input data is validated by laboratory tests. The complete 3D model shown above is used as a reserve in the database for further applications.

Review of the meshing quality

Most of the effort on the modelling work in FEM environment is mashing. In this study, all meshing elements in the models are created manually with hexahedral meshing elements in a high quality level through ICEM CFD tool in ANSYS. The automatic meshing for complex geometry can be done by using tetrahedral meshing elements. For a further research and to carry out a FEM-MBS Co-simulation, a high quality meshing with hexahedral meshing elements is required.

Figure 35 shows an illustrated overview of the meshing quality of the corresponding fastening components from CAD 3D environment into the FEM environment for preparing of the meshes.
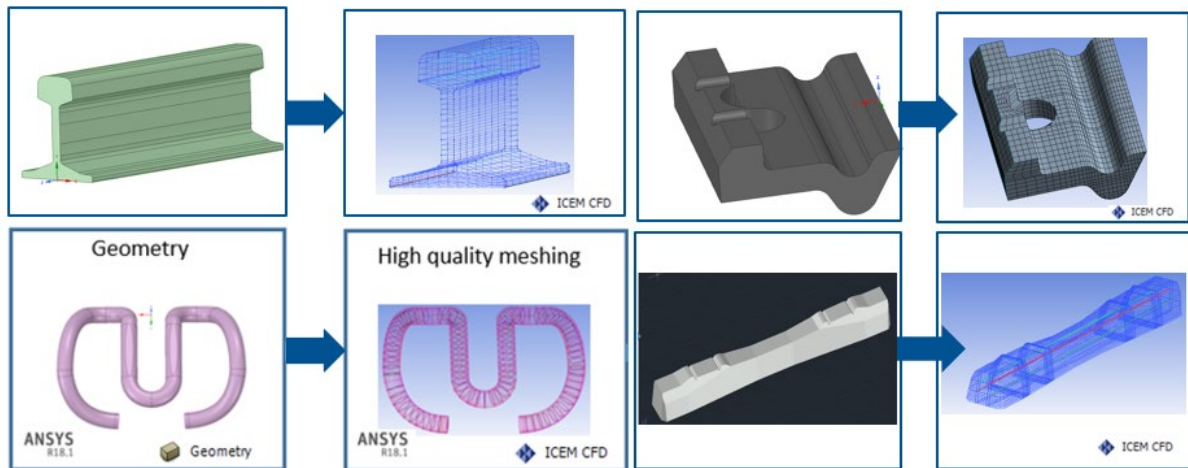
Figure 35: Overview of the meshing of the components

5.2 Model in FEM for validation of the contact condition in MBS

A typical assembly of the fastening system W14 includes tension clamp Skl14, angle guide plate, and rail pad Zw 700.

The modelling of the fastening system is performed in two different software environments, one model is created in FE software ANSYS for static analysis and the other one is based on the ANSYS-model but modified in MBS software SIMPACK for performing the dynamic analysis. The focus of the modelling work is on the lateral railhead displacement to investigate the influence on the wheel-rail contact conditions. The mechanism of rail lateral motion, rail vertical motion, and rail rotation are built in this model (see Figure 36).
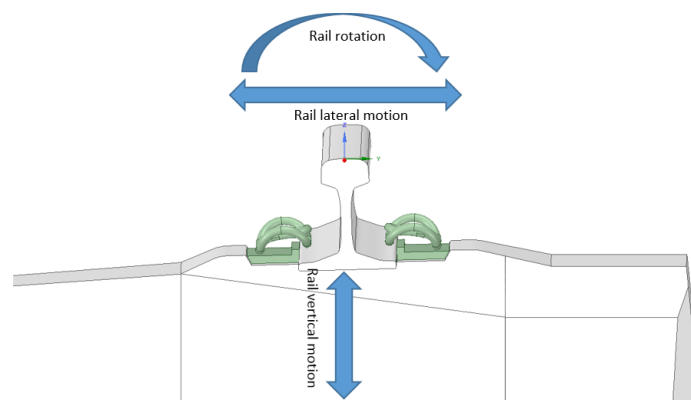
Figure 36: Rail motion in vertical, lateral, rotational direction

The main parameter of the material properties for modelling are listed in Table 7

Table 7: Material properties of components

Component	Young's Modulus E (MPa)	Poisson's ratio	Density (kg/m³)
Tension clamp (SKL14)	210000	0.3	7850
Angled guide plate	12000	0.4	1150
Rail pad (ZW700)	8.92	0.45	1050
Rail	210000	0.3	7850
Concrete sleeper	50000	0.2	2600

Definition of contact and constraint conditions

First, the FE models of the fastening system W14, sleeper, and rail were compiled to one model. The contact and constraint conditions are defined in the assembled model.

The contact type definition for the tension clamp and the rail is "No Separation", which does not allow separation between surfaces, but sliding can occur along with the contacting faces. To simulate the tightening of the tension clamp and the preload on the spring arms activated by the screw, a displacement is applied to the middle bend of the tension clamp instead of using a predefined load acting on the middle bend of the tension clamp.

Based on the manufacturer specification [39] for Skl 14, there should be a deflection of about 12 mm on the tension clamp to activate a toe load of about 9 kN, which is also calculated by the ANSYS model. The description of the definition for contact and constraint conditions between the components can be found in documentation [38]. Figure 37 shows one of the examples to define the contact and constraint conditions between tension clamp arms and rail foot.
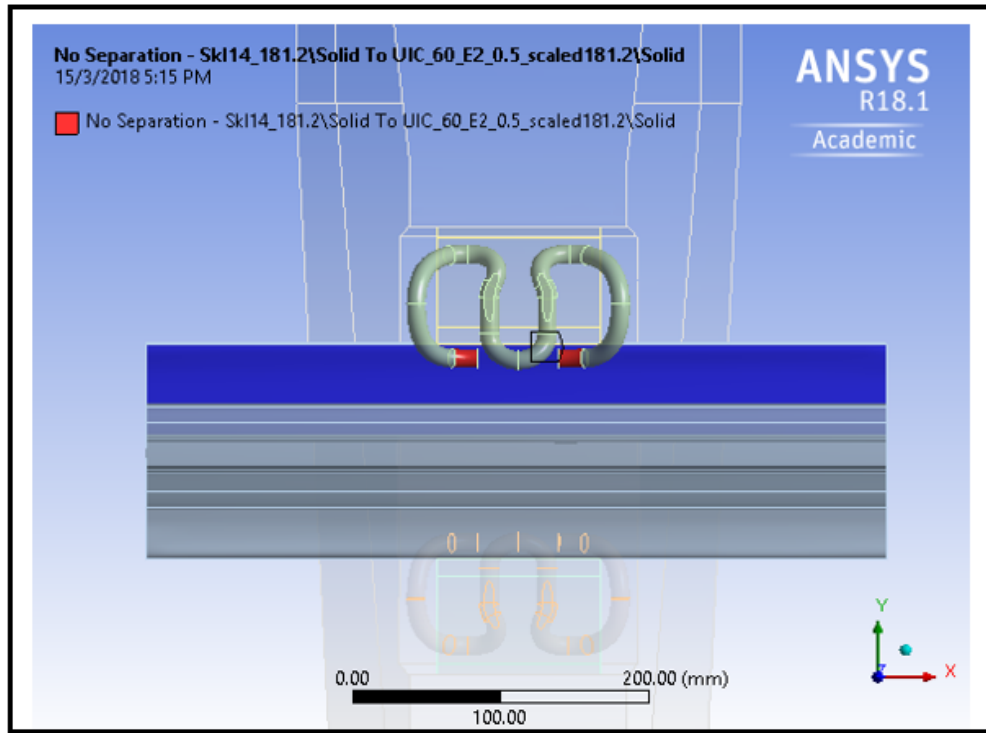
Figure 37: Definition of the contact and constraint conditions between tension clamp spring arms and rail foot

All contact and constraint conditions between the components are listed in Table 8

Table 8: Definition of the contact and constraint conditions between the components

Contact Bodies	Target Bodies	Type
Tension clamp	Rail	Frictional, Coefficient = 0.1
Tension clamp	Angled guide plate	Bonded Penetration Tolerance = 0.1mm
Rail	Angled guide plate	Frictional, Coefficient = 0.2
Rail	Rail pad	Frictional, Coefficient = 0.3
Rail Pad	Angle guide plate	Frictional, Coefficient = 0.3

5.3 Workflow of the numerical tool for a virtual lab test of the fastening system

This section presents the modelling chain of the final numerical tool for designing of the fastening system, which works in the MBS Environment. The modelling process from preparing of the 3D modelling to the MBS environment is depicted in the following logic chart again.
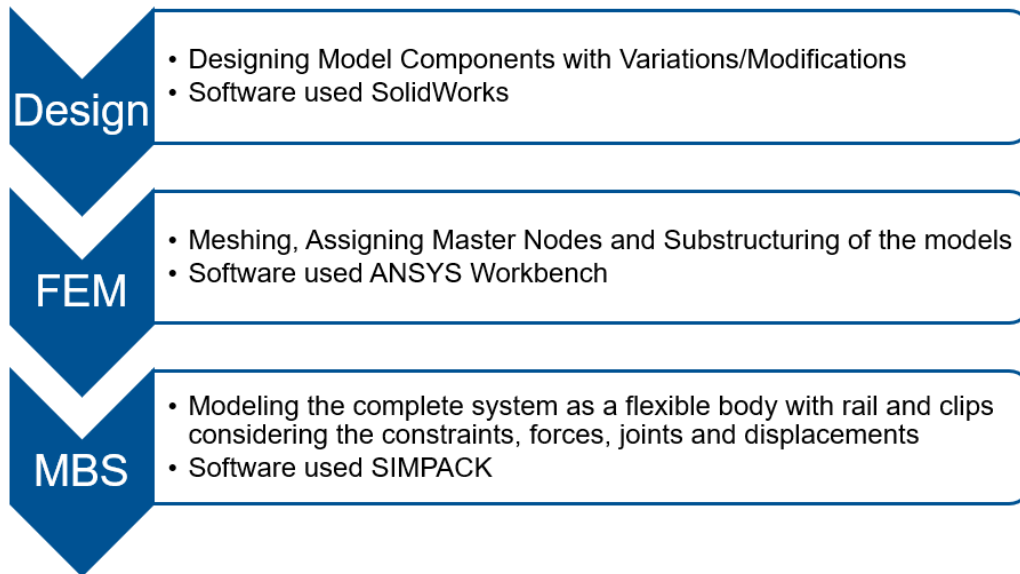
Figure 38: Logic chart of the modelling process

For a clear explanation of the used commercial software to achieve the whole process and the functionalities, Figure 39 illustrates the workflow. The validation of the created model with the laboratory tests and the development of the interface between different software environment aims to solve the particular engineering problem belongs to the key points of this work. One of the essential functions of the tension clamp is to supply the tension force, which consists of the preload and the resistance force through the clamp stiffness to ensure the rail holding the position during the train passing. One can use this numerical tool to calculate the different tension force caused by the middle bend displacement and geometry properties from different tension clamp design. Just as it was mentioned in chapter 1.3, normally the tension force will be modelled for force or spring elements for the whole track/vehicle dynamic model but for the precisely analysis of the load distribution and fatigue on the tension clamp, it is necessary to create a full 3D model as described in the numerical tool.
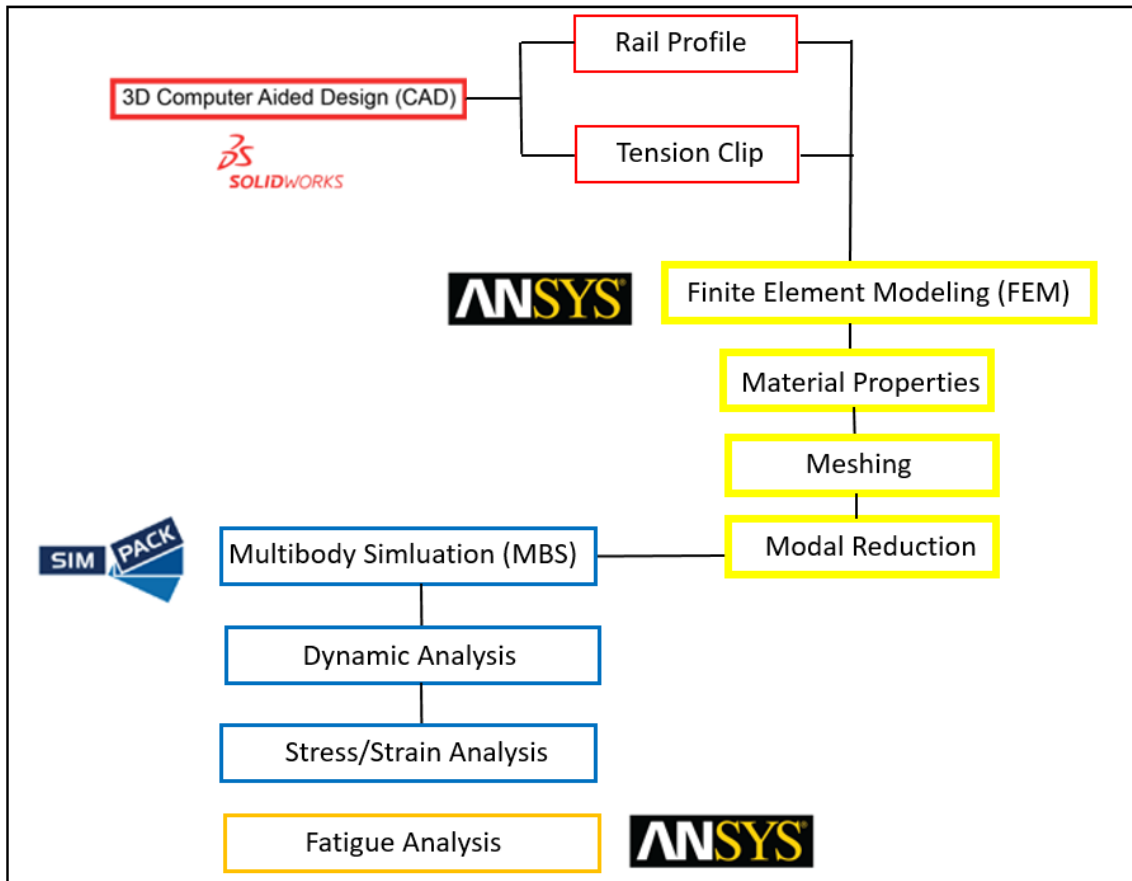
Figure 39: Overview of the software environments for the co-simulation workflow

Overview of the prepared models with different tension clamps as an example in the database

Based on the previously described modelling method, fastening systems with different tension clamps were created in the MBS environment of software SIMPACK as a database for dynamic analysis. Figure 40 shows an overview of the model database as an example.

Figure 40: Overview of model database with different tension clamps in MBS environment of Software SIMPACK

5.4 Modelling of the fastening components working in lateral direction

5.4.1 Definition of the lateral stiffness of the fastening system

The lateral stiffness of the fastening system depends in reality on many factors, such as the stiffness of the angle guide plate, the gap between the angle guide plate and the rail foot, the friction between the angle guide plate and the sleeper, the tension clamp stiffness in lateral direction, the friction between the rail pad and the rail foot. They vary greatly due to installation conditions, different product types and material surface properties. Therefore, each measurement to verify the model represents an individual case. For the vehicle/track dynamic model in this research, a linear stiffness is used instead of a complex non-linear behavior to simulate the lateral fastening stiffness. To perform the sensitivity analysis, a parameter variation in a range from 20 kN/mm to 80 kN/mm was used according to the documentation [9] [12] [19] [44] [46]. However, for the rail fastening model, the 3D numerical modelling method used in this study offers the possibility to perform a detailed analysis in specific areas for specific cases. It helps in optimizing the component design. In the following chapters, the 3D modelling method for lateral components (tension clamp and angle guide plate) in a fastening system is explained.

43

5.4.2 Modelling of the lateral movement behavior of the tension clamp

The tension clamp does not only provide the rail preload and the rail resistance in vertical direction, but also in the lateral and longitudinal direction. In the following study, the working principle is modelled for the lateral direction.

According to the laboratory tests described in chapter 3.2, the functionality of the tension clamp Skl 14 lateral resistance effect is verified and shown in Table 9.

Table 9: Calculated tension clamp (Skl 14) lateral resistance

Tension clamp Skl 14	Lateral displacement of toe in mm	Lateral resistance force of one tension clamp in kN
	0.1	0.32
	0.5	1.6
	1	3.2

Figure 41 shows the functionality of the model in the assembled state. During preload application (picture left), the tension clamp toes move slightly towards the outside on both sides of the rail. Because of rail movement in the lateral direction (picture right), the toes on the side of the rail movement direction move towards inside and the opposing toes move towards outside in the longitudinal direction of the rail section.
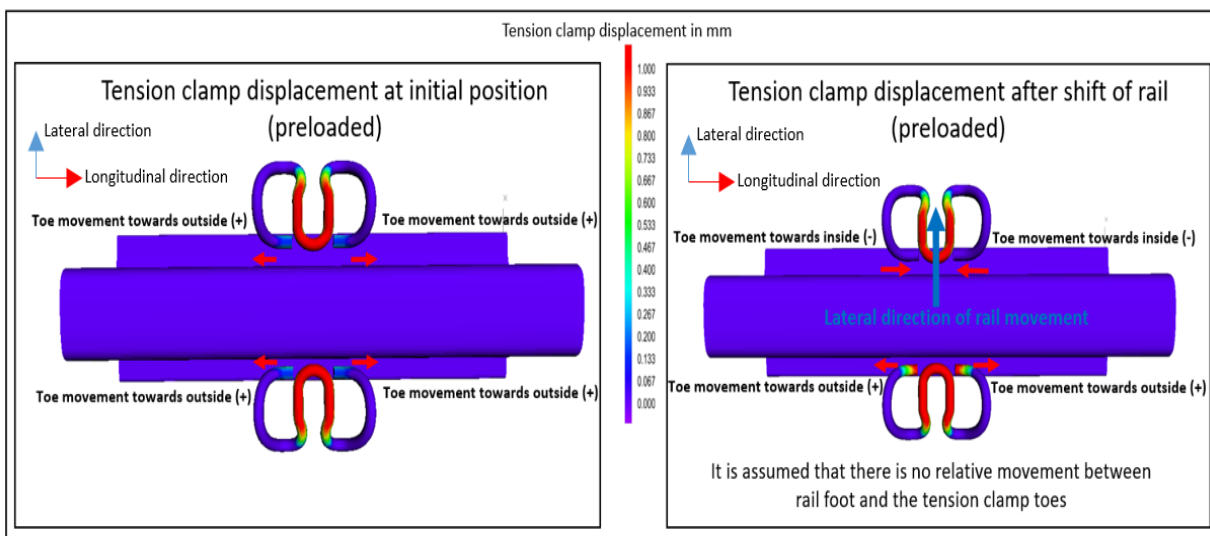
Figure 41: Illustration of tension clamp movement under rail lateral displacement

5.4.3 Modelling of angle guide plate

The modular modelling chain developed in this study has the possibility to assemble the 3D components into a model that meets the different tasks and requirements. An example as shown in Figure 42, in the left picture, the angle guide plates have been modelled as a spring (force element) instead of 3D model compared to the picture right.

If one performs the analysis on the entire fastening system and focuses on the rail displacement under load conditions, a large calculation time can be saved with the modelling method shown in the left picture. If the analysis is focused on the angle guide plate itself, the method of right picture is used.
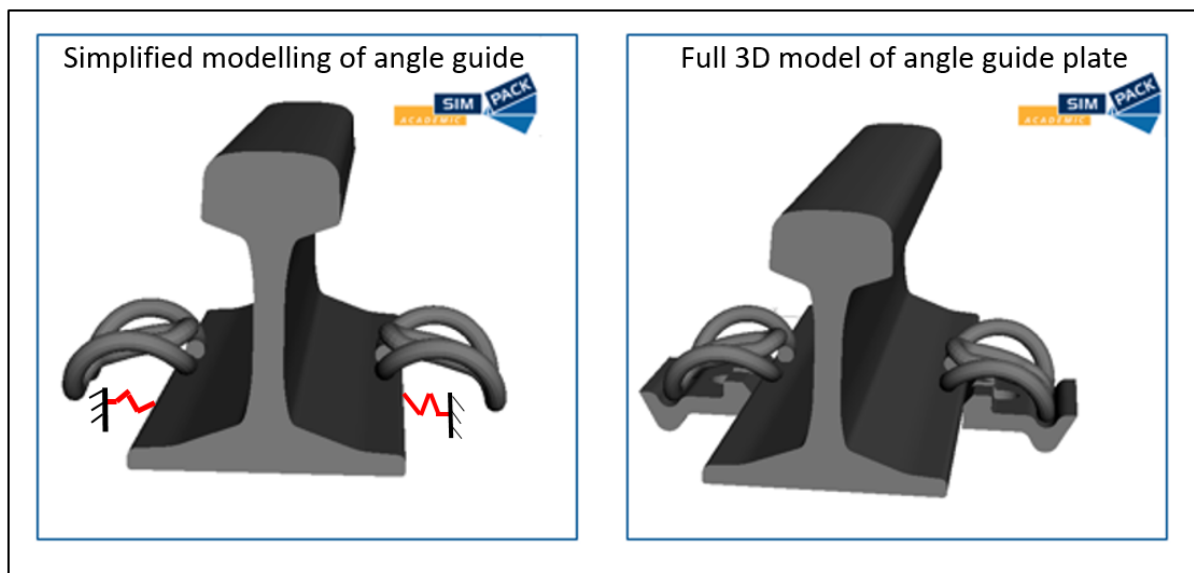
Figure 42: Simplified and 3D modelling of angle guide plate in a fastening system

In the following process, the investigation on the angle guide plate is carried out.

Figure 43 gives an overview of the modelling workflow with a focus on the analysis of the angle guide plate under dynamic and static loads acting on the rail head.
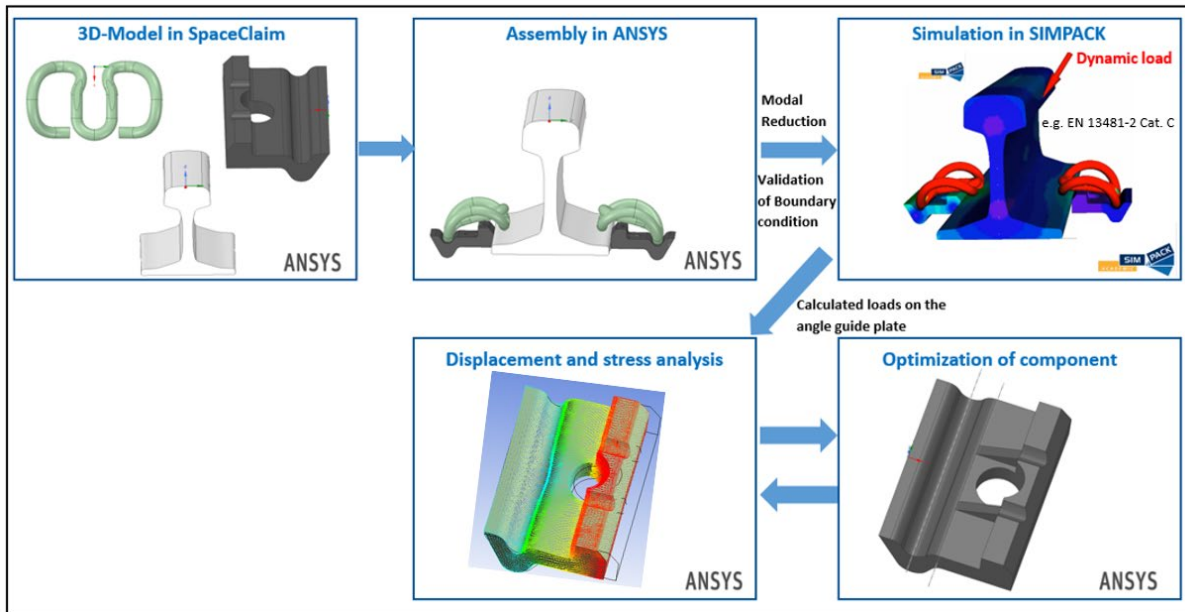
Figure 43: Workflow for the analysis of the angle guide plate under static and dynamic and loads

As it was mentioned before, verification of the boundary conditions is the essential parts of the modelling, which strongly influence the results. A measurement on the test track of TU Munich equipped with Skl 14 system was carried out in [41]. According to the test results, the average strain of the angle guide plate shows a linear behavior when a lateral load of 12.6 kN attacked the rail head (which gave a maximum lateral rail seat load of about 7.6 kN). The average strain on the angle guide plate at the load acting point was determined as 0.87‰. This is an important input to define the material properties in the 3D angle guide plate model and to validate the calculated results. It should be noted that the calculated lateral stiffness is specified by the product installed in the test track, its geometry and material mix (e.g. polyamide with glass fiber), the friction values and initial assembled position influenced by environment and installation process.

Figure 44 shows the workflow of the calculation and verification of the boundary conditions using the full 3D model. The position C is the position exactly below the force applying position. On each angle guide plate, there are two strain gauges glued at both sides marked C-1, C-2; D-1, D-2; E-1, E-2.

Under ideal situation, without initial imperfection (e.g. a gap between angle guide plate and rail foot), the two strain gauges at C should show identical deformations. However, in position C-1 the compression under the same lateral load was smaller than in position C-2. From this it can be concluded that there is a gap at least at position C-1.
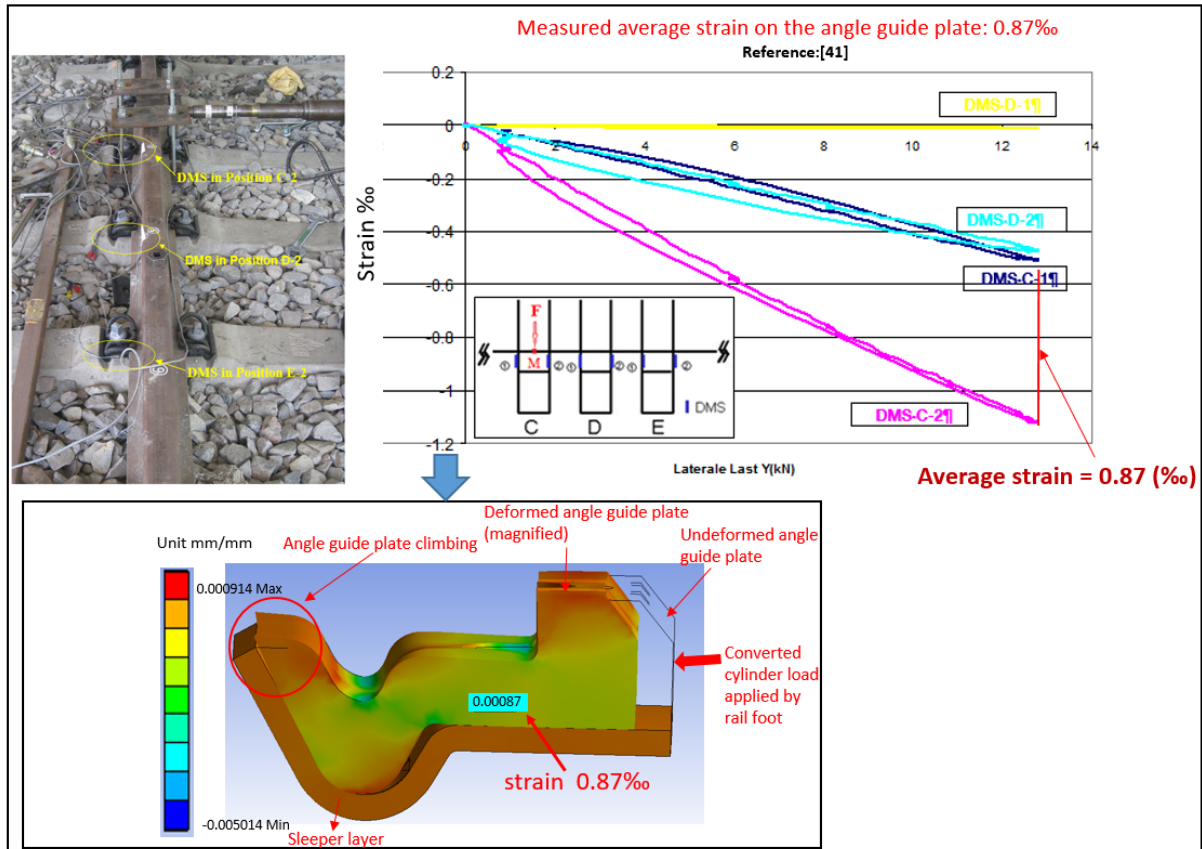
Figure 44: Model verification of the contact and boundary conditions through the laboratory test

The definitions of the contact conditions and friction coefficient influence the clamping behaviour of the angle guide plate and lead to a variation of the calculated stiffness. Based on the complete 3D model, the lateral stiffness of the angle guide can be calculated by the load acting on the angle guide plate and the corresponding average deformation. The calculated lateral stiffness of the angle guide is in a range of 70 kN/mm to 80 kN/mm, which meets the stated range of 50 kN/mm to 80 kN/mm defined in documentation [10] [12]. For the modelling validation work in chapter 5.5, a linear lateral stiffness of 70 kN/mm was used to compare with the laboratory test results recorded after load 10 cycles (contact between the rail foot and the angle guide plate).

One of the essential function of a 3D modelling method is to perform the optimization of the geometric design. Figure 45 shows the results with and without reinforcement near the screw hole under the converted load 40.6 kN as defined in DIN EN 13481-2 category C.
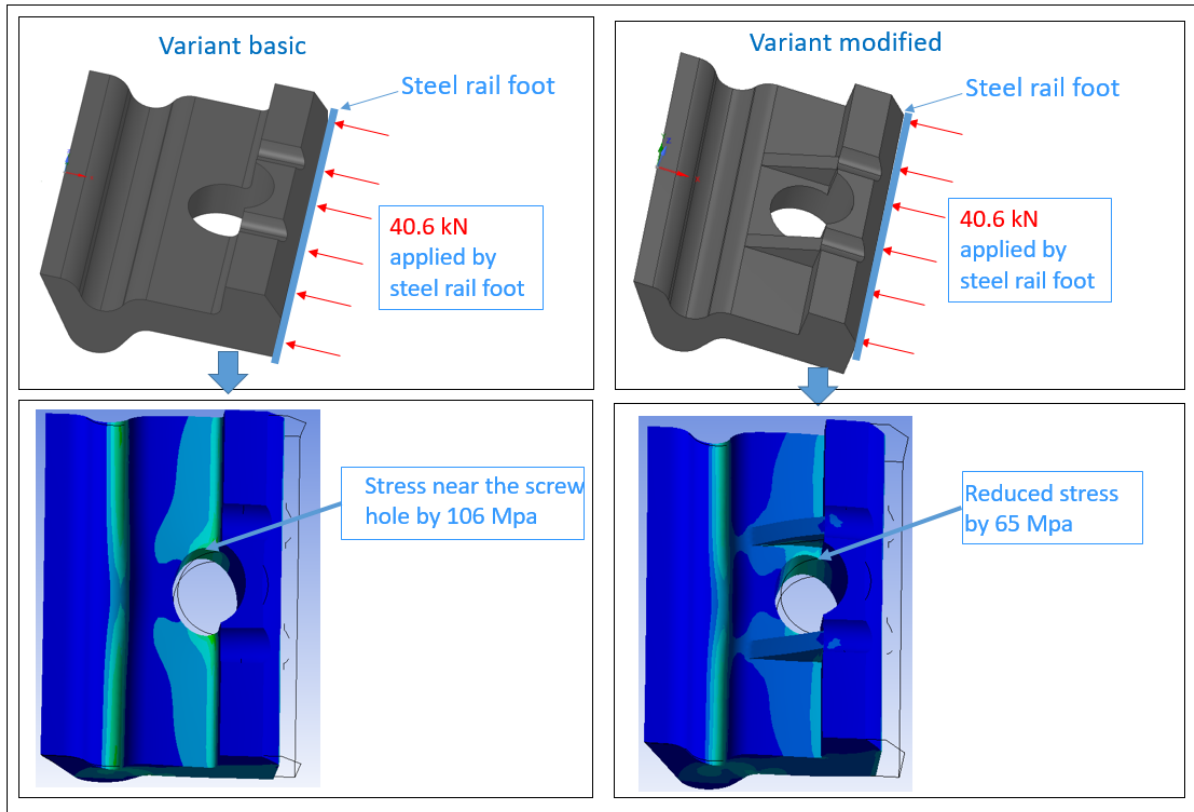
Figure 45: Comparison of stresses near the screw hole with and without reinforcement

It can be seen that the design of reinforcement near the screw hole helps to reduce the stress concentration at the edge of the screw hole.

The reinforcement near the screw hole is proposed to protect a higher stress concentration and to avoid direct shear loading on the screw spike caused by large deformation of the angle guide plate in extreme load cases. The lateral load should be transferred as much as possible via the angle guide plate into the sleeper and the shear load on the screw spike should be avoided.

5.4.4 Evaluation of the lateral stiffness of the rail fastening system

Based on the previously described investigation on the specified resistance force of the tension clamp and the angle guide plate, a general nonlinear diagram of lateral resistance force vs lateral rail movement is developed to evaluate the lateral stiffness. It is assumed that 1) there is no relative movement between the tension clamp toes and the rail foot during the rail movement provided by the gap between rail foot and angle guide plate; 2) if a stiff rail pad is used there is only friction force between the rail foot and the rail pad.
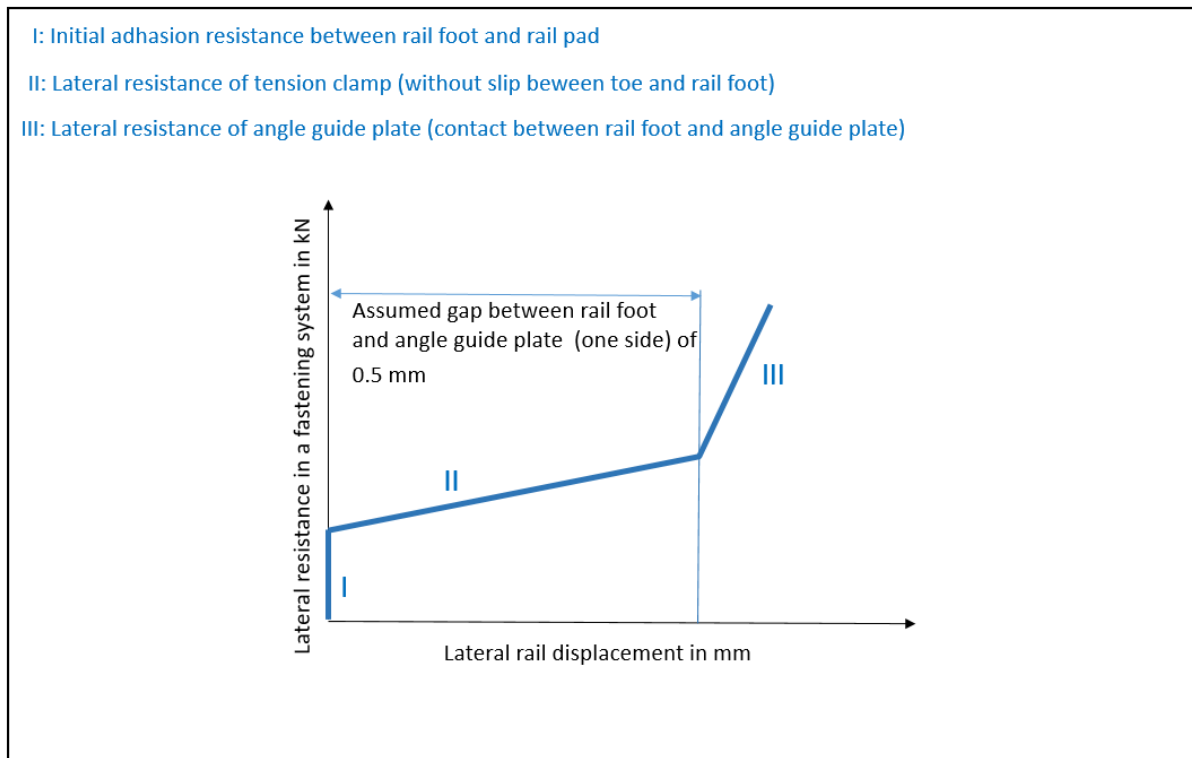
Figure 46: Non-linear lateral stiffness of a rail fastening system

On the straight track or track with large curve, both the lateral resistance force of the fastening system and lateral wheel/rail contact force are low. The vehicle is travelling with a high speed. The influence of the fastening lateral stiffness on the dynamic effect of the vehicle is the critical point and is investigated in chapter 7.4 to study the critical vehicle speed with the theoretical maximal vehicle speed.

In the case of the tight curve (as defined in DIN EN 13481), the lateral fastening resistance increases due to the contribution of angle guide. On the other side, the lateral wheel/rail contact force also becomes large and the permissible vehicle speed is slow. The rail lateral movement and the corresponding load distribution of the rail to the superstructure are the critical points.

As mentioned above, the lateral stiffness of the fastening system depends on many influence factors such as the friction coefficient, relative movement and gap between the components which is strongly influenced by environmental and installation conditions, product materials and geometries. Each measurement to verify the model represents an individual case. Therefore, in the following analysis for the whole fastening system or for the vehicle/track dynamic system, a simplified linear approach of the lateral stiffness according to [9] [12] [19] [23] [46] in a range from 20 kN/mm to 80 km/mm for parameter variation is used.

As already mentioned, a linear lateral stiffness of 70 kN/mm is used for the model validation based on the laboratory test in chapter 5.5 and the calculated results agree very well with the test results. The details of the model validation are explained in the next chapter 5.5.

The individual analysis on each component described in previously research also provides evidence that the range of the lateral stiffness of the fastening system is consistent with the wide variations of the simplified linear approach in the literature review.

5.5 Validation of the virtual laboratory test of the fastening system

As it was mentioned before, to ensure the quality of the numerical model of the fastening system, the measurement results from different scenarios were used,

1) The laboratory experimentation performed in this study to examine the non-linear behavior.

2) The laboratory measurements in [12] by different static end states for large deformation.

Model validation with measurement scenario according to the laboratory experimentation performed in this study:

First, the effect of the tension clamp alone on the rail head displacement under loading will be validated through the laboratory test under using the steel angle guide and steel rail pad (not used in tracks) to check the modelling correctness of the tension clamp mechanism.
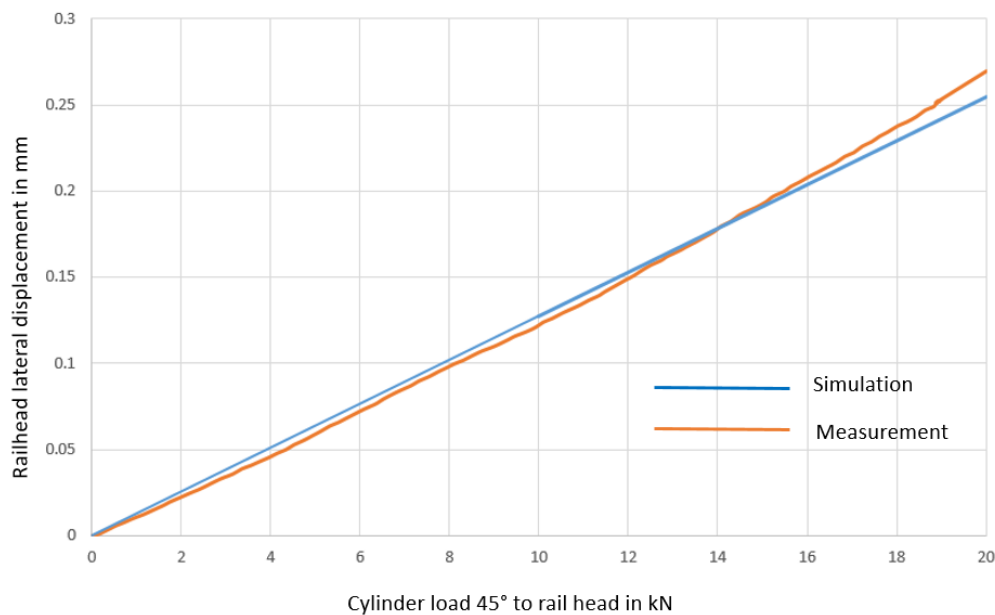
Figure 47: Railhead displacement vs. cylinder load; Skl 14 with steel rail pad and steel angle guide

After research of the tension force preload, which is corresponding to the assembly process, the same load conditions and boundary conditions in the laboratory tests described in chapter 3 are applied on the railhead. The railhead displacement vs. cylinder load diagrams of simulation and laboratory test under different rail pads are depicted in Figure 48 and Figure 49. They represent the railhead lateral displacement behaviors with varying rail pads under the same load scenario.
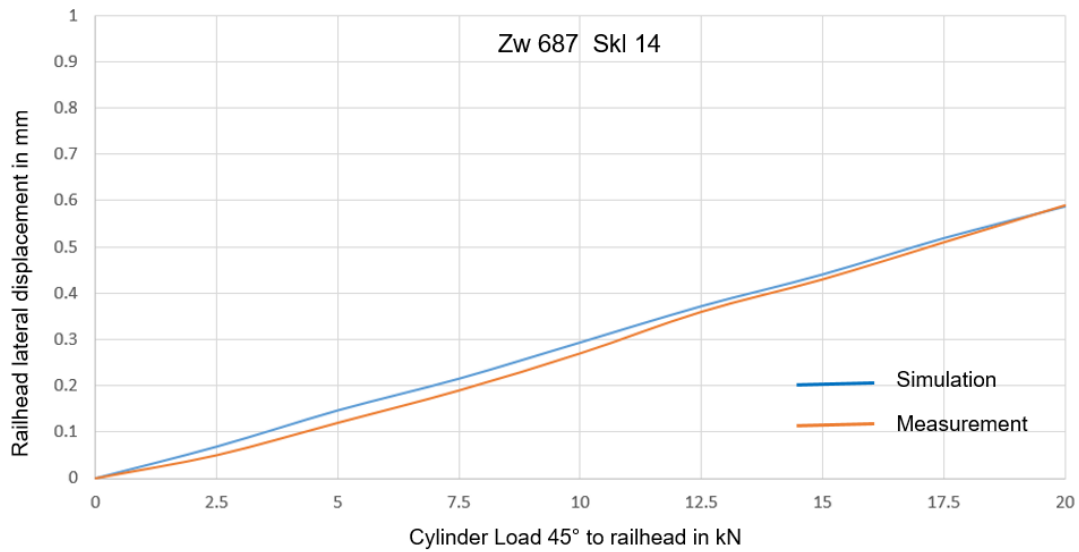
Figure 48: The rail head displacement vs. cylinder load diagram with rail pad Zw 687
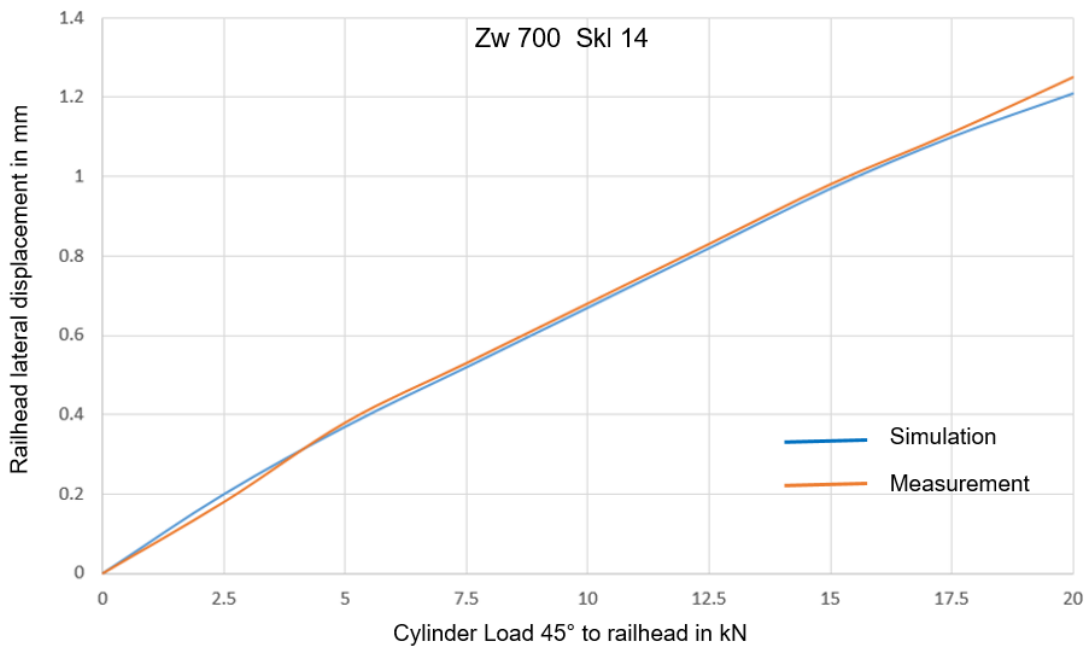
Figure 49: The rail head displacement vs. cylinder load diagram with rail pad Zw 700

It can be found that the simulation results meet the laboratory test very well under using of stiff (Zw 687) or middle stiff rail pad (Zw 700).

In case of large railhead lateral displacements (which vary depending on the rail pad product), the middle bend of the clamp will tend to touch the rail foot. This helps to protect the rail against rotation. The contact between the tension clamp middle bend and rail foot will control further rail head lateral displacement in a linear way that is no longer influenced by the non-linear properties of the rail pad.

Validation process according to the measurement scenario in [12]:

In the next step, the measured results from [12] for the fastening system Skl 21 with rail pad Zw 1000 was used to validate the numerical model in this study further. Figure 50 shows the results.
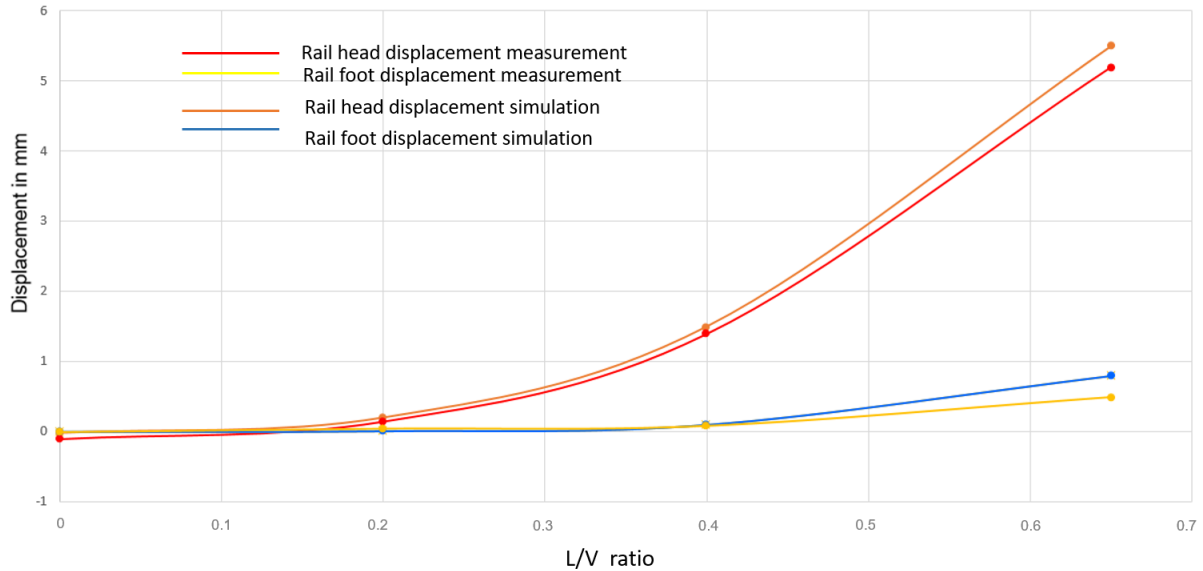
Figure 50: Comparison of lateral railhead and rail foot displacement between measurement and simulation by different L/V ratio

It should be noted that the lateral fastening stiffness in this study was taken as a simplified linear stiffness to describe the total effect of angle guide plate + assembled rail pad shear stiffnesses + tension clamp. The value used in the model for verification process is 70 kN/mm, which is within the range described in [12] and the derived lateral rail head displacements are consistent with the laboratory test results (Figure 48 to Figure 50).

Through the above validation processes in 2 different load scenarios, the model validation process of fastening system is completed and the model is ready for further use in the engineering application.

5.6 Example cases for tension clamp analysis using the virtual lab test tool

The preload plays an essential role in the resistance against the rail head rotation, which is changing the wheel/rail contact geometry. Therefor a general understanding of the relationship between the geometrical tension clamp design and the activated tension force helps to answer the following questions:

1) What is the influence of the tension clamp wire diameter increasing on the tension clamp preload?

2) What happens if the tension clamp is installed too tight or less tight?

What is the influence of the tension clamp wire diameter increasing on the tension clamp preload?

Figure 51 shows a wire diameter variation based on Skl 14 standard.

Standard SKL 14 Rendered Model

Standard SKL 14 with 15% increase in diameter Rendered Model

Figure 51: Overview of tension clamp wire diameter increasing based on Skl 14 standard

Table 10 summarizes the mass and geometry properties.

Table 10: Summary of mass and geometry properties of the tension clamp designs

Geometric Properties	SKL14 Standard	SKL14 Standard 15% ▲ Ø
Geometry		
Density (g/mm³)	0.00780	0.00780
Mass (g)	512.4	668.3
Volume (mm³)	65694.0	85681.4
Surface Area (mm²)	20483.4	23286.8

According to the Vossloh W14 Fastening System brochure [39] in Figure 52, the rail is clamped in a force-fitted way by the two spring arms showing a deflection of approximately 12 mm, which produces a tension clamp preload of approximately 9 kN for one tension clamp (4.5 kN on each tension clamp toe). The preload of the whole fastening system with two tension clamps is 18 kN.
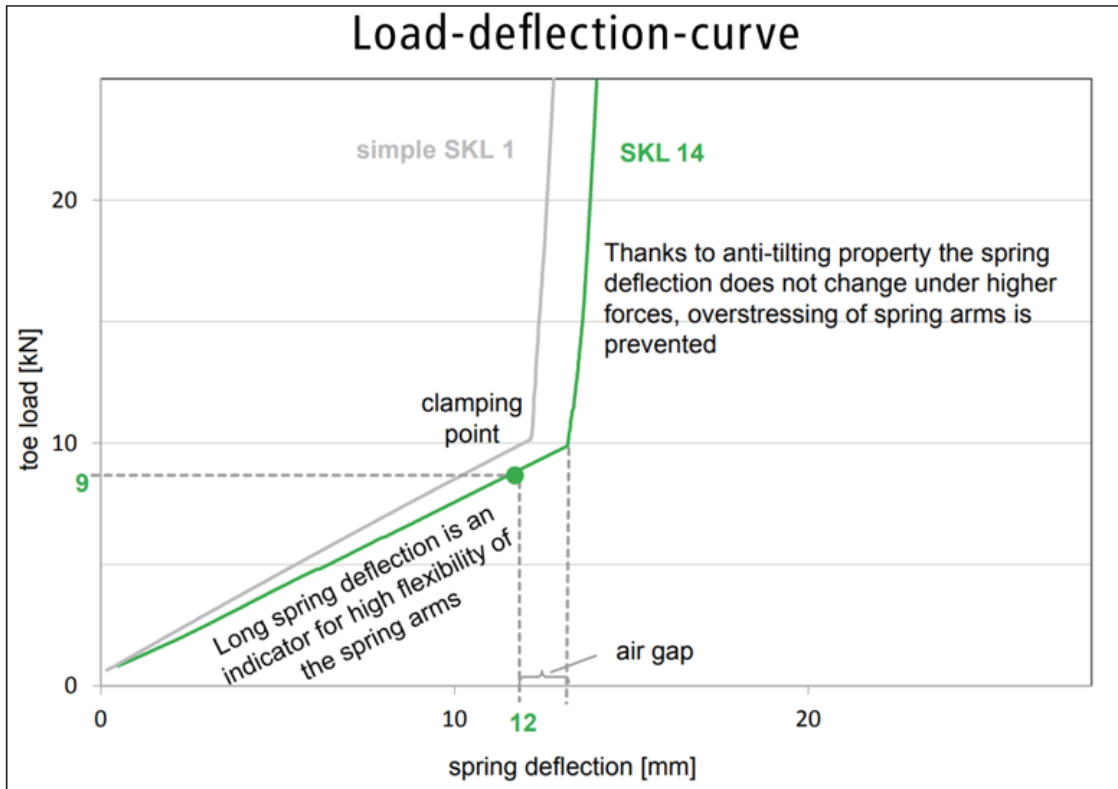
Figure 52: Loading deflection curve of Vossloh SKL 14 [39]

For both designs described in Figure 51, the middle bend of the clamp is deformed by 12 mm according in the installation process. In the assembled system, the rail pad stiffness has a slight influence on the tension clamp preload when the middle bend has the 12 mm displacement. Here for simulation, the rail pad Zw 700 was used. The individual calculated tension clamp preloads are summarized in Table 11.

Table 11: Middle bend deformation under 12 mm and the sum of tension clamp preload

Design Clamp	Displacement of Middle Bend (mm)	Forces on Each Toe (kN)	Sum of Forces (kN)
SKL 14 Standard	12	4.417+4.390+4.417+4.390	17.61
SKL 14 Standard with 15% ▲ in Ø	12.01	7.401+7.266+7.401+7.266	29.33

It can be seen that when the tension clamp wire diameter is increased by 15%, the calculated clamping force increases from 17.61 kN, based on the the Skl 14 standard, to 29.33 kN when the displacement of middle bend distance is 12 mm. This proves the functionality of the

simulation tool for calculating the influence of changes in the tension clamp geometry on the tension clamp preload.

What happens if the tension clamp is installed too tight or less tight?

Figure 53 gives an overview of the tension clamp installations using different preloads. Traffic load application is as described.
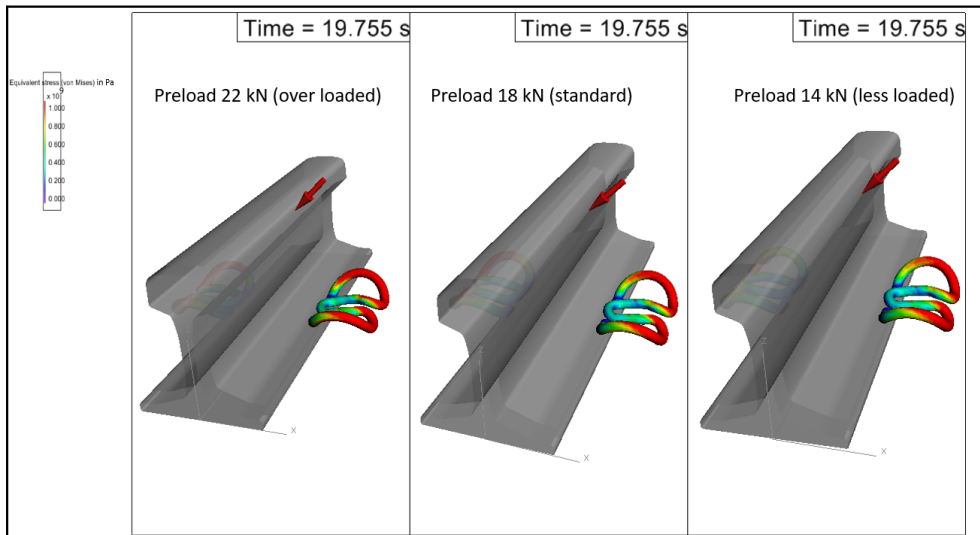
Figure 53: Illustration of the tension clamp stresses by different preloads under applied force on the rail head

Figure 54 shows the von mises stresses on the tension clamp toes and the lateral railhead displacements under pre-loading and traffic loading. It can be seen that the tension clamp with 22 kN preload (over tigtened) has a high stress but smallest rail head displacement. The large rail head displacement under traffic load of the less tightened tension clamp leads to a significant stress increase but the maximum is still smaller than the standard situation.
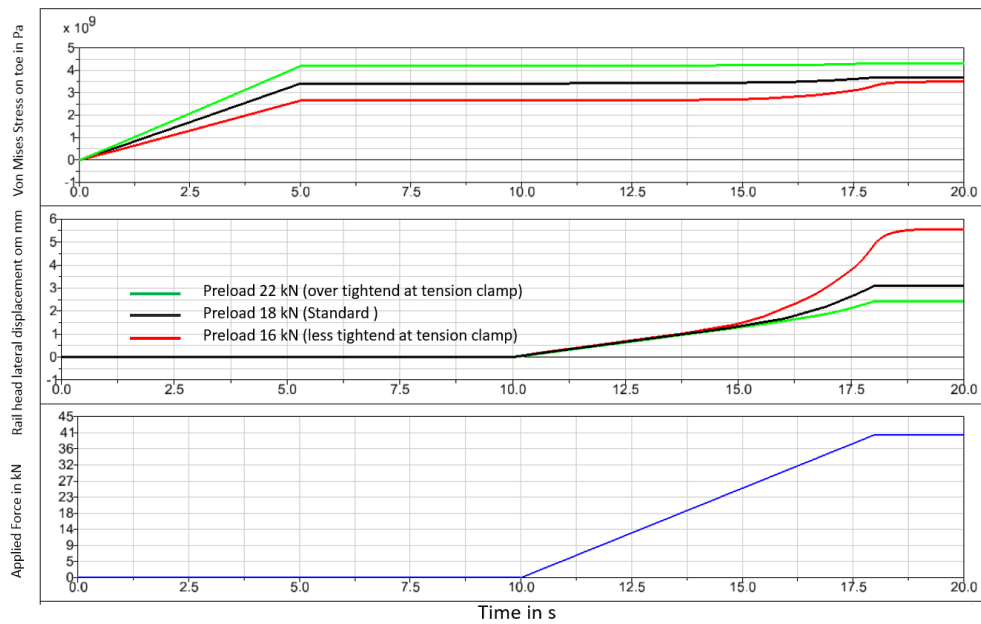
Figure 54: Results of stress on the toe of tension clamps, under assembled preload and applied force on rail head

5.7 Long rail section equipped with more support points

The lateral stiffness of one support point (fastening system) is verified through the laboratory test. In reality, many support points support the rail and the railhead lateral displacement is much smaller when the same load is applied on the rail in comparison with the fastening test according to the standard of EN 13481. The railhead lateral movement with a variation of the number of support points up to a 12 m rail section under defined load is calculated by the numerical model.

It is found that the rail web flexibility also contributes a little to the rail head lateral displacement. In case of a very stiff rail pad, most of the rail head lateral displacement is caused by the flexibility of the rail itself. Therefore, it is essential to use the full 3D rail model (described in section 5.1) to receive precise result. With reference to the standard fastening system Skl 14, different preloads and stiffness had been studied e.g. the Skl 14, Skl 21 and Skl 28 with preloading of 9 kN, 10 kN and 14 kN.

Figure 55 shows a comparison of railhead lateral displacement by using different tension clamp Skl 14, Skl 21 and Skl 28 in combination with rail pad Zw 700.

Figure 55: Rail head lateral displacement of 12 meters rail section with different tension clamps

It can be found that the Skl 28 has the minimal rail head lateral displacement under the two points loading.

The influence of lateral stiffness of the angled guide plate on the lateral rail head displacement needs to be studied. According to the documentation [12] the standard fastening lateral stiffness varies in a range from 50 kN to 80 kN/mm for ballasted fastening system.

In the modelling, the effect of the angle guide plate was modelled as a lateral force element. Figure 56 illustrates the parameter variation of the lateral fastening system stiffness (angle guide plate + rail pad assembled + tension clamp) of 50 kN/mm, 70 kN/mm and 100 kN/mm.
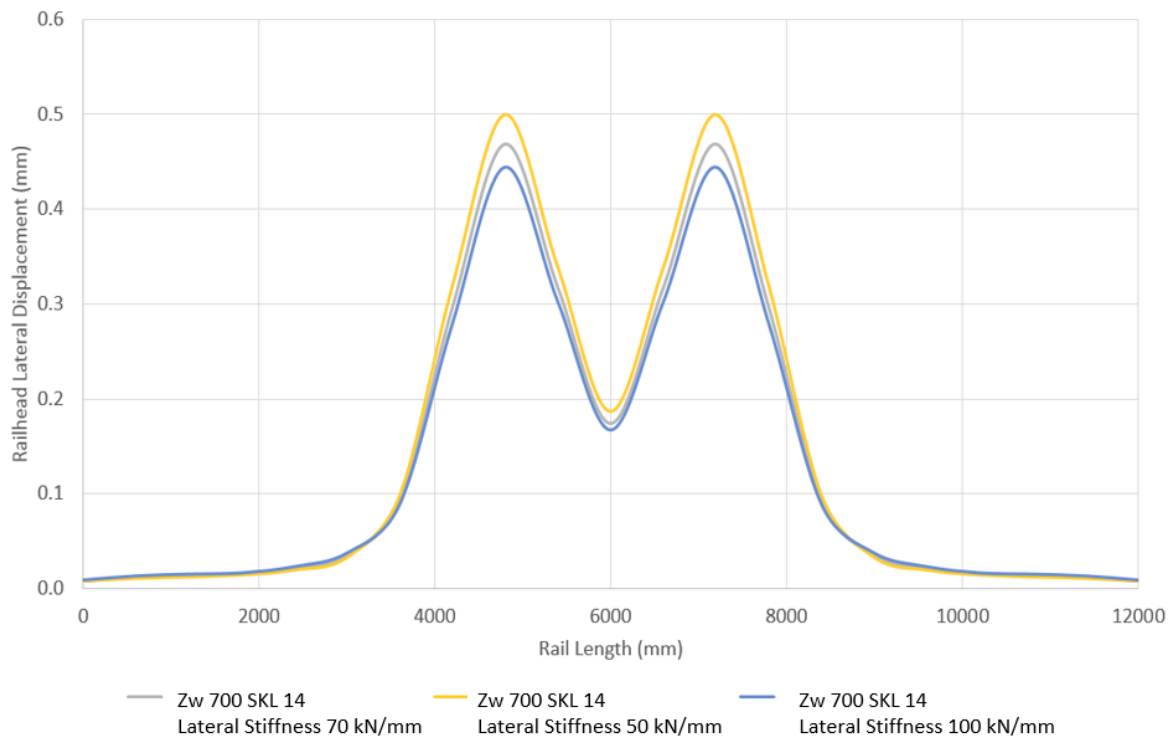
Figure 56: Railhead lateral displacement of 12 meters rail section with different fastening lateral stiffness (angle guide + rail pad assembled+ tension clamp) with Skl 14 tension clamp

The other calculated results using the long rail section with parameter variation are provided in appendix 8.

5.8 Track model under consideration of the sleeper – ballast interface

A track model was created with consideration of the fastening system and of the sleeper support stiffness (with focus on lateral support stiffness).

The initial track model (Figure 57) consists of 18 sleepers and 12 meters' rails built in a MBS environment in SIMPACK which had been extended to 21 sleepers (Figure 58). The model is representing the setup of the test track of the Institute of Road, Railway and Airfield Construction of TU Munich, where a lot of tests for static analysis were carried out [12]. Also dynamic analyses in the acoustic range were also performed using this test track [14] [15] [16].

The modelling of the basic subsystems, sleeper and rail, and the corresponding validation process is described in chapter 5.1.

Figure 57: Track model for calculation of lateral bending
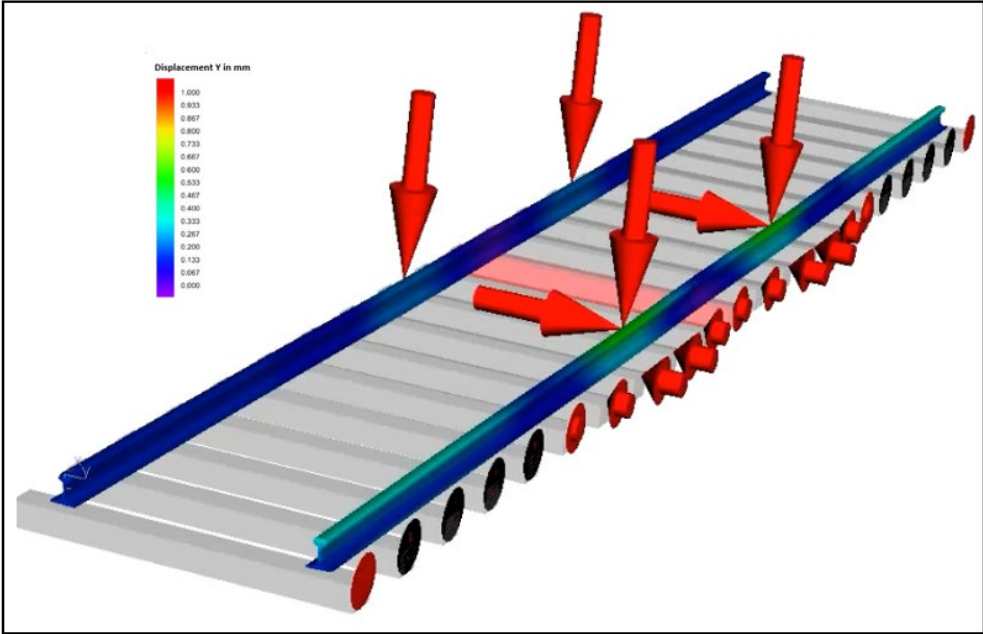
Figure 58: Track model for calculation of the sleeper lateral displacement

The documentation [19] states that the sleeper lateral resistance varies by large amount caused by its intricate mechanisms and strong deviation of conditions. Different values or ranges of stiffness of lateral sleeper support under traffic load conditions are known:

1) 37 kN/mm is used in the Manchester Benchmarks for rail vehicle simulation [46].

2) A range of 25-40 kN/mm is given by [12] [18].

3) In [19] is using 40 kN/mm for vehicle-track interaction simulation.

Documentation [20] developed a diagram (see Figure 59) to perform track lateral accumulated deterioration calculations. It gives a simplified theoretical relationship between the sleeper lateral resistance in the unloaded (blue line) and loaded (red line) case. According to theory the loaded sleeper resistance is determined using the characteristic of the unloaded case, increased with the help of multiplication factors. This approach was used in this study to integrate the sleeper lateral resistance in the numerical model considering the actual vertical load distribution by the track.
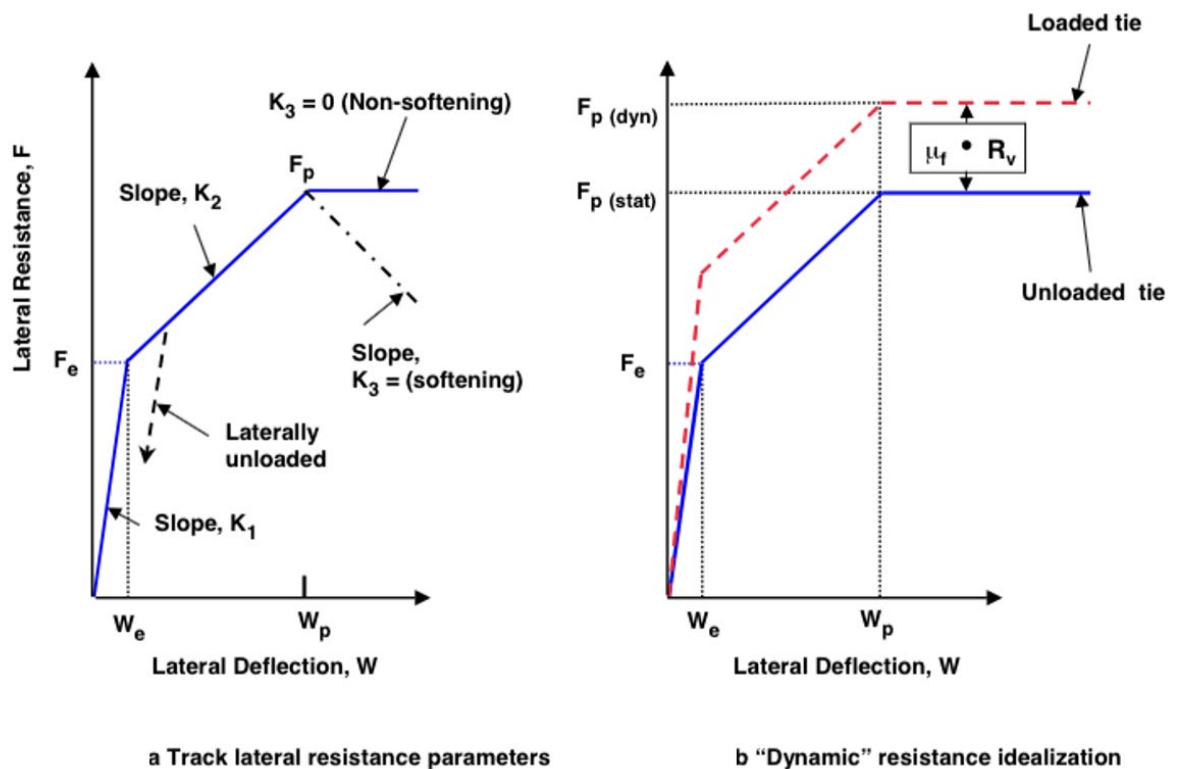
Figure 59: Track lateral resistance parameters [20]

F_e: elastic resistance, W_e: elastic displacement, F_p: peak resistance, W_p: displacement at peak, μ_f: sleeper-ballasted friction coefficient.

Figure 60 shows an example of measured lateral sleeper resistance functions representing different track conditions using different tamping methods. The red line at 2 mm follows the general definition of the sleeper lateral resistance force used as input for the lateral track stability calculations to demonstrate safety against track buckling in unloaded conditions

(without traffic loading) [17] [18]. The blue line at 0.25 mm is used to determine the elastic displacement W_e for this study. The elastic displacement section up to W_e plays an essential role on the track/vehicle dynamics with respect to potential accumulative lateral shift of the sleeper position which leads to increasing effort of maintenance. The larger the linear elastic displacement and the higher the peak value, the better is the situation with respect to track quality degradation [19]. Using under sleeper pad is in line with this statement. The linear elastic displacement and the corresponding peak value should also be considered based on the measured data of sleeper lateral displacement in unloaded case.
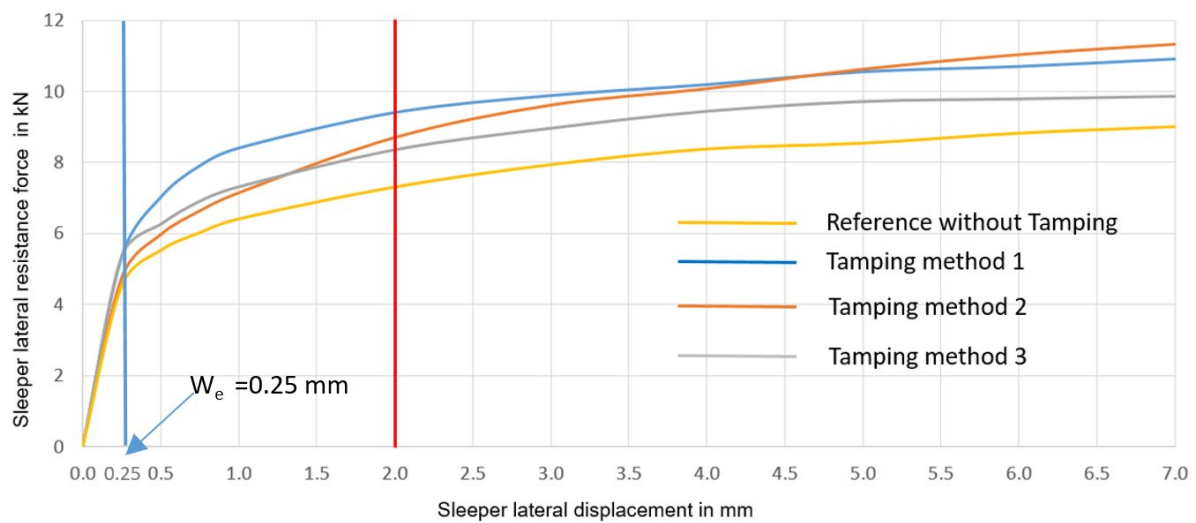
Figure 60: Sleeper lateral resistance force vs displacement diagram without traffic loading

Figure 61 shows the calculated multi-linear stiffness in unloaded case representing the force-displacement behavior of the sleeper.
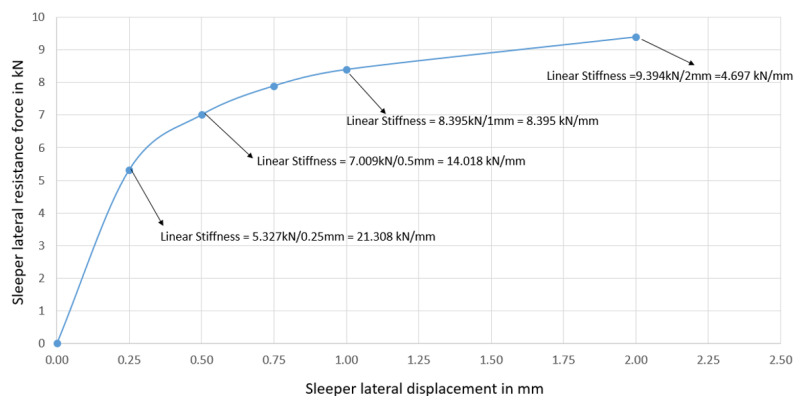
Figure 61: Multi-linear lateral stiffness representing the displacement dependent on lateral sleeper resistance without vertical load

A case study using the combination of the measured sleeper lateral stiffness of 21.3 kN / mm at 0.25 mm displacement in unloaded case (Figure 61) and 25 kN/mm to 40 kN/mm in loaded case [12] [18] was performed in this study (Figure 58, Figure 62), which can establish a simplified relationship between the vertical load distribution and the lateral sleeper support stiffness considering different fastening systems.

Figure 62 shows the calculated lateral sleeper support stiffness in kN/mm under 200 kN axle load (100 kN per wheel) with a wheelbase of 3 m (e.g. locomotive 1116). The Figure shows the situation of one rail of the track.

Sum of vertical load both side rails (kN):	3.46	2.48	1.68	1.7	4.7	13.7	37.18	60.5	60.5	38.52	26.7	38.52	60.5	60.5	37.18	13.7	4.7	1.7	1.68	2.48	3.46
Proportion:	1	0.72	0.49	0.49	0.08	0.23	0.62	1	1	0.64	0.44	0.64	1	1	0.62	0.23	0.08	0.49	0.49	0.72	1
Assumed sleeper lateral support stiffness under axle load: 25 kN/mm	21.3	15.3	10.4	10.4	21.6	22.2	23.6	25	25	23.7	22.9	23.7	25	25	23.6	22.2	21.6	10.4	10.4	15.3	21.3
Assumed sleeper lateral support stiffness under axle load: 30 kN/mm	21.3	15.3	10.4	10.4	22	23.3	26.7	30	30	26.9	25.1	26.9	30	30	26.7	23.3	22	10.4	10.4	15.3	21.3
Assumed sleeper lateral support stiffness under axle load: 40 kN/mm	21.3	15.3	10.4	10.4	22.8	25.6	32.9	40	40	33.3	29.5	33.3	40	40	32.9	25.6	22.8	10.4	10.4	15.3	21.3

Figure 62: Determination of the sleeper lateral support stiffness under consideration of the vertical axle load distribution on track (illustrated on one side)

According to the formula of Prud'homme referenced in [23], the limit value for the total lateral traffic loading force to protect the superstructure against lateral (plastic) deformation is described as:

(∑Y2m) lim =α (10+2Q/3) [kN];

Where coefficient α=1 (for train driven by the locomotive, general passenger train and multi-power unit train) is used in this case study; α=0.85 (for cargo train).

For dynamic calculation the force is distributed along 2m rail length.

The lateral force applied on the track model under 200 kN axle load is calculated as 77 kN.

The simulation results show that the influence of variation in sleeper lateral support stiffness under axle load (from 25 kN/mm to 40 kN/mm) on the rail head lateral displacement (related to the sleeper) is less than the variation in pad-stiffness from hard (Zw 687) to soft (e.g. Zw 1000). The softer the sleeper lateral support, the better the lateral load distribution and the smaller the rail head lateral displacement (related to the sleeper) on the support point of the fastening system.

6. Modelling of rail-wheel contact and creation of track-vehicle system dynamic model

6.1 Investigation on wheel-rail contact point

Since the wheel-rail contact position is one of the important parameters to calculate the rail lateral displacement or rail rotation, a numerical simulation had been performed based on the test performed by [12]. Figure 63 depicts the measurement setup. The line of e=0 is the centre line of the rail head profile. The positive value of e determines a position which is at rail outside. The corresponding measured rail head lateral displacement under different contact points and load application conditions in the documentation were used as reference to verify the numerical model which created in this study.
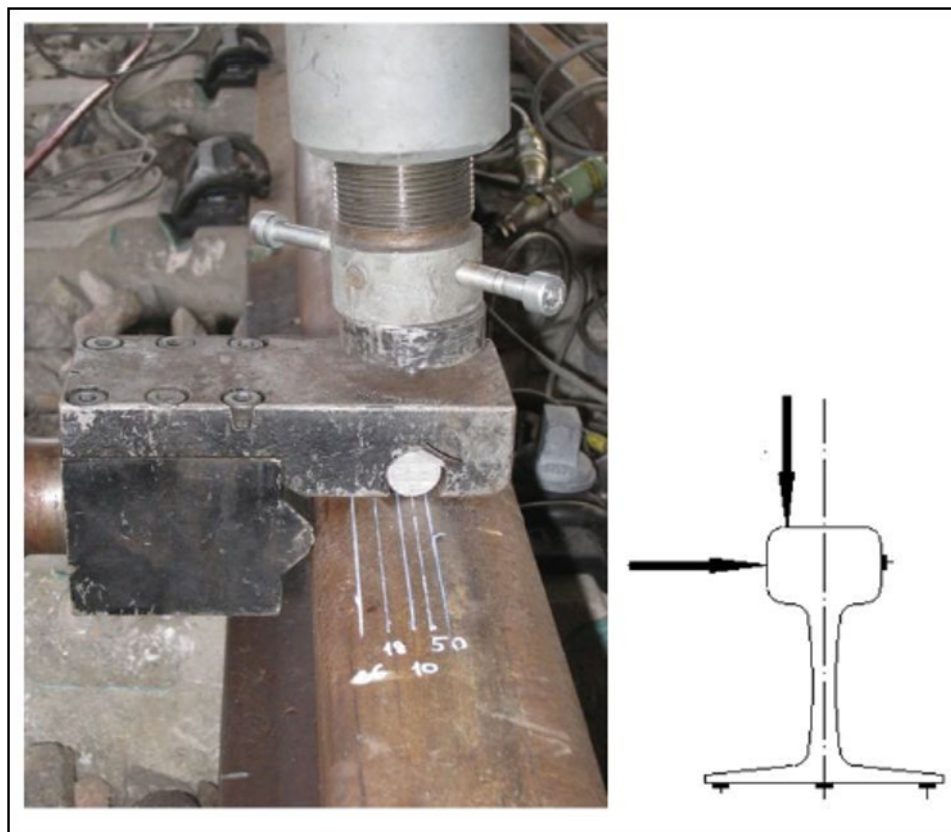
Figure 63: Measurement setup as used by [12]

Figure 64 shows the numerical calculated wheel/rail contact positions under variation of the different track gauges.
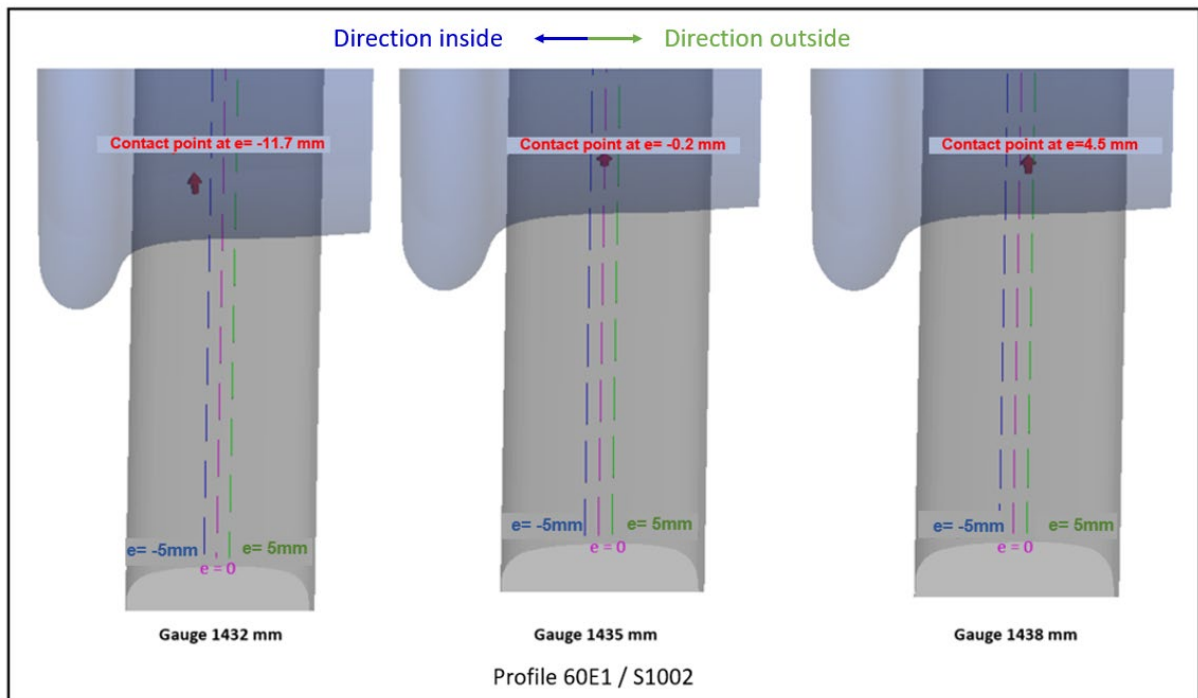
Figure 64: Rail contact point under different gauges (defined as right side rail)

By the normal case of a standard gauge by 1435mm, the contact point is at -0.2 mm direction inside based on the rail head middle line (e=0). At the gauge of 1432 mm, the contact point is at -11.7 mm direction inside and at the gauge of 1438 mm, the contact point is at 4.5 mm direction outside.

By gauge narrowing, the contact points on the railhead tend to the track center direction (direction inside) and by gauge widening, the contact points on the railhead tend to the rail outside direction.

In the next step, the influence of the rail inclination on the contact point is investigated (Figure 65).

By the rail inclination of 0, the contact point is at -10.2 mm direction inside and by rail inclination of 1:10, the contact point is at 14.9 mm direction outside.

It can be seen that by decreasing of the rail inclination, the contact point points on the railhead tend to the direction inside and by the increasing of the rail inclination, the contact points on the railhead tend to the rail outside direction.
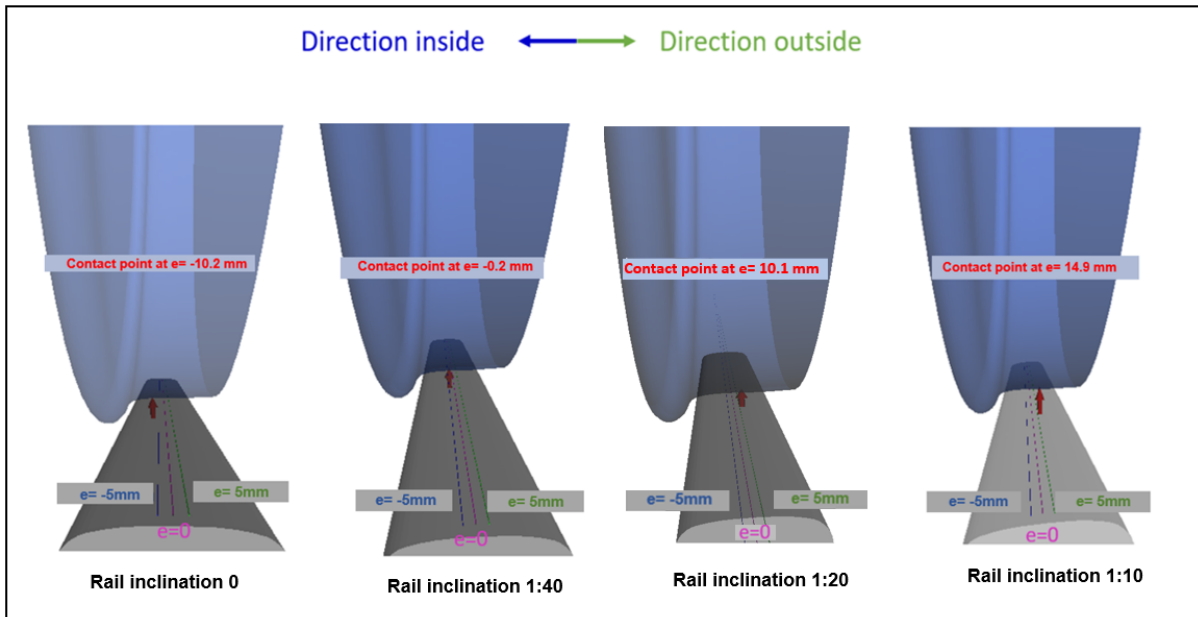
Figure 65: Rail contact point under different rail inclination (defined as right side rail)

It can be seen that the changing of the rail gauge and the rail inclination has an influence on the contact point of the rail.

The function to calculate the contact point corresponding the rail inclination and gauge changing is an essential key point in the numerical model for the connection of the superstructure and the vehicle model. Based on this, the whole mechanism of the rail fastening system and sleeper movement can be created in the numerical model.

As shown in Figure 64 and 65, one can obtain a general overview of the contact point positions under different parameter combinations.

To investigate the basic vehicle running behavior using the numerical model, a single wheelset model with a specific wheel profile (cone profile) according to the theory described in [5] is used in the next chapter.

6.2 Validation of the single wheelset model using classic theory

A simple numerical model using a rigid wheelset with conical wheel profiles is shown in Figure 66. Along a straight track, an initial lateral shift of the axle is needed to demonstrate the sine-shaped wheelset run.
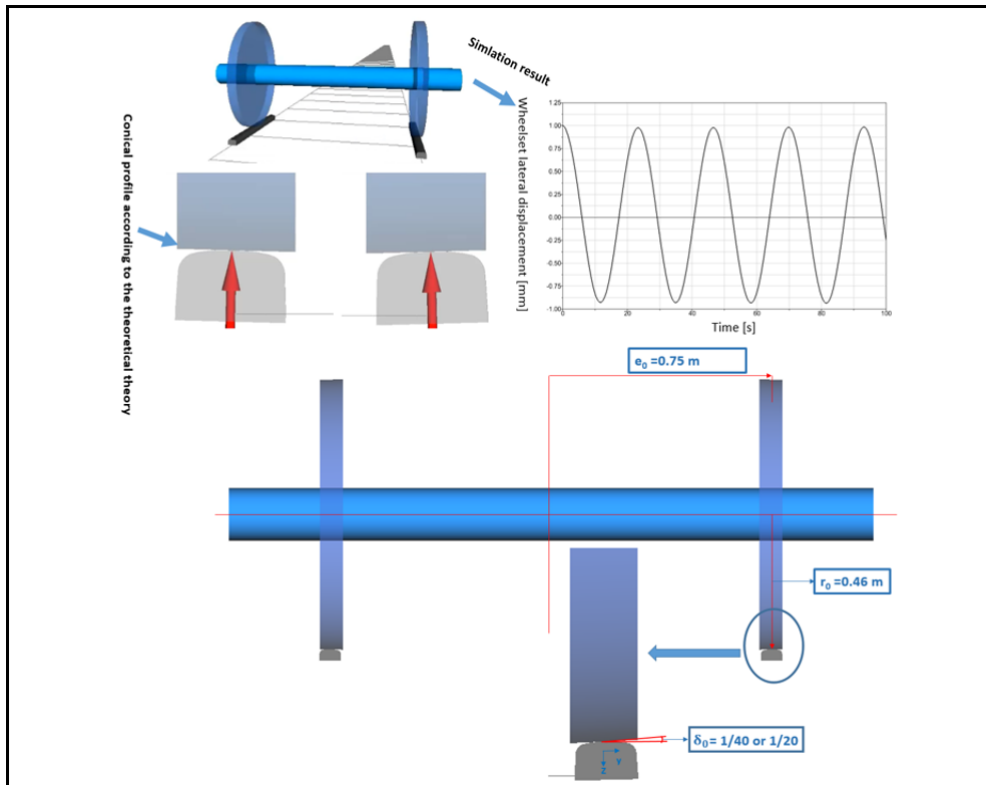
Figure 66: Sine run of a simple MBS numerical model according to classic theory (no damping)

The wavelength according to classic theory is described as $L_s = 2\pi\sqrt{\frac{r_0 e_0}{\delta_0}}$ in [5], r_0 is the wheel radius; e_0 is a distance of the wheel contact point to the track centre; δ_0 is the contact surface inclination, see Figure 66.

The wheelset is now passing through a curve with radius of 1000 m and vehicle velocity is 1 m/s. The track section starts with a 10 m straight track first in order to give an initial stabile position of the wheelset and to compare the results with the curved track. The parameters r_0=0.46 m and $e_0 = 0.75$ m are kept constant. The selected test case includes a variation of δ_0 (1/20; 1/40), see Figure 67.

The chart contains the following embedded equations and labels:

$$L_s = 2\pi\sqrt{\frac{r_0 e_0}{\delta_0}} = 2\pi\sqrt{\frac{0.46 * 0.753}{1/20}} = 16.5mm$$

Legend: Simulation contact angle $\delta_0=1/20$; Simulation contact angle $\delta_0=1/40$

Y-axis: Wheelset lateral displacement related to track center in mm

X-axis: Way in m

16.5 m

23.4 m

$$L_s = 2\pi\sqrt{\frac{r_0 e_0}{\delta_0}} = 2\pi\sqrt{\frac{0.46 * 0.753}{1/40}} = 23.4mm$$

Figure 67: Comparison of classic theory and simulation of single wheelset running along a curve

R=1000 m (no damping). Lateral excitation by a sudden change of R = 1000 m after a 10 m straight section

When the wheel goes through the curve, the difference of the rolling radius between the outer and inner wheel and the rail contact positions can be calculated by MBS using a single wheelset model. The wavelength of the sinus run determined by MBS matches with the formula of the classic theory. Conical wheel profiles are not pre-defined in the database of the MBS software SIMPACK. Therefore, the corresponding conical profiles were created in this work in order to validate the basic numerical model with the classic theory. Initiated by track irregularities, the sinus run creates dynamic track loads in the lateral direction.

It should be noted that:

1) In reality, the sinus run motion is damped through the primary suspension system and wheel/contact friction. This is integrated in the newly developed MBS-Modell

2) The rail is considered rigid in the classic theory and the changing of the rail/wheel contact condition by the railhead lateral motion of a flexible track system is not considered. The following chapter 6.3 will study the influence of changing rail head position on the equivalent conicity.

6.3 Modelling and calculation of the conicity under consideration of the rail head lateral displacement by rail lateral movement and rail rotation

The lateral rail head displacement leads to a changing of the rail/wheel contact conicity. The lateral railhead displacement is caused by the lateral rail movement and the rail rotation. In Germany, the rail has an initial rail inclination of 1:40. The key point of the interface of the lateral stiffness of the superstructure and the vehicle running behavior is the rail head lateral displacement and it is the resultant of the rail lateral displacement and rail rotation. It is important to understand the contribution of the rail head lateral displacement by the contribution of the rotation. To get a quick overview, a model with the real rail profile in consideration of the gauge measurement point (14 mm under the top of rail) at the rail head has been developed. Figure 68 shows the relationship between the rail rotation angle and the railhead lateral displacement based on the initial rail inclination. A calculation with the corresponding updated parameters was undertaken in this work, using the wheel profile S1002 and the rail profile 60 E1.
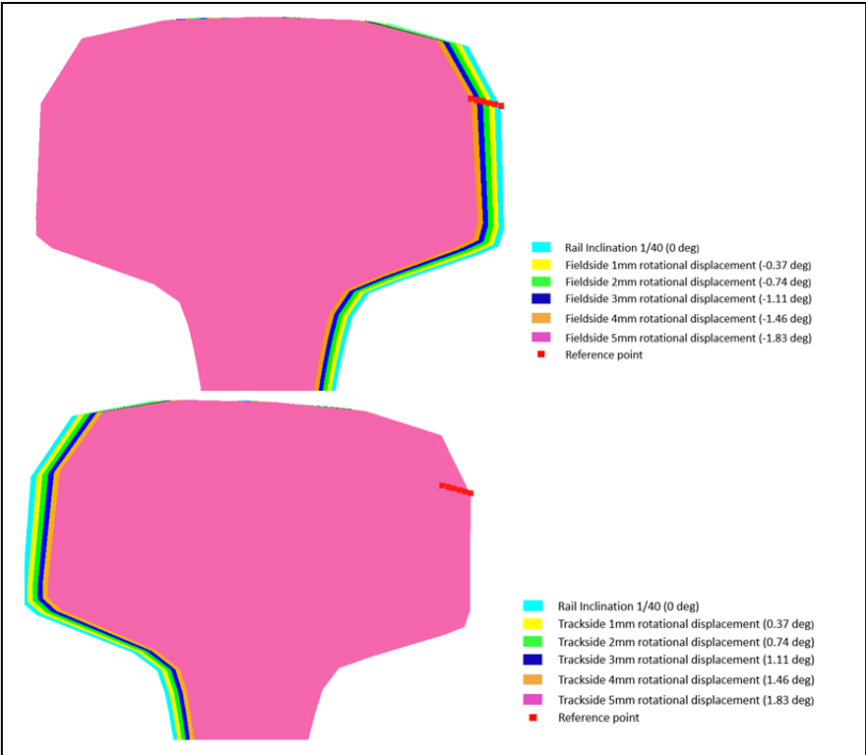
Figure 68: Relationship between rail rotation angle and railhead lateral displacement

In the next step, the wheel/rail contact is established and research for the equivalent conicity is performed. In this case, the wheel position is fixed and the rail is adjusted with different lateral displacements and angles of rotation.

6.3 Modelling and calculation of the conicity under consideration of the rail head lateral displacement by rail lateral movement and rail rotation

The changing of the equivalent conicity caused by railhead lateral displacement by rail rotation and rail lateral movement under different gauges is shown in Figure 69 and Figure 70.
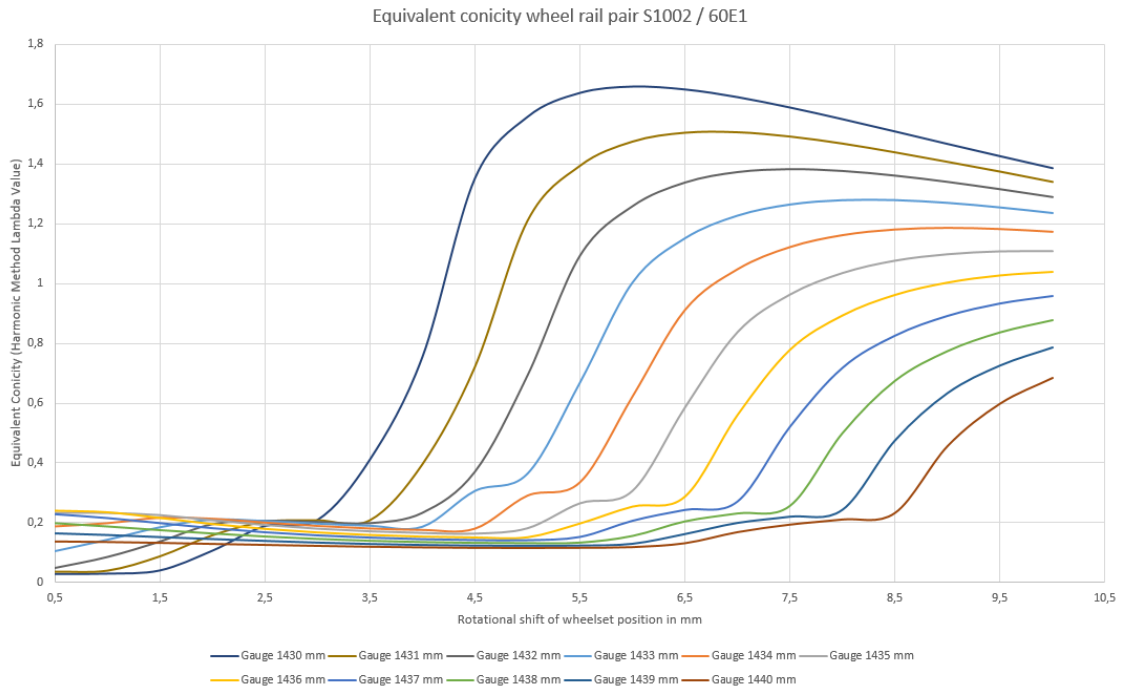
Figure 69: Equivalent conicity by railhead rotational lateral shift under different gauges
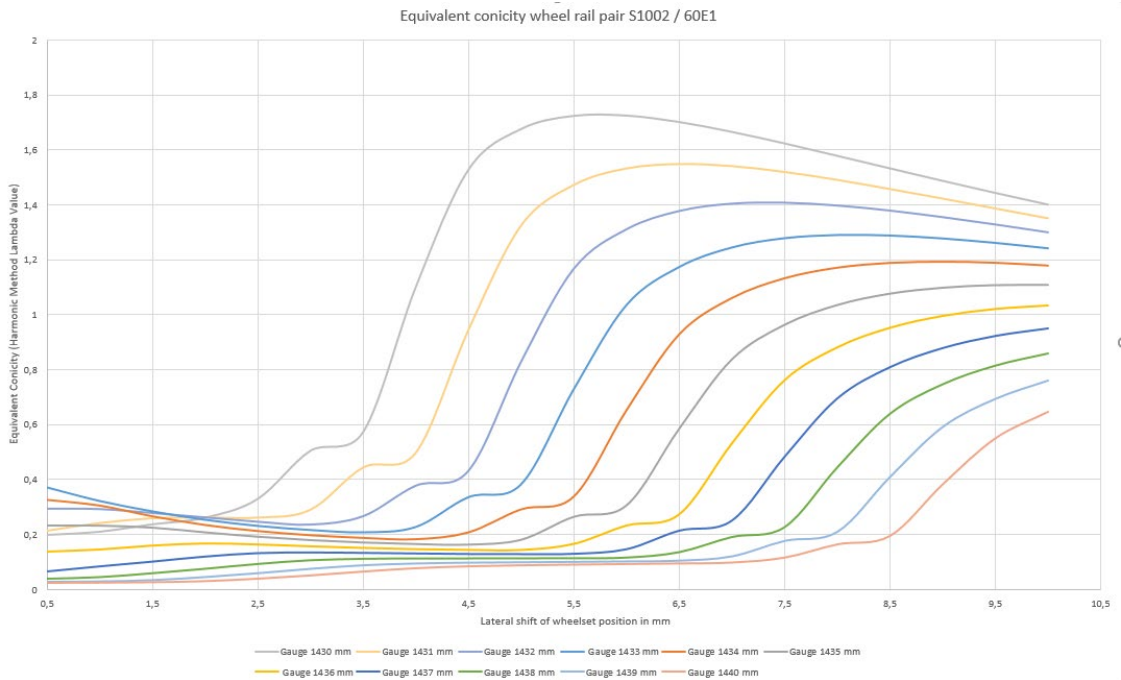
Figure 70: Equivalent conicity by railhead lateral shift under different gauges

The track geometry reference in the model is the standard gauge 1435 mm, used as a comparison benchmark (the lateral rail movement and the rail rotation are set to zero), the diagram of equivalent conicity versus displacement is depicted in Figure 71.

Figure 72 illustrates the effects of gauge narrowing and widening. Table 10 summarizes the equivalent conicity values and the changing ratios in Figure 72. It must be noted that the equivalent conicity values of Table 12 had been calculated using a 3 mm lateral off-set of the wheel set.
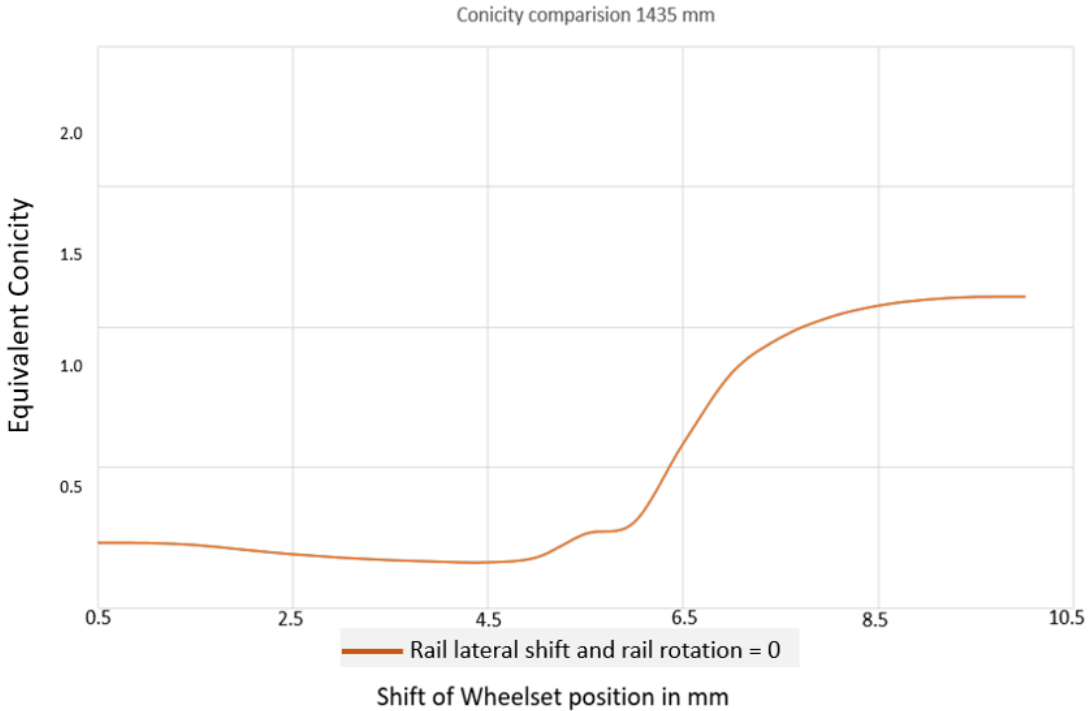
Figure 71: Effect of wheel set position on equivalent conicity at gauge 1435 mm (Comparison benchmark, no rail rotation and lateral rail shift)

Figure 72: Equivalent conicity affected by rail rotation and rail lateral movement (standard gauge)

Table 12: Change of equivalent conicity based on gauge narrowing and widening (reference is standard gauge 1435 mm)

Gauge		Equivalent Conicity at 3 mm amplitude		C_L-C_R	C_L-C_{1435} at 3mm amplitude		C_R-C_{1435} at 3mm amplitude	
mm		Lateral (C_L)	Rotational (C_R)	at 3mm amplitude	Value	Ratio	Value	Ratio
Narrowing	1431	0.291494	0.206737	0.084757	0.113054	63%	0.028297	16%
	1432	0.237403	0.202512	0.034891	0.058963	33%	0.024072	13%
	1433	0.216987	0.196103	0.020884	0.038547	22%	0.017663	10%
	1434	0.197951	0.187758	0.010193	0.019511	11%	0.009318	5%
Normal	1435	0.17844	0.17844	0	0	0%	0	0%
Widening	1436	0.15741	0.168151	-0.010741	-0.02103	-12%	-0.010289	-6%
	1437	0.133978	0.156726	-0.022748	-0.044462	-25%	-0.021714	-12%
	1438	0.106942	0.145044	-0.038102	-0.071498	-40%	-0.033396	-19%
	1439	0.0762817	0.132964	-0.0566823	-0.1021583	-57%	-0.045476	-25%

C_L in Table 12 demonstrates the equivalent conicity affected by lateral rail shift and C_R affected by rail rotation.

It can be concluded that the change of equivalent conicity caused by limited rail rotation

(+/- 1 mm lateral) is small (6%), and by the lateral rail movement is 12%.

In consideration of significant railhead lateral displacement up to 4 mm, the lateral rail movement has more effect on the equivalent conicity changing than the rail rotation considering the same lateral railhead displacement.

It can be concluded that the rail rotation and the lateral rail motion are affecting the equivalent conicity. Therefore, the rail motions caused by the wheel-rail contact force should be limited. The major influencing factors of the rail head rotation are the rail pad stiffness and the tension clamp preload forces (see chapter 5.5).

6.4 Modelling of the Vehicle

There are two vehicle models applied in this study. One model is based on the modified SIMPACK Training Model [42] [43], and the other one is a locomotive model type 1116 based on [12], see Figures 73 and 74.

Based on the predefined fastening system model and the wheel-rail contact, the vehicle-track interaction model with a focus on the lateral dynamic is established.
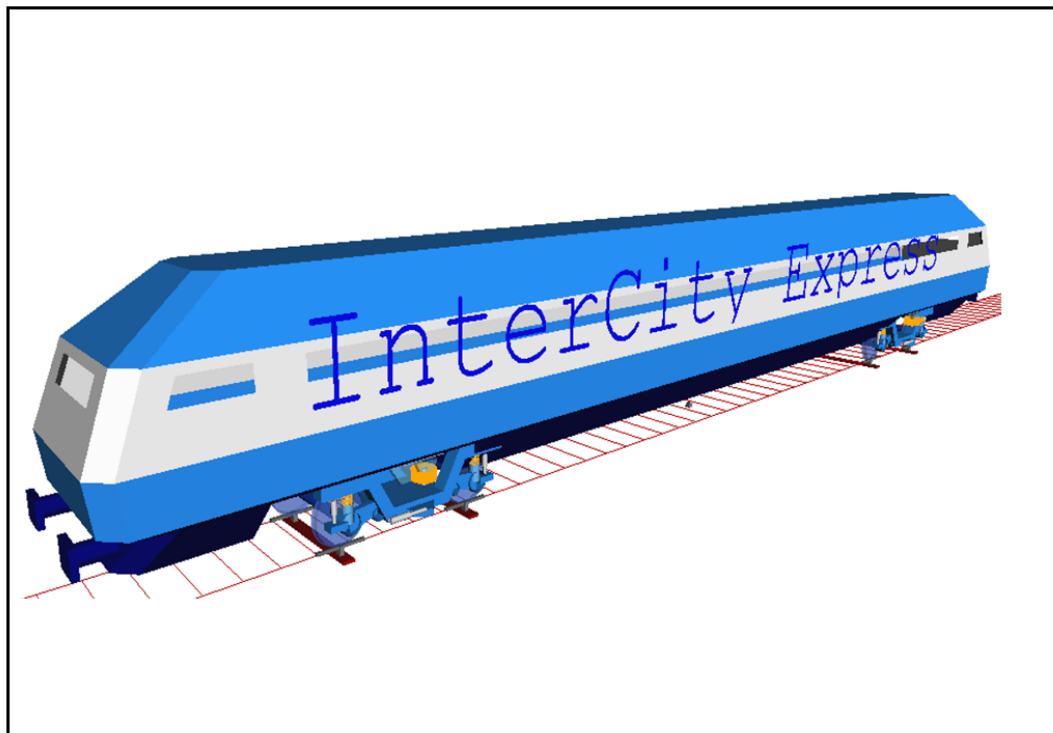
Figure 73: Overview of the basic vehicle model 1, Intercity Passenger Train
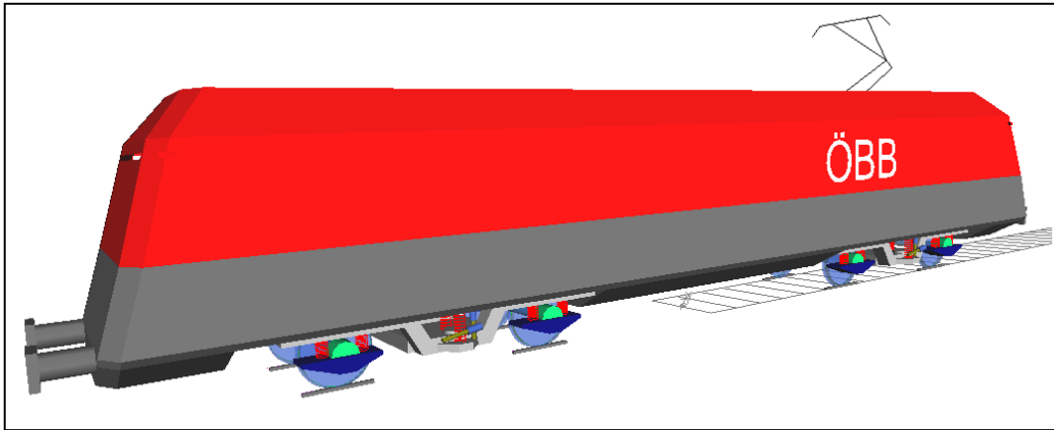
Figure 74: Overview of the basic vehicle model 2, Locomotive

In this work, the whole vehicle-track dynamic analysis is based on these two vehicle types to study the influence of lateral track stiffness on the vehicle dynamic behaviour.

6.4.1 Linear critical speed of the vehicle

The determination of the linear critical speed is dependent on the properties of the vehicle model including the rail wheel contact geometry. The rail/wheel contact linearization plays an essential role on the results. It is the first check to ensure the correctness of the vehicle model [43]. The theoretical background for the numerical solution is described in [3] and the corresponding results considering the rail head lateral displacement concerned in this study are described in section 7.4.

6.4.2 Non-linear critical speed of the vehicle

The investigation of the non-linear critical speed is the investigation of vehicle running stability because it describes the decay behaviour of the running vehicle under the track excitations. Figure 75 shows the theoretical background described in [44].
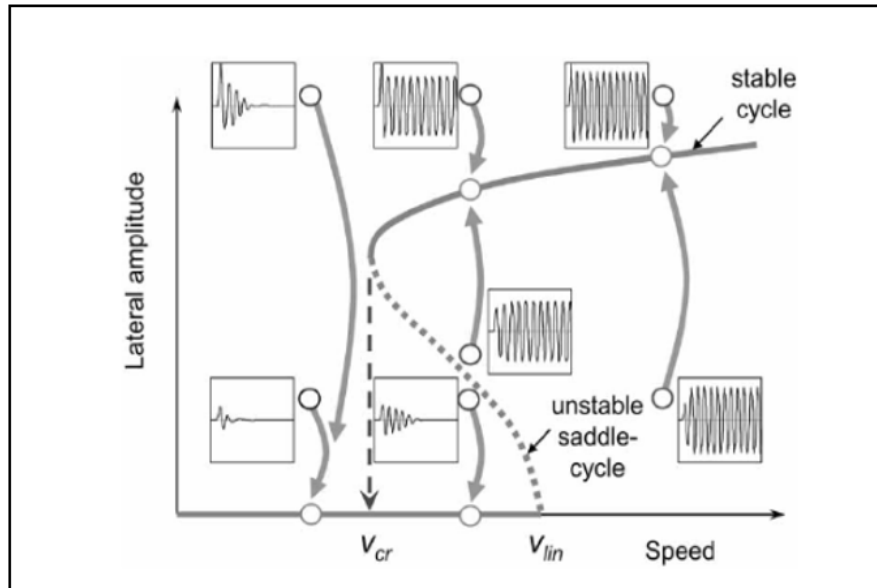
Figure 75: Bifurcation diagram as a result of the simulations of wheelset behaviour after excitation [44]

Figure 76 shows the calculated non-linear critical speed of the investigated vehicle models running on a rigid track superstructure (rail head cannot move) used as a reference for the case studies on moving rail heads under the dynamic wheel/rail contact force. It must be noted that the vehicle linear critical speed is normally higher than the non-linear critical speed. According to the standard EN 14363 [28], the designed non-linear critical speed should be at least 10% higher than the maximal service speed.
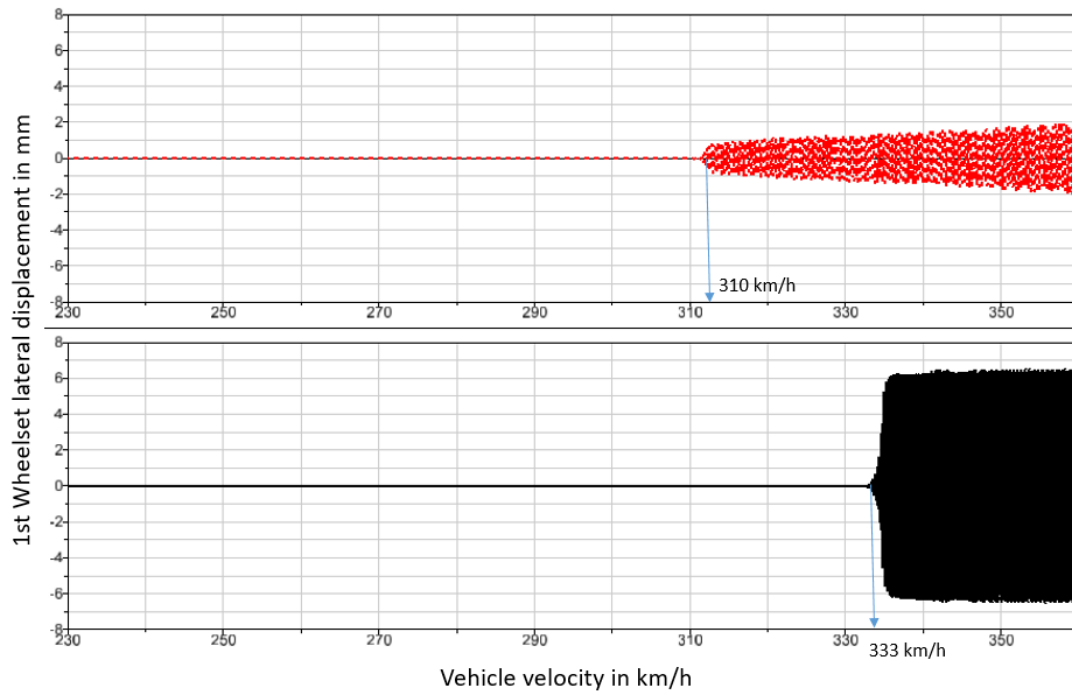
Figure 76: Nonlinear critical speed of vehicle intercity passenger train and locomotive 1116 running on a rigid track

6.4.3 Vehicle derailment analysis

The vehicle derailment analysis gives proof of the correctness of the parameters set for the vehicle model.

The twisted track method according to EN DIN 14363 [28] and ORE B 55 [47] is used for the two different vehicle models.

The criteria are:

- Safety against derailment (Y/Q) limit according to the Nadal formula

- Vehicle speed must be lower than 10 km/h

- Curve radius is 150 m

Figure 77 shows the calculated derailment coefficient of the both vehicle models.
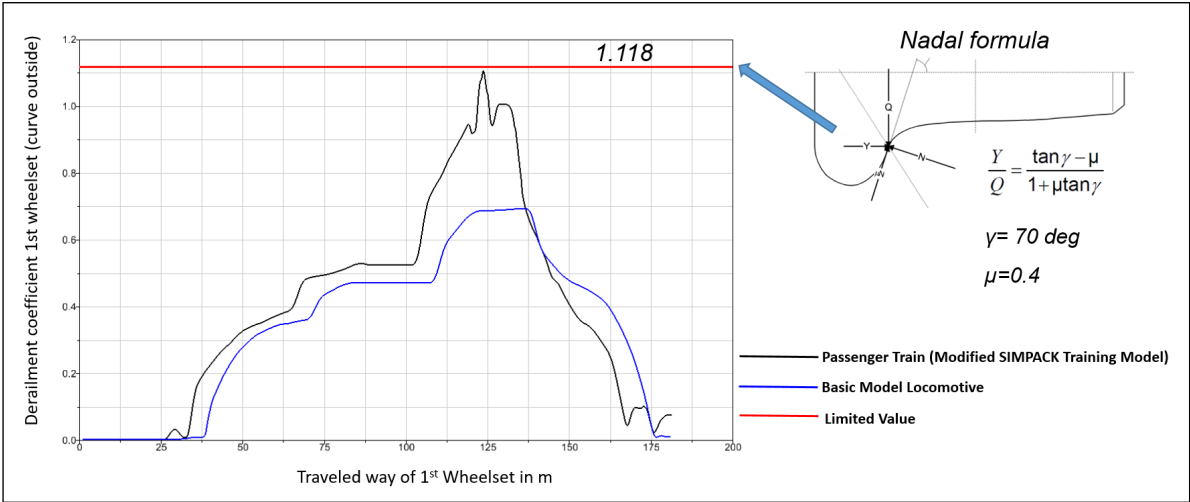
Figure 77: Derailment analysis of both vehicle models

It is found that the derailment coefficient of both vehicles is lower than the limit value calculated according to Nadal formula. It proves that the parameters applied to both vehicles are fundamentally correct and can be used for further numerical analysis.

6.5 Creation of wheel-rail contact on the fastening system model within MBS environment

The key point of the integration of the superstructure model and the vehicle model is to create the correct wheel-rail contact between both systems (see Figure 78). The in ANSYS created and validated model is converted into the MBS SIMPACK environment. The wheel-rail contact is built based on the newly developed fastening system model using standard wheel profile S1002. The validation is based on the comparison of the equivalent conicity determined by the new method and by the SIMPACK standard model, see Figure 79.
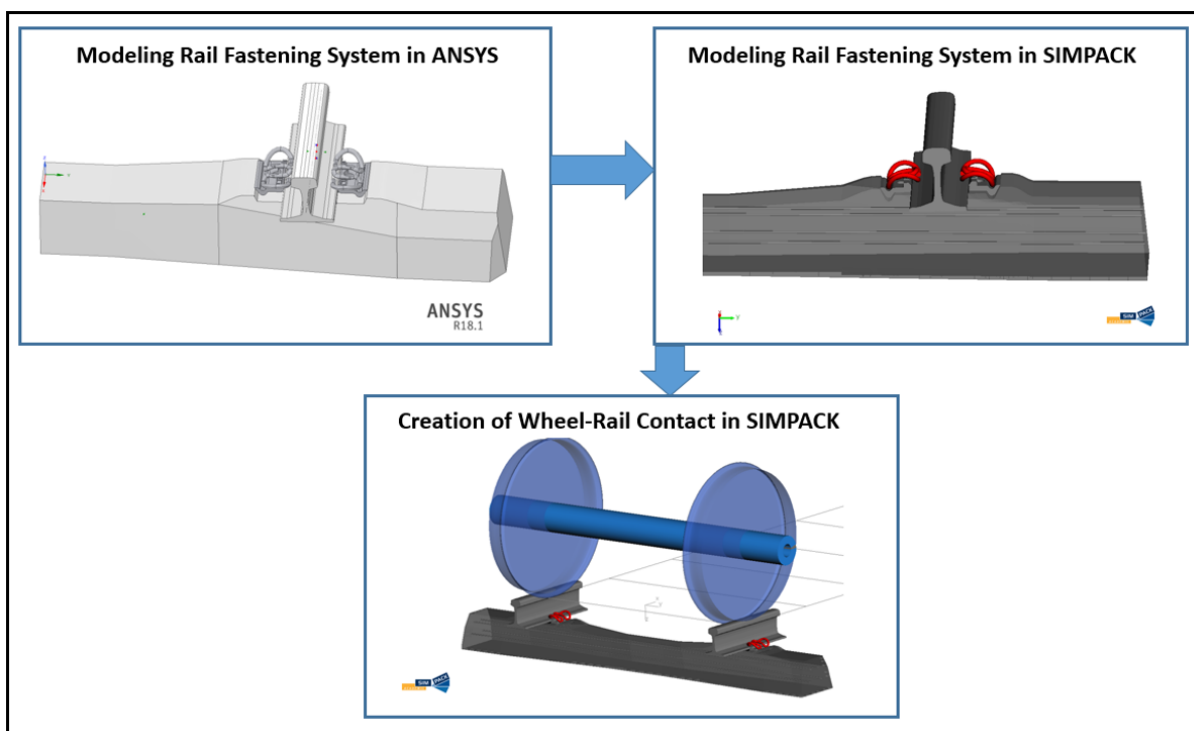
Figure 78: Workflow of integration of rail fastening system model into the wheel-rail contact system

The developed model has the functionality to consider the rail head displacement and it can be used to investigate the track-vehicle lateral dynamics based on lateral superstructure stiffness. Both models have the same equivalent conicity of 0.16177.
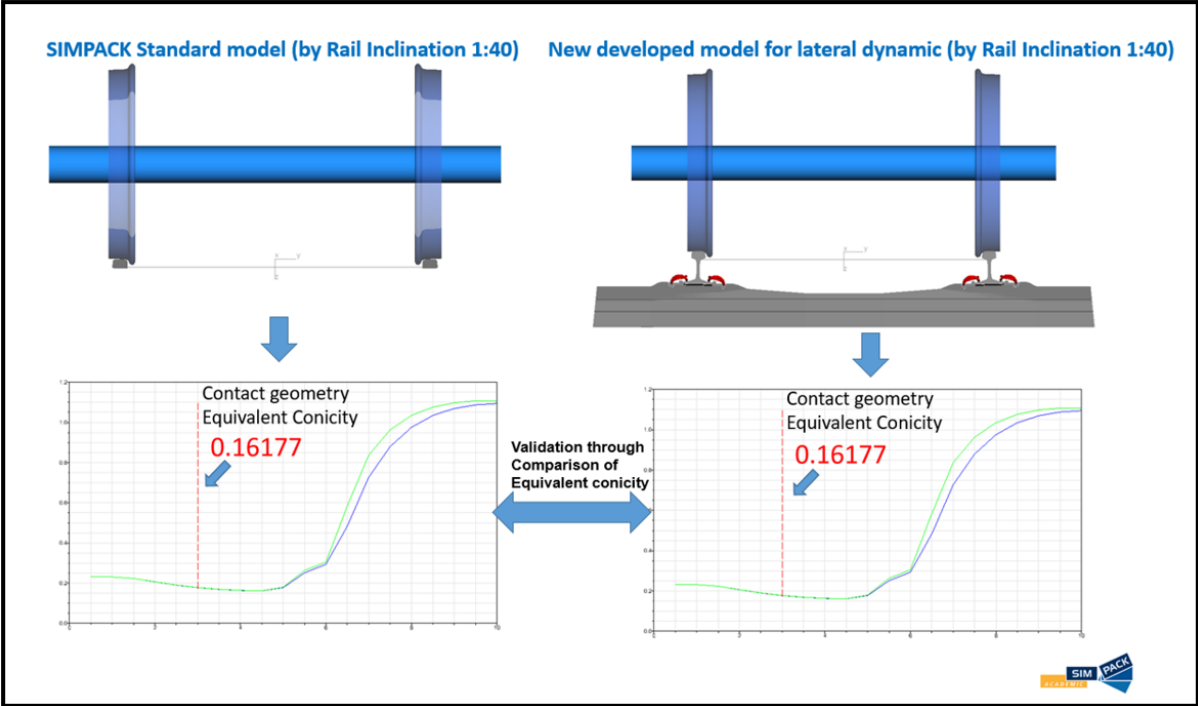
Figure 79: Examination of the correctness of newly developed model through comparison of equivalent conicity

6.6 The linking of the vehicle running model and the dynamic superstructure model

The whole modelling chain is divided in the vehicle running model and the dynamic superstructure model see Figure 80.

The vehicle running behaviour model calculates the dynamic wheel/rail contact forces and the dynamic changing of the contact points, which are used as the input for the dynamic superstructure model. The corresponding displacements, velocities, accelerations, strains and stresses on the superstructure components such as tension clamp can be calculated.

Figure 80: Overview of modelling chain: vehicle running model and superstructure dynamic model

For the modelling of vehicle running behaviour, the fastening system components such as tension clamp and angle guide plate are simplified using the corresponding non-linear and linear springs, in order to speed up the calculation time for the track/vehicle model which has many elements and degrees of freedoms inside. The real rail profile as a flexible body is used to represent the elastic properties of the rail as realistically as possible.

7. Sensitivity analysis and simulation evaluation

The configurations of rail fastening components are motivated by the intended sensitivity analysis and not with regard to the application in specific track sections.

7.1 Virtual laboratory testing of the fastening system

7.1.1 Virtual laboratory test of fastening system according to the predefined load cases in EN DIN 13481-2

The application of the test load on the rail head for rail fastening test for one support point is shown in Figure 81 according to the standard DIN EN 13481-2 [1].
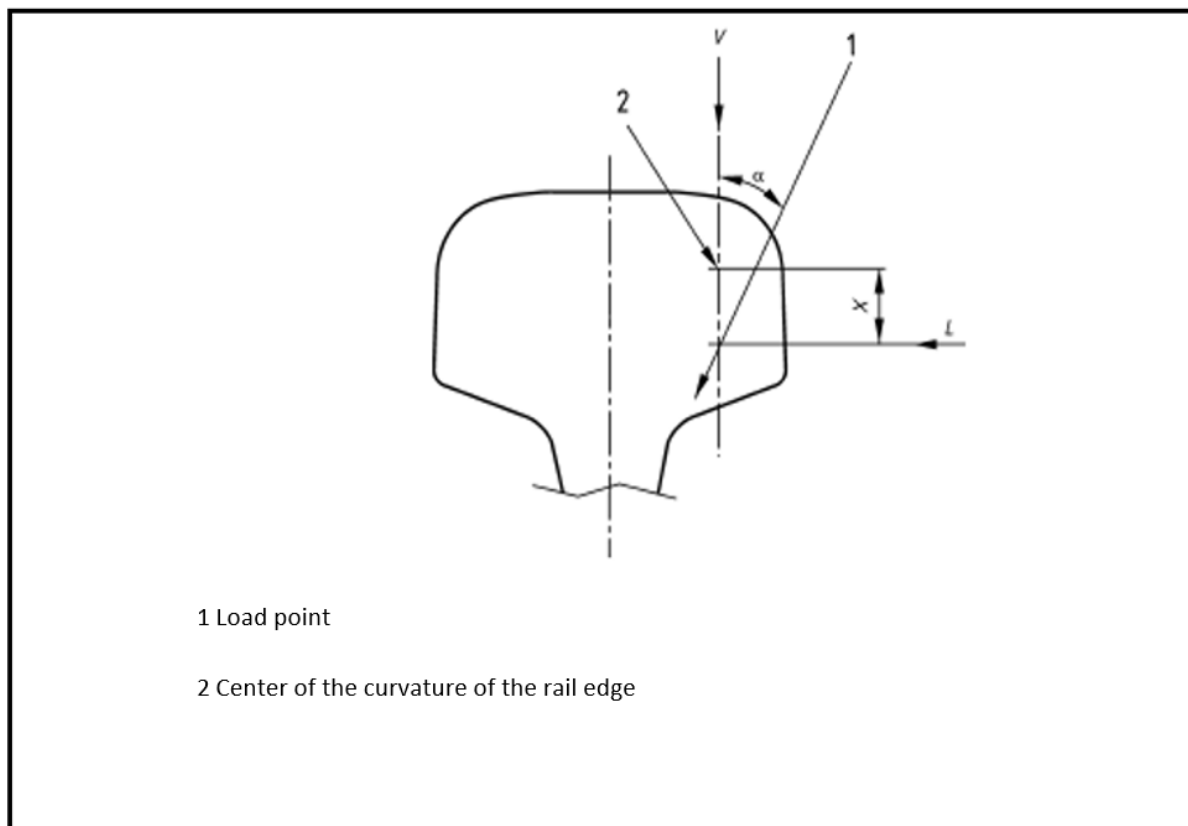
Figure 81: Definition of load attack according to [1]

Table 13 gives the test conditions for different categories; condition applied for virtual test is marked red.

Table 13: Application of force and situation of load attack according to DIN EN 13481-2 [1]

Category	α Grad (°)	X mm	$P_v/\cos\alpha$ kN[a, b]	
			$50 \leq k_{LFA} < 200$ MN/m[c, d]	$k_{LFA} \geq 200$ MN/m[c]
A	38,6	25[e]	55	55
B	38,6	25[e]	62	65
C	33	15[e]	75	83
D	26	15[e]	70	76
E	40	75[e]	100	108

Figure 82 shows the virtual test according to category C for the Skl 14 system with rail pad type Zw 700.
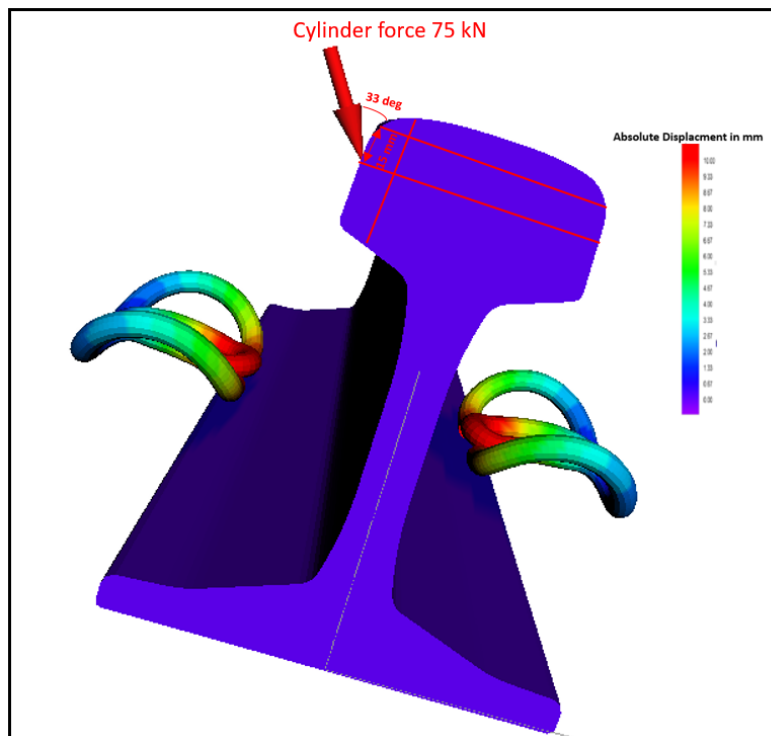
Figure 82: Lab test scenario according to DIN EN 14381-2, Category C

Table 14 summarizes the virtual testing railhead displacements using different rail pads and tension clamps according to categories C, D and E.

Table 14: Railhead displacement according to test categories using virtual laboratory test in mm

	Rail head lateral displacement (mm)		
	Zw 687	**Zw 700**	**Zw 1000**
Load cases	**Lab-Test scenario**	**Lab-Test scenario**	**Lab-Test scenario**
Cat C Skl 14	1.7	1.8	
Cat C Skl 21	1.7	1.8	2.3
Cat C Skl 28	1.7	1.7	2.1
Cat D Skl 14	1.2	1.2	
Cat D Skl 21	1.2	1.2	1.5
Cat D Skl 28	1.2	1.2	1.4
Cat E Skl 14	1.9		
Cat E Skl 21	1.9	2.2	
Cat E Skl 28	1.9	2.0	

The Institute of Road, Railway and Airfield Construction of TU Munich performed many rail fastening tests according to the standard DIN EN 13481. The lateral rail head displacements calculated by the numerical tool developed in this study are within the real range of real laboratory tests.

There is a rule defined in the standard if the test specimen of a fastening system passes the test scenario E, then, the test specimen should also pass by C and D. If the test scenario C passes, the test should also pass by D. That means the load cases are sequenced from the highest load (critical) to the lowest load in E> C >D. The data listed in Table 13 shows the same trend. Group E has the larger rail head displacement than the group of C and D. The group with the softest rail pad Zw 1000 has larger rail head displacements than the group with hardest rail pad Zw 687. The tension clamp with higher preload such as Skl 28 (28 kN) has a significant effect on the resistance of the rail head lateral displacement on the medium stiff (Zw 700) and the softest rail pad (Zw 1000). The effect is not recognizable with the hardest rail pad Zw 687. With Skl 21 (preload of 20 kN) the effect is only significantly noticeable with the softest rail pad Zw 1000.

Table 15 summarizes the virtual testing rail foot displacements using different rail pads and tension clamps according to categories C, D and E.

It is found that the trend of the rail foot displacements follows the rail head displacements

Table 15: Rail foot displacement according to test categories using virtual laboratory test in mm

	Rail foot lateral displacement (mm)		
	Zw 687	**Zw 700**	**Zw 1000**
Load cases	**Lab-Test scenario**	**Lab-Test scenario**	**Lab-Test scenario**
Cat C Skl 14	0.58	0.51	
Cat C Skl 21	0.58	0.51	0.5
Cat C Skl 28	0.58	0.51	0.51
Cat D Skl 14	0.42	0.38	
Cat D Skl 21	0.42	0.38	0.39
Cat D Skl 28	0.42	0.38	0.39
Cat E Skl 14	0.93		
Cat E Skl 21	0.93	0.84	
Cat E Skl 28	0.93	0.84	

7.1.2 Comparison the rail lateral displacement between lab test scenario and the track scenario

Determination of the critical scenario by train passing defined in DIN EN 13481 using MBS-Simulation.

Figure 83 shows the lab test scenario (left) using single rail seat and the track scenario (right) using long rail section (see chapter 5.7).
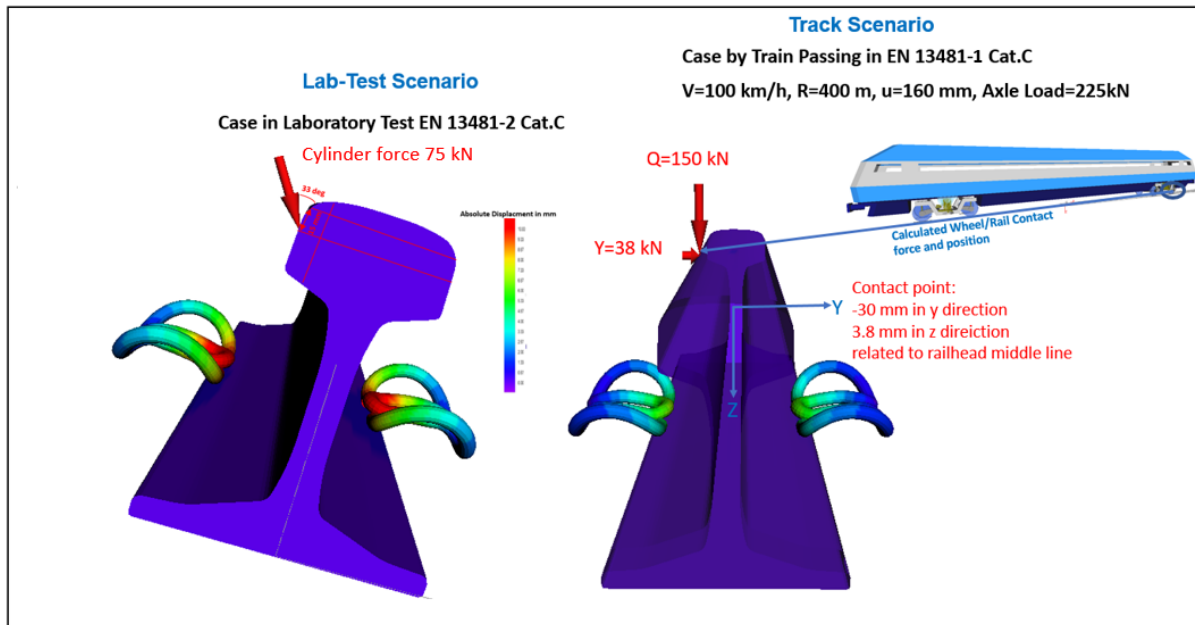
Figure 83: Illustration of comparison of the laboratory test scenario and the scenario from wheel/rail contact using virtual laboratory test

Typical cases defined in DIN EN 13481-1

Categories in DIN EN 13481-1 [48] are defined as followed:

Category C: the fastening system for the rail with a typical axle load of 225 kN, a typical curve radius of 400 m a typical maximum speed of 250 km/h, and a typical rail profile of 60E1 moreover the typical sleeper or support point spacing of 600 mm.

Category D: the fastening system for rail line with big curve radius, most often be used for high speed and the typical axle load of 180 kN, a typical curve radius of 800 m and a typical rail profile of 60E1, the typical sleeper or support point spacing of 600 mm and every typical maximum speed.

Category E: the fastening system for rail line with mixed traffic, on which the heavy trains run. With a typical axle load of 300 kN, a typical curve radius of 150 m, a typical max travelling speed of 200 km/h, a typical rail profile of 60E1 and the typical sleeper or support point spacing of 600 mm.

Cant U and cant equilibrium are calculated [45],

$U = 11.8\ V^2/R - 153 * a_q$ [mm]

With

U: rail cant in mm

87

V: vehicle speed in km/h

R: Curve radius in m

a_q: lateral acceleration in m/s^2

The parameters of U= 160 mm and a_q =0 are used to perform the calculation, the corresponding vehicle velocities and radius can be summarized in the following table according to the above-mentioned specification in EN DIN 13481-1 [48]. The calculation is performed along a track alignment designed with straight section – transition (linear ramp) – radius – transition – straight.

Table 16: Scenarios for simulation

	Speed V (km/h)	Radius R (m)	Cant u (mm)	Axle load (kN)
Category C	100	400	160	225
Category C	250	2600	160	225
Category D	140	800	160	180
Category E	60	150	160	300
Category E	200	1650	160	300

Since two scenarios are defined in category C and E in EN DIN 13481-1 [48], the following calculations aim to find the maximal lateral wheel force. The Figures below (Figure 84 to Figure 86) summarize the MBS simulation results for using fastening system Skl 14 + Zw 687 as an example.
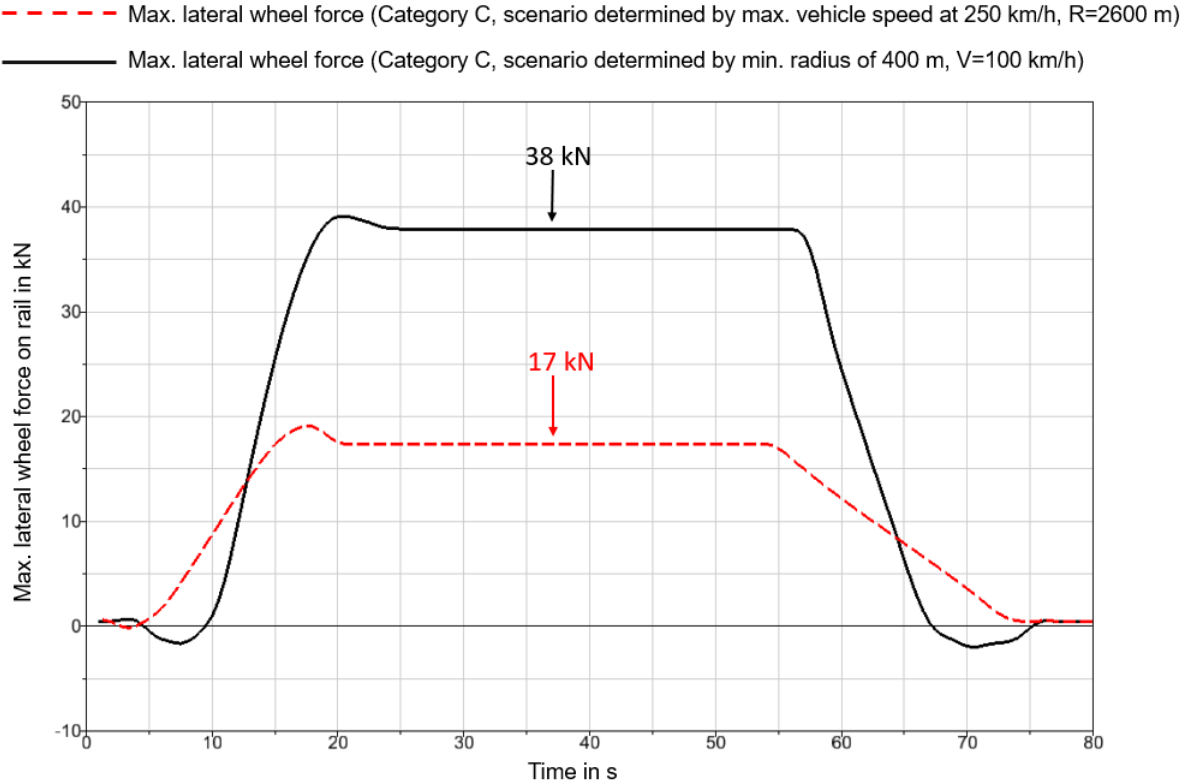
Figure 84: Comparison of lateral wheel force of track scenarios Cat C
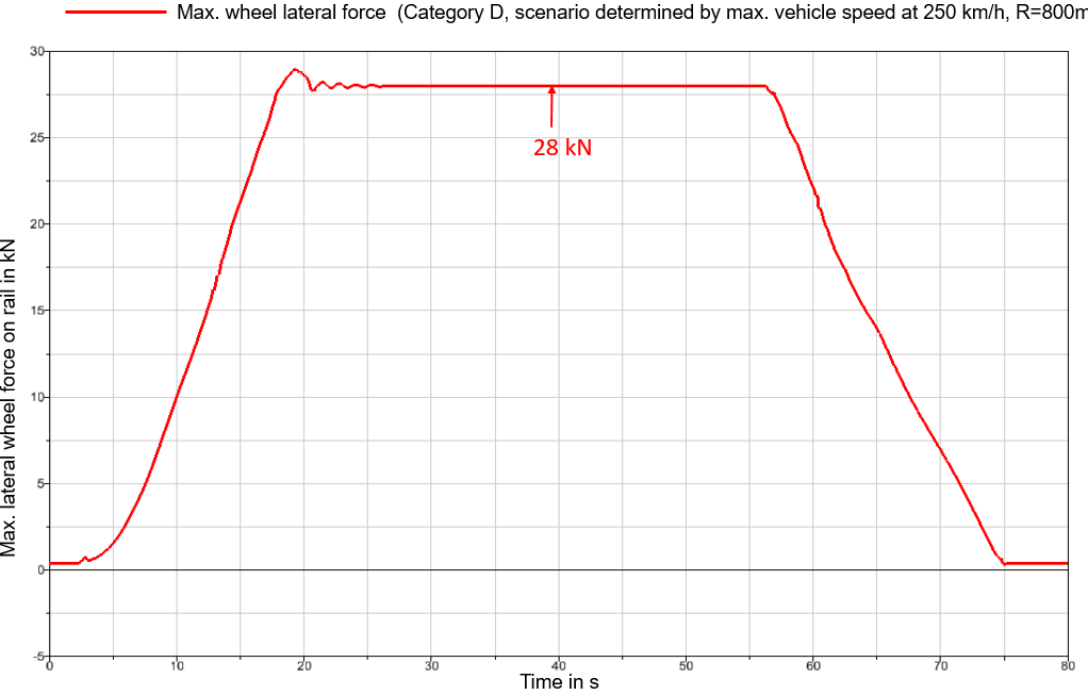
Figure 85: Lateral wheel force of vehicle running scenarios Cat D
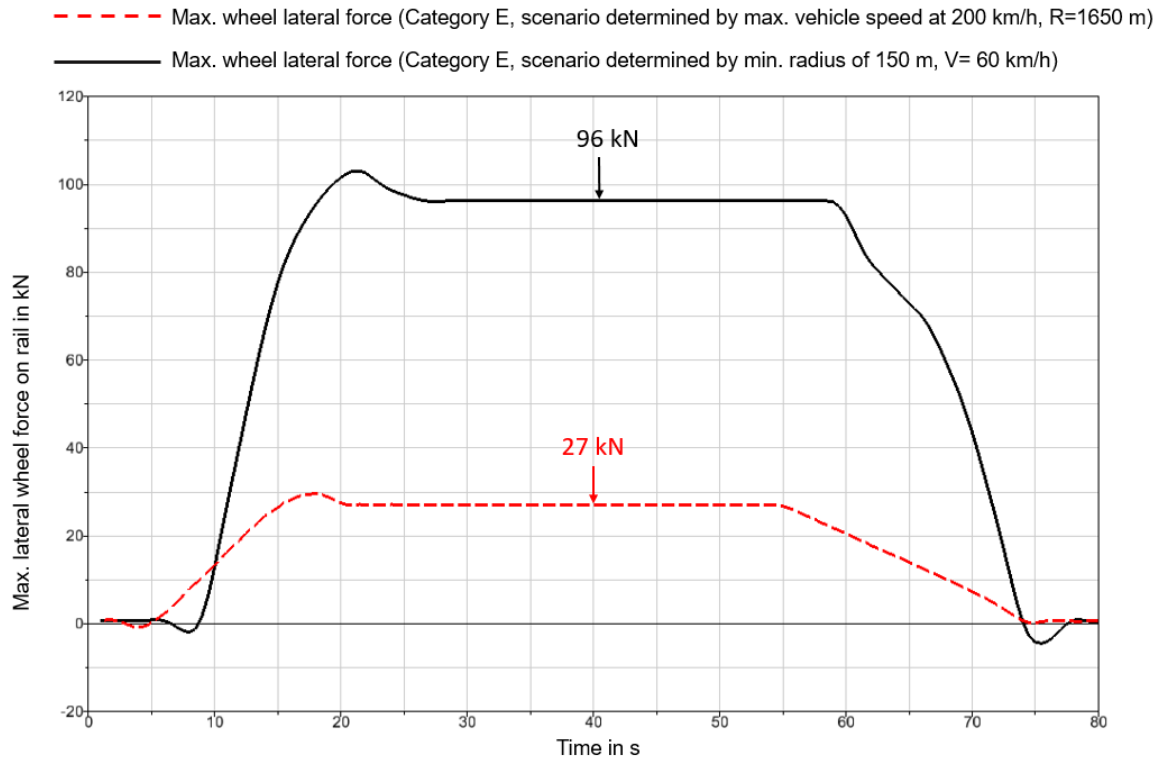
Figure 86: Lateral wheel force of track scenarios Cat E

Based on the simulation results it can be concluded that the scenarios defined by typical minimum curve radius, recommended in the standard DIN EN 13481-1 [48] (typical cases), give the critical scenarios. Table 17 lists the critical scenarios for the application of the simulation for the further investigations.

Table 17: Test scenarios for the application of the simulation performances

	Speed V (km/h)	Radius R (m)	Cant u (mm)	Axle load (kN)
Category C	100	400	160	225
Category D	140	800	160	180
Category E	60	150	160	300

The following table summarizes the calculated wheel/rail contact forces L, V and their contact positions along the radius not affected by transition section (see Table 18).

Table 18: Calculated wheel-rail contact forces L, V and their contact positions from MBS model

Category	L in kN	V in kN	Position in Y mm	Position in Z mm
C	38	150	-30	3.8
D	28	122	-17	0.7
E	96	221	-32	5.6

The negative Y value means direction rail inside related to the rail head middle line. Positive Z value means downwards related to the railhead middle line.

Table 19 summarizes the railhead lateral displacements of the lab test scenario and the track scenario from category C and E using the virtual laboratory test to compare the effect of different loads and different points of load attack.

Table 19: Comparison of rail head lateral displacement between lab test scenario and track scenario for category C and E

	Rail head lateral displacement (mm)								
	ZW687			ZW700			ZW1000		
Load cases	Lab-Test scenario	Track scenario (long rail section)	Δ mm	Lab-Test scenario	Track scenario (long rail section)	Δ mm	Lab-Test scenario	Track scenario (long rail section)	Δ mm
Cat C Skl14	1.7	0.6	1.1	1.8	0.67	1.13			
Cat C Skl21	1.7	0.6	1.1	1.8	0.66	1.14	2.3	0.73	1.57
Cat C Skl28	1.7	0.6	1.1	1.7	0.64	1.06	2.1	0.7	1.4
Cat E Skl14	1.9	1.6	0.3						
Cat E Skl21	1.9	1.6	0.3	2.2	1.8	0.4			
Cat E Skl28	1.9	1.6	0.3	2.0	1.7	0.3			

It is found that all the lateral rail displacements from track scenario are smaller than the lab test scenario.

Scenarios according to DIN EN 13481-2 for ballasted track

In the next step, the limits as defined in DIN EN 14381-2 [1] for ballasted track are applied to the track scenario and compared with the lab test scenarios. Using the same method as for the typical cases, the through MBS model calculated track scenario in L and V forces and the contact positions were listed in Table 20.

Table 20: Calculated wheel-rail contact forces L, V and their contact positions from MBS model for category C and E for ballasted track

Category	L(kN)	V(kN)	Position in y(mm)	Position in z(mm)
C	78	161	-32	6
D	44	150	-30	4
E	101	220	-33	6

Table 21 gives the results of category C and E for the limit loading scenario.

Table 21: Comparison of rail head lateral displacement between lab test scenario and track scenario for category C and E for ballasted track

Load cases	ZW687			ZW700			ZW1000		
	Lab-Test scenario	Track scenario (long rail section)	Δ mm	Lab-Test scenario	Track scenario (long rail section)	Δ(mm)	Lab-Test scenario	Track scenario (long rail section)	Δ mm
Cat C Skl14	1.7	1.3	0.4	1.8	1.5	0.3			
Cat C Skl21	1.7	1.3	0.4	1.8	1.5	0.3	2.3	1.7	0.6
Cat C Skl28	1.7	1.3	0.4	1.7	1.4	0.3	2.1	1.7	0.4
Cat E Skl14	1.9	1.7	0.2						
Cat E Skl21	1.9	1.7	0.2	2.2	1.8	0.4			
Cat E Skl28	1.9	1.7	0.2	2.0	1.8	0.2			

Based on the Table 21, it is found that the typical track scenarios defined in EN 13481-2 for ballasted track are more critical with respect to lateral rail head displacement than the limit

scenarios defined in EN 13481-1, however all the rail head lateral displacements from track scenario are smaller than the lateral railhead displacements from lab test scenario. This confirms that the requirements for performing the laboratory tests are conservatively designed (section 7.1.2, Table 21). All the railhead lateral displacements in the virtual laboratory tests following category C (DIN EN 14381-2) and using soft rail pads (e.g. Zw 1000) are below 3 mm as demonstrated by the real laboratory tests.

The tests defined in the standard represent categories not individual cases. The lowering of the point of load attack (e.g. X=15 mm for category C, D) to adopt the rail rotation comes with a particular benefit for rail fastening system equipped with soft rail pad.

7.1.3 Parameter variation of rail fastening system

Based on the developed virtual laboratory tool, parameter variations on different fastening components such as rail pad vertical stiffness, tension clamp preload and fastening system lateral stiffness (angle guide plate + rail pad assembled+ tension clamp) under load case of category C were carried out. The configurations of rail fastening components and parameters are motivated by the intended sensitivity analysis and not with regard to the application in a specific track sections.

Table 22 shows the rail head lateral displacement and the rail rotation angle under variation of tension clamp preload with constant lateral fastening system stiffness at 70 kN/mm (angle guide plate + rail pad assembled+ tension clamp) and rail pad Zw 1000 in category C.

Table 22: Rail head lateral displacement under variation of tension clamp preload with constant lateral fastening system stiffness of 70 kN/mm and Zw 1000 in category C

Tension clamp preload (kN)	Lateral railhead displacement (mm) Cat C	Rail Rotation Angle (°) Cat C
10	2.6	0.70
12	2.6	0.67
14	2.5	0.67
16	2.4	0.62
18	2.3	0.60
20	2.3	0.58
24	2.2	0.55
28	2.1	0.53
30	2.1	0.52

Table 23 shows the rail head lateral displacement under variation of lateral fastening system stiffness (angle guide plate + rail pad assembled) with constant tension clamp preload 18 kN and rail pad Zw 1000 in category C. According to the documentations [9] [12], the lateral fastening stiffness is varied in a range from 20 kN/mm to 80 kN/mm.

Table 23: Rail head lateral displacement under variation of lateral fastening system stiffness in category C

Lateral fastening stiffness (kN/mm)	Lateral railhead displacement (mm) Cat C	Rail Rotation Angle (°) Cat C
20	3.8	0.6
30	3.1	0.6
40	2.8	0.6
50	2.6	0.6
60	2.5	0.6
70	2.4	0.6

Table 24 gives results of the rail head lateral displacement under variation of vertical rail pad stiffness with constant tension clamp preload 18 kN and constant lateral fastening system stiffness of 70 kN/mm (angle guide plate + rail pad assembled+ tension clamp).

Table 24: Rail head lateral displacement under variation of vertical rail pad stiffness based on Zw 1000 in category C

Vertical Stiffness Factor based on Zw 1000	Lateral railhead displacement (mm) Cat. C	Rail Rotation Angle (°) Cat. C
0.5	2.41	0.62
1	2.4	0.6

7.2 Vehicle/track simulation according to the field measurement Redl/Zipf-Vöcklamarkt

The test scenario of the field measurement in track section Redl/Zipf-Vöcklamarkt (described in chapter 4) was reproduced using the developed vehicle/track dynamic model:

- curve radius R=799 mm (left curve related to running direction)

- designed track cant 160 mm, average actual track cant 157mm

- maximal vehicle speed 130 km/h; actual speed 120km/h

- Rail fastening systems: Skl 21+Zw 687 (with under-sleeper pad), Skl 21 + Zw 1000 (without under-sleeper pad)

- The difference in the lateral sleeper support provided by the presence/absence of under-sleeper pad had not been realised because of the identical lateral sleeper displacement behaviour as recorded during the on-site measurements.

- Locomotive 1116, wheelbase 3 m, bogie distance 9.9 m, total mass in service 86 t [12]

Figure 87: Track alignment setup in the model

The track irregularities applied in the simulation are converted by PSD ERRI Low and by PSD ERRI Low reduced by Factor 0.5. Figure 88 illustrates the results.
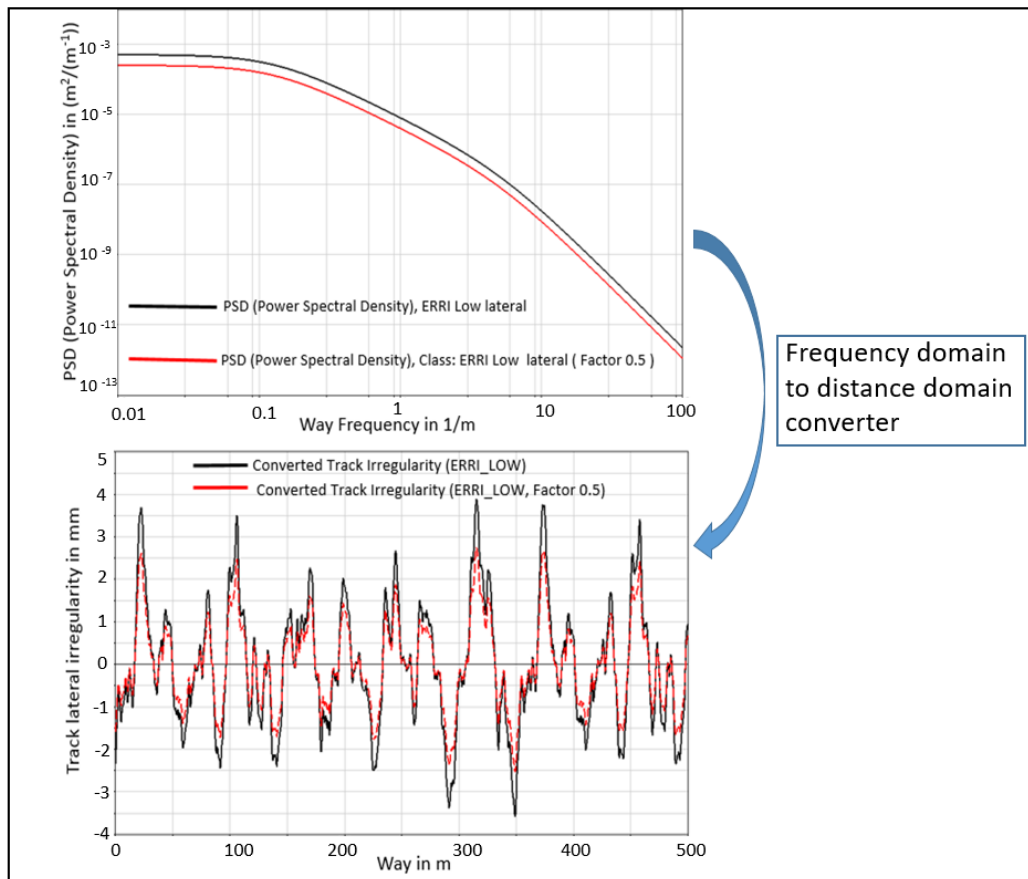
Figure 88: PSD ERRI Low, ERRI Low factor 0.5 and the corresponding converted track irregularities

Figure 89 shows the comparison of the lateral rail head displacement of the field measurement (see chapter 4.2) and the simulation in time domain measured at one sensor point. The vehicle speed is set to 120 km/h. The lateral rail head displacement of the curve outside rail during passage of 1st wheelset and 2nd wheelset of the locomotive was represented in the figure to give an example. It can be seen that the lateral rail head displacements given by measurement and simulation are identical.

Figure 89: Railhead lateral displacement in comparison of filed measurement and simulation in time domain at curve outside rail

Based on the verified model described in Figure 89, a further representation of the calculated results over a long track section (3000 m) to obtain an overview of the dynamic lateral rail head displacement along straight track section, transition curve and   radius is shown in Figure 90.

It gives the simulation results of system Skl 21 + Zw 1000 as an example, the conclusions are:

- The simulation results are consistent with the field measurements described in section 4. The peak values of the dynamic rail head lateral displacement for curve outside rail are close to 1 mm, and just as the measured results, the direction is towards the outside of the rail (see Figure 18 in chapter 4.2 and Figure 89).

- The dynamic rail head lateral displacement on the straight track section is smaller than along the curved section.

- Along radius the dynamic amplitudes along the outside rail (right) are larger than along the inside rail (left). Both rail heads contribute to gauge widening. The initial rail lateral displacement to the track inside (less than 0.1 mm, the initial section without track irregularity) of both rails along the straight section is caused by the lever arm effect of the rail inclination (1:40) under the vertical wheel force.
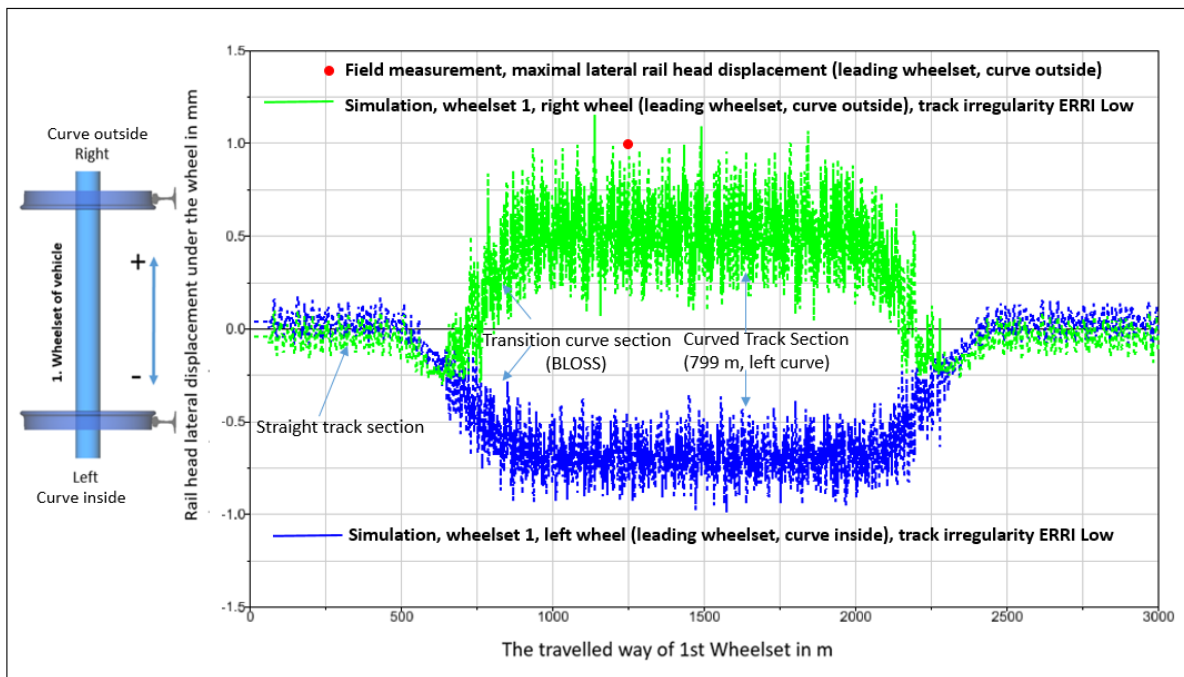
Figure 90: Railhead lateral displacement under the leading wheelset of vehicle with and without track irregularities (Skl 21+ Zw 1000)

Figure 91 illustrates the wheel/rail contact position and the contact points in view of the first wheelset of the vehicle. The definition of the coordinate system is according to the standard of rail engineering defined in [29].

It can be found, that the contact point on the right side rail is at the position of Y=-29.2 mm (rail inside to the rail center) in the lateral direction and Z=3.4 mm (downwards related to the rail middle line). The contact point at left side rail is at the position of Y=-4.3 mm (left side to the rail middle line) and Z is nearly to 0 related to the rail middle line. It is observed that the resultant lateral force at the right side wheel pushes the rail head towards to the curve outside and on the left side, the lateral force pushes the rail head towards to the curve inside. The calculated vector wheel/rail contact forces and the contact positions are reasonable and consistent with the illustrated results in Figure 91.
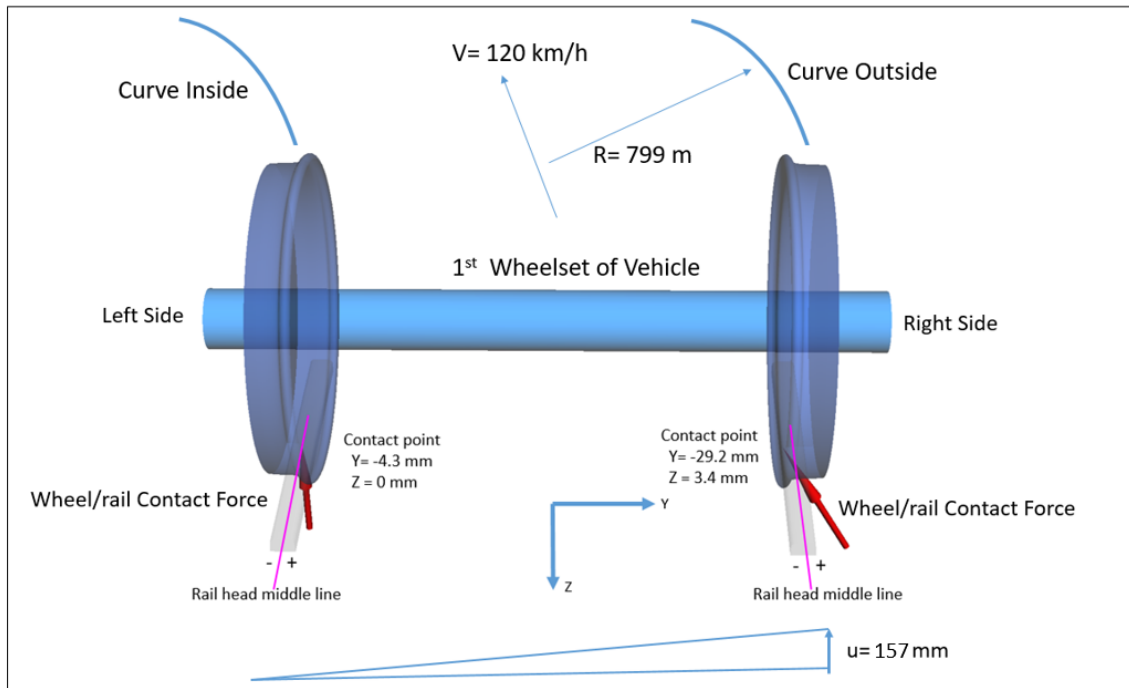
Figure 91: Scenario and coordinate system in simulation

The purpose of the numerical tool is to investigate the effect of the fastening system stiffness on the railhead displacement and on vehicle running behaviour enveloped the vehicle/track interaction.

Figure 92 illustrates the calculated results from the simulation tool. It shows the comparison between two different fastening systems Skl 21 + Zw 687 and Skl 21 + Zw 1000 under the same vehicle and track alignment conditions. The Figure shows that the combination of Skl 21 + Zw 1000 (soft system) has a higher rail head lateral displacement than Skl 21 + Zw 687 (hard system). The reason is that the hard rail pad Zw 687 can limit the rail rotation much better than the soft rail pad Zw 1000. A great advantage of this simulation tool is that the animation gives a realistic insight to the displacements and deformations.
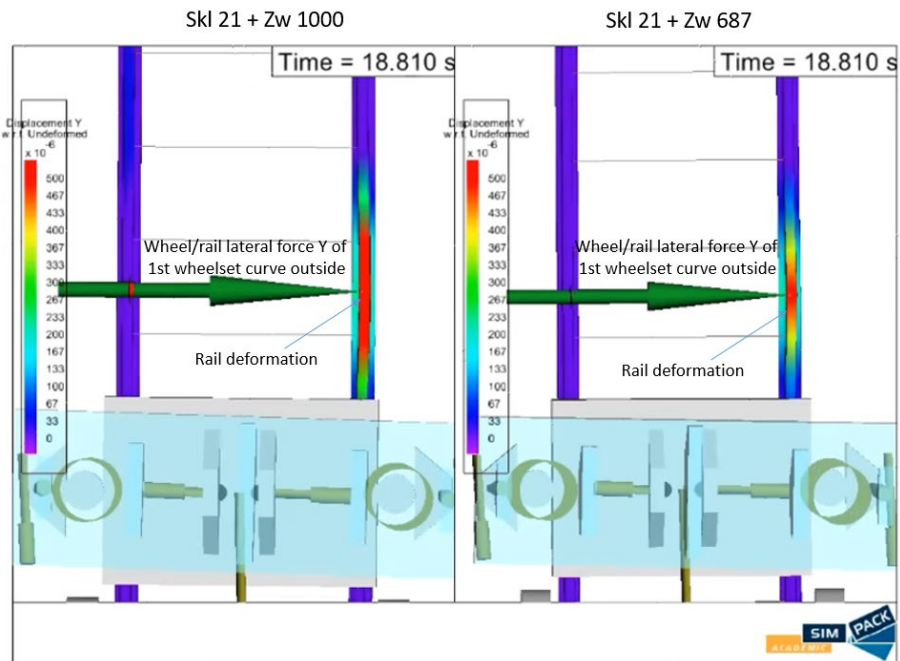
Figure 92: Illustration of the rail head displacement under the leading wheelset of vehicle using different fastening systems

Figure 93 shows the comparison of the calculated rail head lateral displacement using two different fastening systems. The lateral rail head displacement of the stiffer system (Zw 687+ Skl 21) is smaller than the soft system (Zw 1000 + Skl 21), this tendency is also consistent with the field measurement described in section 4.2.
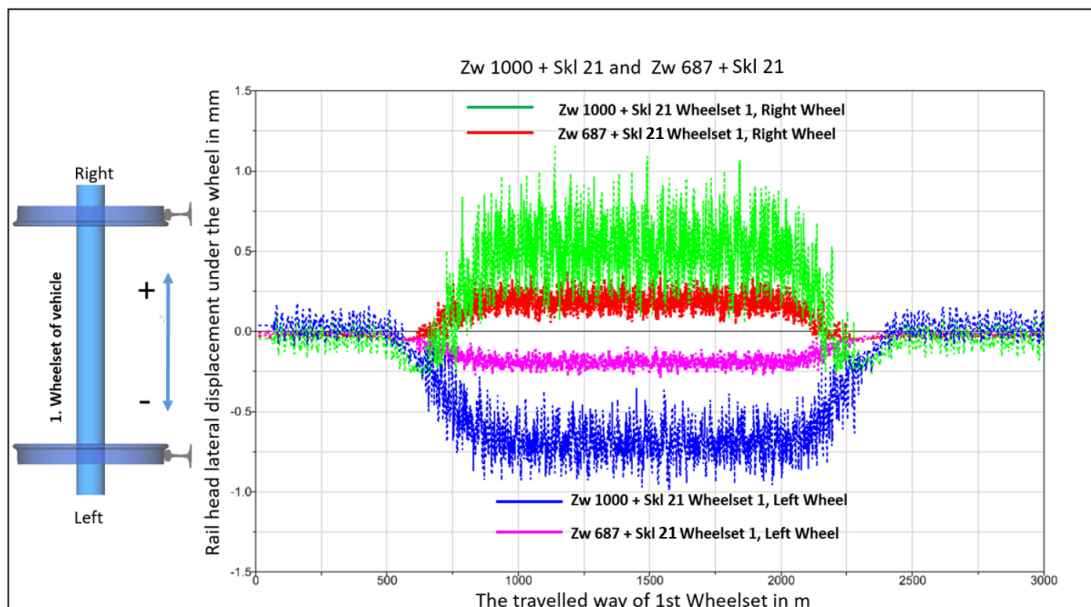
Figure 93: Rail head displacement under the leading wheelset of vehicle using different fastening system

The dynamic lateral rail head displacement is caused by the track response by the initiated sinus running behaviour of the wheelset with continuous excitation of the track irregularities.

To investigate the influence of the track irregularity on the dynamic effect, a comparison of two different track irregularities (ERRI Low and ERRI Low factor 0.5) is illustrated in Figure 94.
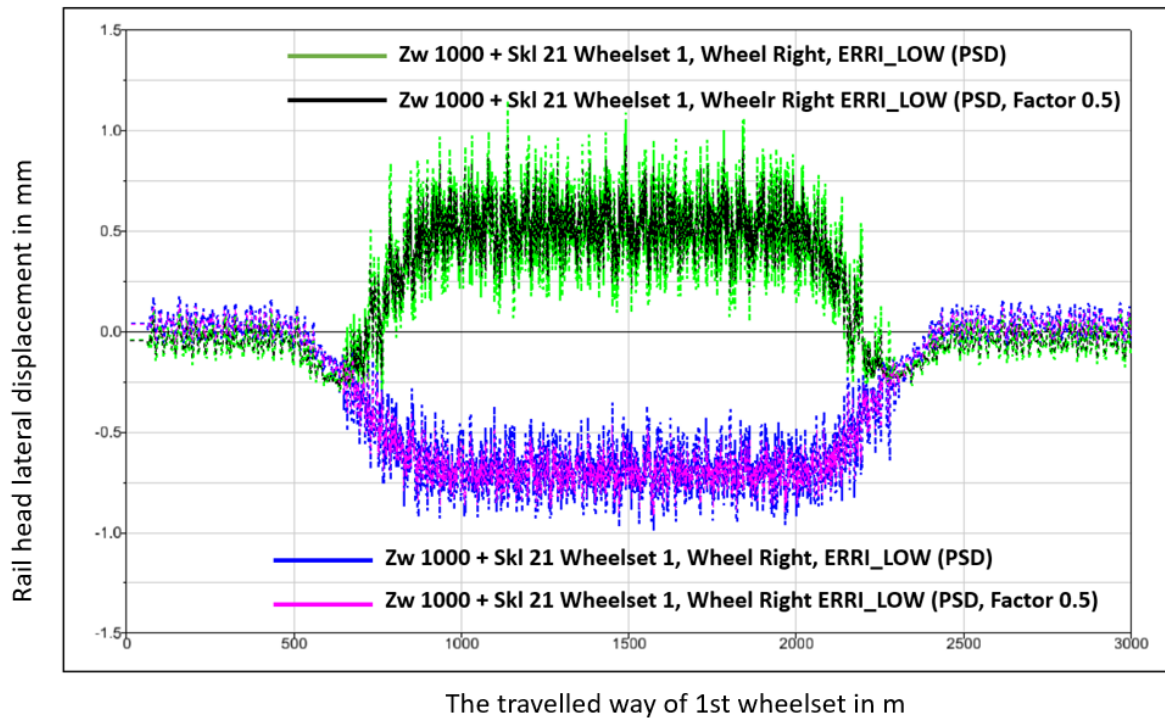
Figure 94: Rail head lateral displacement under different track irregularities

It can be seen that the dynamic rail head lateral displacement due to track irregularities PSD ERRI_Low standard is larger than that with factor 0.5, i.e. the track irregularities play a significant role in the dynamic response of superstructure. The smaller the amplitudes of the track irregularities, the lower the dynamic response of the track superstructure. Good maintenance to limit the track irregularities is also an important factor in protecting the superstructure against high dynamic wheel/rail contact loads.

Figure 95 gives the results of the measured and calculated rail head surface wear. It is found that the calculated results match the results gained from measurements. The normalised figure shows that the wear along the outer rail is much higher than along the inside rail.
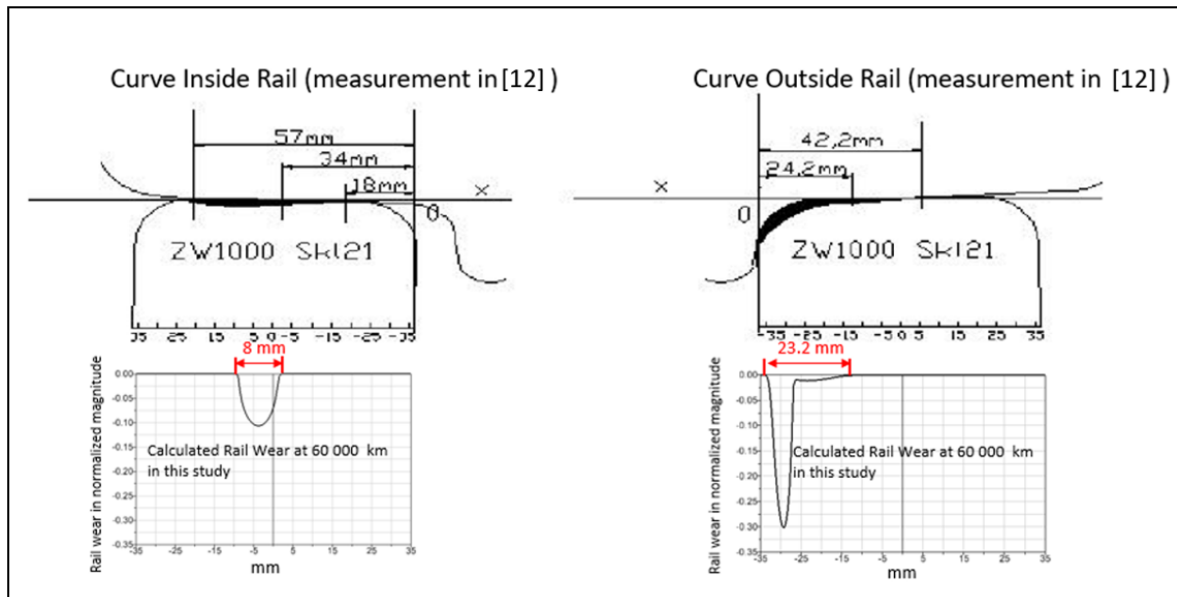
Figure 95: Comparison of the calculated and measured wear area on rail profiles

The reason of the material loss is the friction power between the wheel and rail. In SIMPACK, it is treated as wear number and calculated as $|Tx*vx|+|Ty*vy|+|Mz*\varphi z|$. Where, the Tx, Ty and Mz are the creep force and creep torque in x, y and about z directions; the vx, vy and φz are the relative creepages in x,y and about z directions [3].

Figure 96 illustrates sleeper lateral displacement under the leading wheelset with track irregularities using 40 kN/mm for sleeper lateral support stiffness. The calculated dynamic sleeper lateral displacements under leading wheelset are consistent with the field measurement close to 0.2 mm.

The travelled way of 1st wheelset in m
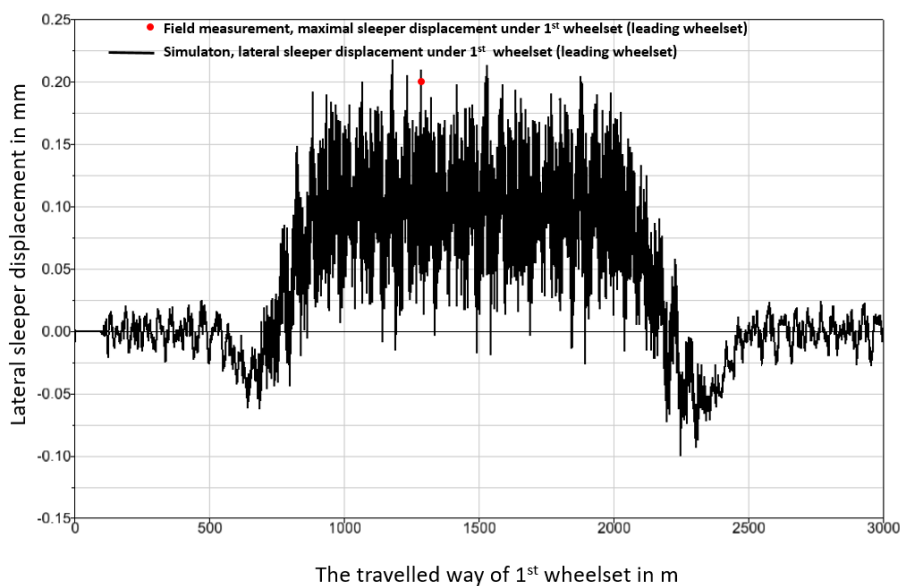
Figure 96: Lateral sleeper displacement under leading wheelset with and without track irregularities

Based on the validated model, the investigation on the four different fastening systems (Skl 14 + Zw 687, Skl 28 + Zw 700, Skl 14+ Zw 700 and Skl 21 +Zw 1000) installed on the track section Redl/Zipf-Vöcklamarkt under a converted track irregularity based on PSD ERRI Low (Figure 88) was performed and the results of the vehicle lateral axle box acceleration was summarized under Table 25.

Table 25: Lateral axle box acceleration under different fastening systems and track irregularities

Rail pad	RMS Value m/s^2
Zw 687 + Skl 14	1.31
Zw 700 + Skl 28	1.30
Zw 700 + Skl 14	1.29
Zw 1000+ Skl 21	1.19

It can be concluded, that along the 4 track sections with the 4 fastening systems, the Zw 687 + Skl 14 has the highest lateral axle box acceleration at 1.31 (RMS value) and the Zw 1000 + Skl 21 has the lowest lateral axle box acceleration at 1.19 (RMS value).

The ride comfort evaluation according to DIN EN 12299 (see chapter 2.2.4) was performed and the calculated results are summarized in the following table.

Table 26: Ride comfort under different fastening systems and track irregularities

Rail pad	Comfort ride
Zw 687 + Skl 14	0.86
Zw 700 + Skl 28	0.85
Zw 700 + Skl 14	0.85
Zw 1000 +Skl 21	0.84

For the next step, the influence of the sleeper lateral support stiffness is taken into account using the fastening system Zw 687 + Skl 21. Parameter variation on sleeper lateral support stiffness is done in range from 25 kN/mm to 40 kN/mm. Table 27 shows the corresponding influence on vehicle running behaviour.

Table 27: Influence of the sleeper lateral stiffness on the vehicle running behaviour (fastening system Zw 687 + Skl 21)

Lateral sleeper support stiffness	Lateral axle box acceleration average RMS Value	Maximal lateral sleeper displacement percentile 95
kN/mm	m/s^2	mm
25	0.98	0.35
40	1.01	0.19

The results show that the soft lateral support stiffness (25 kN/mm) is beneficial for the lateral axle box acceleration compared to the stiff one (40 kN/mm). However, the lateral displacement is also increased and the effect on the factors mentioned in chapter 5.8, such as elastic displacement W_e and elastic resistance P_e need to be considered.

7.3 Sensitivity analysis using the track scenario EN 13481-2 category E

The following process is focused on the track/vehicle dynamic effect on the narrow curve (R=150 m) area with higher axle load (350 kN) according to the track scenario defined in EN 13481-2. According to the definition in [45] and chapter 7.1.2, the calculated vehicle speed used in this analysis is 45 km/h. The track geometrical irregularity is ERRI_Low which is the same as in chapter 7.2 for simulation scenario. Different fastening systems are applied in the simulation scenario to determine the influence on the track/vehicle dynamic coupling behaviour.

Figure 97: Rail head lateral displacements under the wheel in test scenario of category E

Figure 97 gives the calculated results of rail head lateral displacements by two different fastening systems Zw 687 + Skl 14 and Zw 700 + Skl 21. Based on the results, the following conclusions can be given:

- The rail head lateral displacement of fastening system Zw 687+ Skl 14 is generally smaller compared to Zw 700+ Skl 21

- There are peaks of lateral rail head displacements at the beginning and at the end of the radius. They vary according to the individual track alignment, vehicle speed and vehicle types.

- In comparison with Figure 93 in chapter 7.2, the lateral rail head displacement in Figure 97 is much higher because of smaller curve radius and higher axle load. However, the dynamic effect caused by track irregularities is smaller than the results in Figure 93, because the vehicle velocity is 45 km/h according to the category E compared to 120 km/h as shown in Figure 93 for the Redl/Zipf-Vöcklamarkt track section.

In the next step, the vehicle travels along a track following the same track scenario of category E but equipped with a different tension clamp Skl 28 which supply a higher tension clamp preload on the middle stiff rail pad Zw 700.

Figure 98 shows the compared rail head lateral displacements.
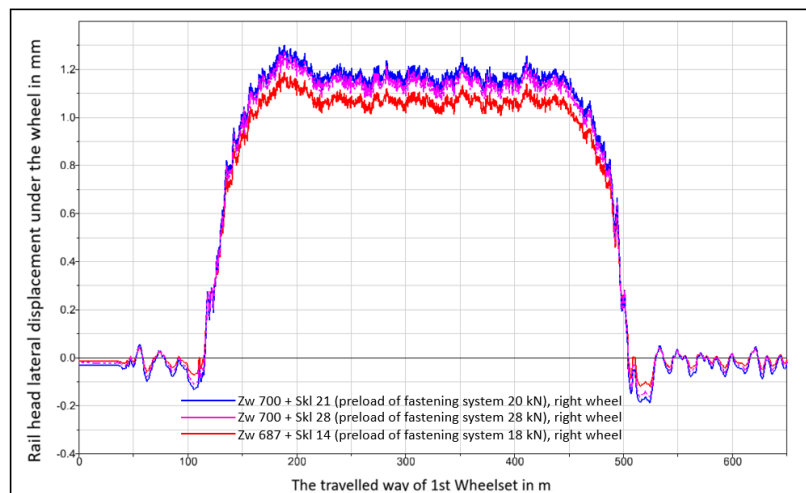
Figure 98: Comparison of lateral rail head displacements under different rail pads and tension clamp preloads

It can be found that the use of Skl 28 (preload 28 kN) helps to reduce the rail head lateral movement in comparison with Skl 21 (preload 20 kN) with the same medium-stiff rail pad Zw 700. However, compared to the stiff rail pad (Zw 687) with a lower tension clamp preload Skl 14 (preload 18 kN), the rail head lateral displacement is still larger when using Skl 28 + Zw 700.

For the case of tight curve and heavy axle load, the usage of the stiff rail pad 687 (e.g. Zw 687 instead of Zw 700) is one of the best way to control the rail head lateral motion, but the vertical and lateral load distribution effect will become worse caused by the stiff support stiffness of the Zw 687. A favourable solution is using a middle stiff rail pad such as Zw 700 with a higher tension clamp preload such as Skl 28 in a narrow curve including the transition area, as done by ÖBB in practise.

According to the documentation [9] and the description in 5.4, when the lateral force from wheel/rail contact is large, the main lateral fastening stiffness is contributed by the angle guide plate. Unlike the elastic component rail pad, the angle guide plate works only in the lateral direction. In order to research the relationship between the angle guide stiffness and the dynamic reaction force on it, it is assumed that the angle guide plate contribute the whole lateral stiffness of the fastening system and the effect of other parts (tension clamp, friction between rail and rail pad) in lateral direction are neglected. The applied tension clamp and rail pad for the following research are Skl 28 with Zw 700 which has the same track scenario as defined in DIN EN 13481-2 category E.

Figure 99 gives an overview of the reaction force of the angle guide plate under different stiffness and the rail head lateral displacement under the 1st wheelset, which is located on the curve outside rail.
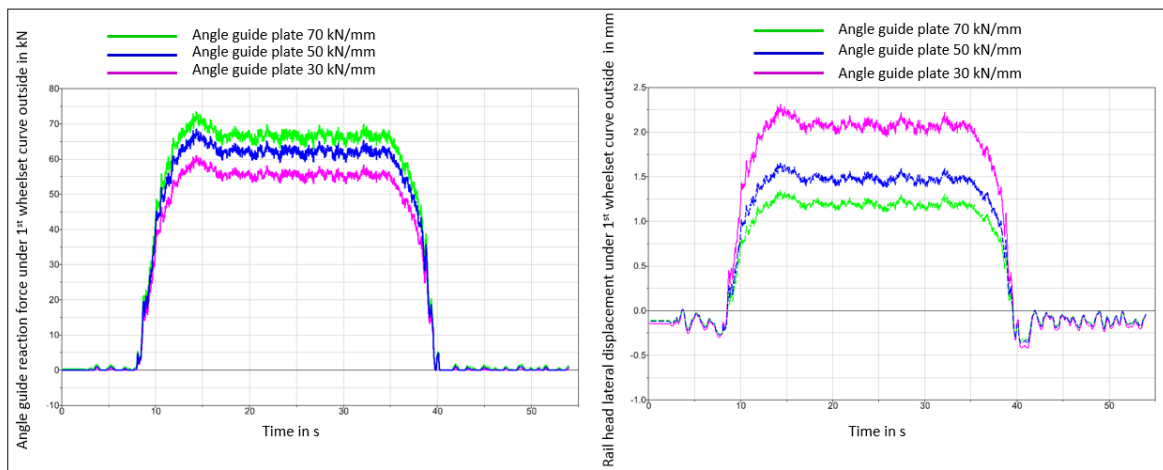
Figure 99: Reaction forces and rail head displacements under different angle guide stiffness

It can be concluded that the angle guide plate plays an essential role in the lateral movement of the rail. The soft angle guide plate leads to a larger lateral rail head displacement (Picture right in Figure 99), but lower reaction force compared to the stiff angle guide plate (Picture left in Figure 99). A higher lateral stiffness of the angle guide plate is reducing the lateral load distribution by the rail, but limiting the lateral rail movement. The dynamic forces caused by track irregularities are smaller using soft angle guide plates. A value of 50 kN/mm is used by practical experience of ÖBB according to [10].

7.4 Effect of lateral track stiffness along straight track

In this section, the influence of the superstructure lateral stiffness on the vehicle running behavior on a straight track is investigated.

Linear critical speed

Table 28 gives a summary of the relationship between gauge and linear critical speed calculated by SIMPACK. The position of the rail is given before the simulation starts and is not changed. The dynamic effect under consideration of the lateral rail head displacement and the impact of dynamic force cannot be considered.

Table 28: Relationship between linear critical speed and the rail gauge changing by rail inclination of 1:40

Gauge	Linear critical speed
1433 mm	360 km/h
1434 mm	370 km/h
1435 mm	380 km/h
1436 mm	400 km/h

As the gauge increases, the linear critical speed is also increasing because of decreasing the equivalent conicity.

Non-linear critical speed

The method according to [44] for determination of vehicle non-linear critical speed was used to carry out the following investigations.

Table 29 lists the effect on the critical speed by using different tension clamp preloads on a rail pad Zw 1000 and an initial lateral fastening stiffness at 70 kN/mm.

Table 29: Influence of different tension clamp preloads under rail pad Zw 1000 on vehicle critical speed

Tension clamp preload	Non-linear critical Speed in km/h
10 kN	282
18 kN	298
30 kN	323
32 kN	324

It can be found that the increase in preload (more constraint on the rail rotation) is beneficial for increasing the critical speed. The critical speed is 282 km/h with a tension clamp preload of 10 kN and increases to 324 km/h when the tension clamp preload is 32 kN.

Based on the investigations in chapter 5.4.4, the lateral stiffness on the straight section without contact between rail foot and angle guide plate can be small. The parameter variation in this study to investigate the influence of different lateral fastening system stiffness on the critical speed is extended to a minimum lateral stiffness of 5 kN/mm and no abnormal vehicle running

behaviour occurs. A maximal non-linear critical speed (optimum) can be found by lateral stiffness of fastening system (angle guide plate + assembled rail pad + tension clamp) of 30 kN/mm using Zw 687 and of 40 kN/mm using Zw 1000 (see Table 30).

Table 30: Influence of different lateral fastening stiffness under rail pad Zw 687 and Zw 1000 on vehicle critical speed

Lateral fastening system stiffness kN/mm	Non-linear critical speed Zw 687 km/h	Non-linear critical speed Zw 1000 km/h
5	286	290
10	287	292
30	302	308
40	276	317
50	276	314
70	275	298
80	275	285

8. Developed simulation tools and findings of the research

A universal numerical modelling and simulation chain was developed to investigate the influence of the lateral superstructure stiffness on the vehicle running behavior and on the dynamic response of the track. Its input data and validation were obtained from the laboratory tests, the field measurements performed in this study and from the experiments previously conducted and described in the literature [12].

One of the developed simulation tools, called the **virtual fastening system test**, is linking the laboratory test using a single fastening system loaded by a single contact force with the real track scenario. Comparative simulations can be conducted with respect to the rail head lateral displacement because of lateral rail movement and rail rotation. It calculates the displacements, forces and stresses of the superstructure components such as rail and tension clamps. All investigations had been performed on W-fastening systems for rail profile 60 using the defined parameters as well as the theoretical (not "as built") parameter variations in the sensitivity analysis.

1) Functionality of the numerical tool for design optimization:

Using the complete 3D modelling method of tension clamp and angle guide plate developed in this study in a CAD-FEM-MBS co-simulation system, geometric design optimization under static and dynamic load can be carried out.

For the tension clamp:

The tension clamp preload can be calculated according to the different geometric design of the tension clamp (see chapter 5.6). It can help to design a new product, e.g. to achieve a higher preload with a lower middle bend displacement (elastic and plastic deformation) to avoid damage of the tension clamp.

For the angle guide plate:

The reinforcement near the screw hole is proposed to avoid a high stress concentration and to avoid lateral direct shear loading on the screw spike duo to large deformation of the angle guide plate under extreme load cases. If possible, the lateral load should be transferred via the angle guide pate into the sleeper and the shear load on the screw spike should be avoided (see chapter 5.4.3).

2) Lateral stiffness of the rail fastening system:

Under the given assumptions, a non-linear diagram of the lateral resistance vs rail movement was developed and an evaluation method of the lateral stiffness of the rail fastening system under different conditions (with and without contact between rail foot and angle guide plate) is presented.

An approach to use a simplified linear stiffness for the numerical modelling according to [9] [12] [19] [44] [46] was investigated and used in this study as input for the parameter variation of the numerical calculation.

3) Standard fastener component set-up:

The rail head lateral displacements in the laboratory test scenarios following categories C, D and E as defined in the standard DIN EN 13481-2 (ballasted track equipped with concrete sleepers) are all greater than under train passage using the track scenario. This confirms that the requirements for performing the laboratory tests are conservatively designed (see chapter 7.1.2).

The requirements defined in the European standard represent categories not individual load cases. The lowering of the point of load attack (e. g. X=15 mm for category C, D) to adopt the rail rotation comes with a particular benefit for rail fastening systems equipped with soft rail pad, e. g. Zw 1000.

4) Sensitivity analysis using theoretical parameter variations (not "as built"):

Parameter variations were carried out on different components such as rail pad vertical stiffness (based on Zw 1000 but using factor 0.5 to 1), tension clamp preload (from 10 kN to 30 kN) and fastening system lateral stiffness (angle guide plate + rail pad assembled + tension clamp from 20 kN/mm to 70 kN/mm) for laboratory scenario category C (see chapter 7.1.3).

The lateral rail head displacement (lateral rail movement and rail rotation) changes the rail contact geometry which is affecting the **running behavior of the rail vehicle** dependent on the track geometry and the track geometry quality (here: track alignment).

Track geometry quality level ERRI low is applied to all simulations representing good quality of conventional ballasted tracks. The vehicle running performance is evaluated by the level of lateral axel box accelerations.

The general observations are that a fastening system with low lateral stiffness (e. g. soft pad and soft angle guide plate) helps to reduce the lateral axle box accelerations, while a low rail rotational stiffness (e. g. by low/moderate clamping force) is increasing the lateral accelerations:

1) Tight curve and moderate speed:

   Using the scenario Redl/Zipf-Vöcklamarkt, a track section equipped with 4 different track designs (different fastening systems and sleepers with/-out under sleeper pads) along a radius R = 799m, cant u = 160 mm and train-speed V = 120 km/h (therefore cant deficiency uf ≈ 53 mm; lateral acceleration a ≈ 0,34 m/s²) the lowest calculated lateral axle box acceleration level, RMS a_{lat} = 1.19 m/s² is along the section with Zw 1000 + Skl 21 (soft pad in combination with tension clamp preload 2x10 kN = 20kN) compared to (see chapter 7.2):

   Zw 687 + Skl 14: 1.31 m/s²

   Zw 700 + Skl 28: 1.30 m/s²

   Zw 700 + Skl 14: 1.29 m/s²

2) Critical speed

   The non-linear critical speed represents the theoretically determined speed limit along straight track based on the actual wheel – rail interaction (one of the methods based on [44] was used). The sensitivity analysis shows:

   The increasing of the tension clamp preload is decreasing the rail rotation which is beneficial for the critical speed, e.g. 282 km/h using a theoretical tension clamp pre-load of 2x5 kN =10 kN applied and 324 km/h when the tension clamp preload is 2x16 kN = 32 kN on a pad ZW 1000 (see chapter 7.4).

   The change of lateral stiffness of the fastening system (angle guide plate + assembled rail pad + tension clamp) in a range of 5 kN/mm to 80 kN/mm shows a maximum critical speed (optimum) dependent on the vertical stiffness of the pad, e.g.

   - Stiff rail pad (ZW 687): optimum lateral fastening stiffness 30 kN/mm

   - Soft rail pad (ZW 1000): optimum lateral fastening stiffness 40 kN/mm

The **vehicle-track dynamic model** itself can calculate the wheel-rail contact forces, wear, the points of load attack, the load distribution and the vehicle accelerations (vertical/lateral) under consideration of the superstructure stiffness (vertical and lateral).

The rail head lateral displacement (lateral movement and rail rotational) influences the lateral load distribution. With respect to the required control of rail head lateral displacement (vehicle running behaviour, see above) the following conclusions can be drawn:

1) On the straight track or track with large curve, both the lateral wheel/rail contact force and the corresponding lateral resistance force of the fastening system (without contact between rail foot and angle guide plate) are low. The vehicle is usually travelling with a higher speed. The influence of the fastening lateral stiffness on the dynamic effect of the vehicle is the critical point and is investigated in chapter 7.4 to study the critical vehicle speed with the theoretical maximal vehicle speed.

   In the case of the tight curve (defined in DIN EN 13481), the lateral wheel/rail contact force is large, the corresponding lateral fastening resistance also increases significantly due to the contribution of the angle guide plate. The permissible vehicle speed is slow. The rail lateral movement and the corresponding load distribution on the superstructure are the critical points (see chapter 7.3).

2) On the tight curve, using a stiff rail pad (e. g. Zw 687 instead of Zw 1000) is one of the most effective measures to limit the rail head lateral displacement, but this comes with a limitation of the vertical and lateral load distribution. A favourable solution could be the use of a medium-stiff rail pad (e. g. Zw 700) in combination with a higher tension clamp preload, e.g. Skl 28 (preload of 2 x 14 = 28 kN), in narrow curves as done e. g. by ÖBB (see chapter 7.3).

3) The rail head lateral displacement along the track is highest near the connection point of the transition and the curve itself. This is caused by the change in curvature in combination with the vehicle response dependent on the individual vehicle configuration and speed. In case of using a special fastening system along the radius it should be also installed along the transition (see chapter 7.3).

4) The angle guide plate acts in the lateral direction and plays an essential role in the lateral movement of the rail. A higher lateral stiffness of the angle guide plate is reducing the lateral load distribution by the rail, but limiting the lateral rail movement. Based on the simulation results and the practical experience of e.g. the ÖBB infrastructure, a lateral angle guide plate stiffness of about 50 kN/mm can be suggested

along the curve, which realises a limited lateral rail movement but a sufficient load distribution (see chapter 7.3).

Additional conclusions are obtained from the investigation of the lateral sleeper support stiffness:

5) According to [12] [18] [19] [20] [46], a range of sleeper lateral stiffness from 25 kN/mm to 40 kN/mm under axle load is given. Using 40 kN/mm [19], the elastic sleeper lateral displacement determined by the vehicle-track dynamic model corresponds to the field measurements performed along the radius of the Redl-Zipf track section (see chapter 7.2).

6) A soft lateral sleeper support stiffness (25 kN/mm) is beneficial for the lateral axle box acceleration compared to a stiff one (40 kN/mm). However, the effect on the elastic sleeper-track resistance needs to be considered (see chapter 7.2).

References

[1]. DIN EN 13481-2 (2012). Railway application – Track - Performance requirements for fastening systems – Part 2: Fastening systems for concrete sleepers; German version EN 13481-2:2012.

[2]. Freudenstein, S.; Zhang, J.; Lechner, B. (2020). Technical Report TU Munich No.4044 (not published).

[3]. SIMPACK Documentation Version 2018 (2017).

[4]. ANSYS Documentation Version 19 (2018).

[5]. Knothe, K., & Stichel, S. (2003). Schienenfahrzeugdynamik. Berlin: Springer.

[6]. Kurzeck, B. (2003). Analyse des lateralen Schwingungsverhaltens eines Nahverkehrs-Triebfahrzeugs unter Komfortgesichtspunkten. ZEV Rail Glasers Annalen, 127 (8), 358-368

[7]. Polach, O. (2007). Berührgeometrie Rad/Schiene und Fahrzeugauslegung im Hinblick auf Stabilität. ZEV Rail Glasers Annalen 131 (9), 359-359.

[8]. Polach, O. (2006). Comparability of the non-linear and linearized stability assessment during railway vehicle design. Vehicle System Dynamic, 44 (sup1), 129-138.

[9]. Zhai, W. (2007). Vehicle-track coupling dynamics. Science Press, China, 6, 11-13.

[10].Auer, F. (2010). Zur Verschleißreduktion von Gleisen in engen Bögen, Dissertationsschrift, Wien.

[11].Liu, D. (2015). The influence of track quality to the performance of vehicle track interaction (Doctoral dissertation, Technische Universität München).

[12].Liu, J. (2013). Einfluss der Schienenbefestigungskomponenten auf das laterale Verformungs- und Lastverteilungs-verhalten der Schiene (Doctoral dissertation, Technische Universität München).

[13].Freudenstein, S., Zhang, J., & Mack, J. (2014). Field Measurement at Rothenthurm (CH) for Input Data of Simulation Model and Model Validation; Research Report 3493 of Institute of Road, Railway and Airfield Construction (not published).

[14].Zemp, A., & Kurt, E. (2015). Bericht zur Messung an Testgleis TUM (not published).

[15].Freudenstein, S., Zhang, J., & Mack, J. (2018). Modularer Workflow zur Modellierung der Dynamik von Oberbausystemen und dessen Validierung. ZEV Rail, (4), 132-137.

[16].Zhang, J., Lechner, B., Freudenstein, S., Wunderli, J.M., Zemp, A., Hannema, G., & Hecht, M. (2020). Development of numerical model for the design of low-noise ballasted track. International Journal of Transport Development and Integration, 4(2), 179-189.

[17].Freudenstein, S., Illiev, D., & Stahl, W. (2013). Querverschiebewiderstandsmessungen an un-und besohlten Schwellen. EI-Der Eisenbahningenieur, S-20.

[18].Klugar, K. (1976). Der statische Querverschiebewiderstand des belastetet Gleises. ETR-Eisenbahntechnische Rundschau, 25(4), 211.

[19].Gong, C. (2013). The Interaction between Railway Vehicle Dynamics and Track Lateral Alignment. Doctoral thesis, University of Huddersfield

[20].Kish, A., Samavedam, G., & Wormely, D. (2004) Fundamentals for Track Lateral Shift for High Speed Rail Applications. National Technical Service.

[21].Steger, M.V. (2017). Untersuchungen zum Schwingungsverhalten und der daraus resultierenden Beanspruchung von Spannklemmen für Schienenbefestigungen unter Berücksichtigung von hochfrequenten Anregungen. (Doctoral dissertation, Technische Universität München).

References

[22]. Tian, F. (2016). Integration of the Fastening System into the Railway Superstructure Model and Validation under Static and Dynamic Loading. (Master's thesis, Technische Universität München, not published)

[23]. Polach, O. (2018). Simulationstechnik in der Schienenfahrzeugdynamik, Vorlesungsskript TU Berlin, ILS

[24]. US Department of Transport, Federal Railroad Administration (FRA DOT), Track Safety Standards, 49 CFR part 213 (2002)

[25]. Report China Changsha Rail Institute 1985

[26]. Report China Peking Rail Institute 1999

[27]. Frederich, F. (1984). Die Gleislage aus fahrzeugtechnischer Sicht. ZEV-Glasers Annalen, 108-1984.

[28]. DIN EN 14363 (2005). Bahnanwendungen – Fahrtechnische Prüfung für die fahrtechnische Zulassung von Eisenbahnfahrzeugen.

[29]. UIC 518 (2009). Fahrtechnische Prüfung und Zulassung von Eisenbahnfahrzeugen – Fahrsicherheit, Fahrwegbeanspruchung und Fahrverhalten.

[30]. Wikipedia: CAD Computer-Aided Design

[31]. Wikipedia: Finite Elements Method

[32]. SIMPACK Documentation Version 8904 (2009, SIMPACK AG).

[33]. DIN EN 12299 (2009). Railway Applications-Ride comfort for passengers – Measurement and evaluation; German version.

[34]. Sperling, E. (1941). Verfahren zur Beurteilung der Laufeigenschaften von Eisenbahnwesen. Organ für die Fortschritte des Eisenbahnwesens, 12, 176-187.

[35]. DBS 918 235:2017. Elastische Zwischenlagen und Zwischenplatten von Schienenbefestigungssystemen

[36]. Bösterling, W. (2010). Elastische Gleise für hohe Geschwindigkeit. Der Eisenbahningenieur (Hamburg), 61(4), 26-30.

[37]. DIN EN 13674-1 (2001). Railway applications -Track-Rail-Part 1: Vignole railway rails 46kg/m and above. German version EN 13674-1:2001.

[38]. Than, P. (2018). Modelling of the Fastening System for the Analysis of the Lateral Rail Displacement. (Master's thesis, Technische Universität München, not published).

[39]. Vossloh Fastening System GmbH. System W 14, highly elastic rail fastening for high speed and conventional rail, the established solution for ballasted track with concreted sleepers.

[40]. Freudenstein, S.; Zhang, J.; Lechner, B. (2018). Technical Report TU Munich No.3820 (not published).

[41]. Xiao, Jun (2012): Laterale Lastverteilung des Schottergleises. Masterarbeit. Technische Universität München. Lehrstuhl für Verkehrswegebau. (Master's thesis, Technische Universität München, not published).

[42]. Zhang, J. (2019): Fahrzeugdynamische Simulationsgrundlagen eines Triebzuges für den InterCity-Verkehr. (Diplomarbeit, Technische Universität Berlin, not published).

[43]. Weidemann, C., Matthias, A., & Zhang, J. (2013). SIMPACK Rail Training Material, Gilching, Germany.

[44]. Polach, O. (2006). On non-linear methods of bogie stability assessment using computer simulations. Proceedings of the Institution of Mechanical Engineers, Part F: Journal of Rail and Rapid Transit, 220(1), 13-27.

[45]. DB Richtlinie 800.0110, 01.08.2009: Netzinfrastruktur Technik entwerfen; Linienführung

[46]. Iwnick, S. (1998). Manchester benchmarks for rail vehicle simulation. Vehicle System Dynamics, 30 (3-4), 295-313.

[47]. ORE-B55 (1983). Entgleisungssicherheit von Güterwagen in Gleisverwindungen. Bericht Nr. 8 (Schlussbericht), Utrecht.

[48]. DIN EN 13481-1 (2012). Railway application – Track - Performance requirements for fastening systems – Part 1: Definitions; German version EN 13481-1:2012.

List of Figures

List of Figures

121

List of Tables

List of Abbreviations

APDL	ANSYS Parametric Design Language
CAE	Computer Aided Engineering
CAD	Computer Aided Design
DOF	Degree of Freedom
ERRI	European Rail Research Institute
FBI	Flexible Body Input
FEA	Finite Element Analysis
FEM	Finite Element Method
IGES	Initial Graphics Exchange Specifications
IRM	Inertia Relief Mode
L/V	Ratio of Lateral force over Vertical force
MBS	Multibody Simulation
MDOF	Master of Degree of Freedom
PSD	Power Spectral Density
RMS	Root Mean Square
STEP	Standard for the Exchange of Product Model Data
USP	Under-sleeper pad

Definition of Symbols

Term	Unit	Definition
A	mm^2	Area of rail section
E	MPa	Yong's Modulus
F_e:	kN	Elastic resistance
F_p:	kN	Peak resistance
I	cm^4	Area Moment of inertia
Ixx	cm^4	Area Moment of inertia of section about x-axis
Iyy	cm^4	Area Moment of inertia of section about y-axis
W_p:	mm	Displacement at peak
W_e:	mm	Elastic displacement

Appendices

This document included all the appendices. They are numbered from 1 to 10
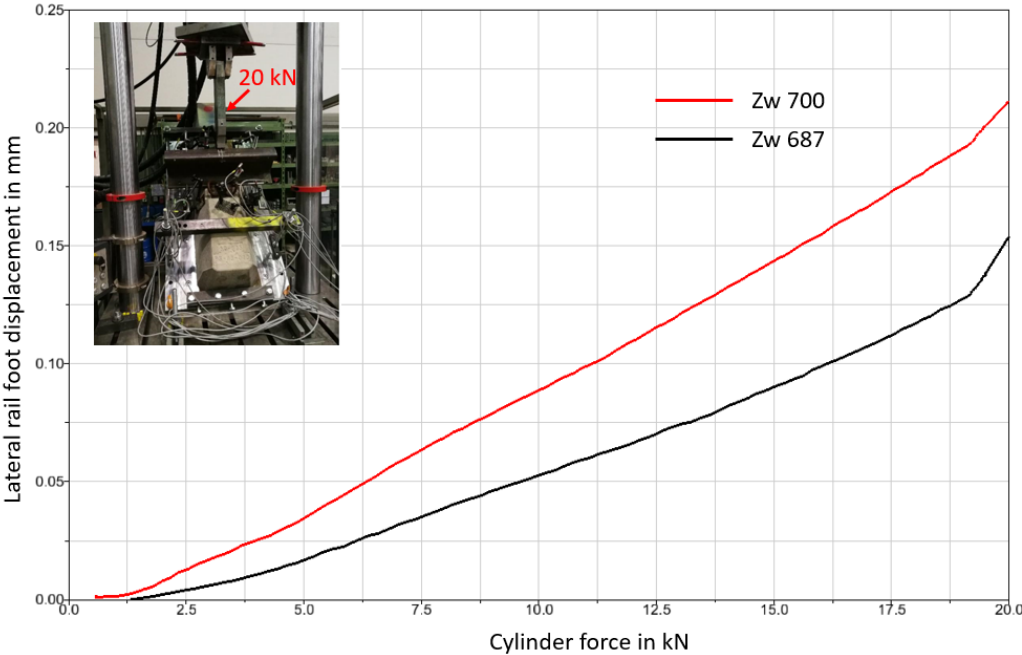
Figure: Rail foot lateral displacement vs cylinder load under different rail pad types
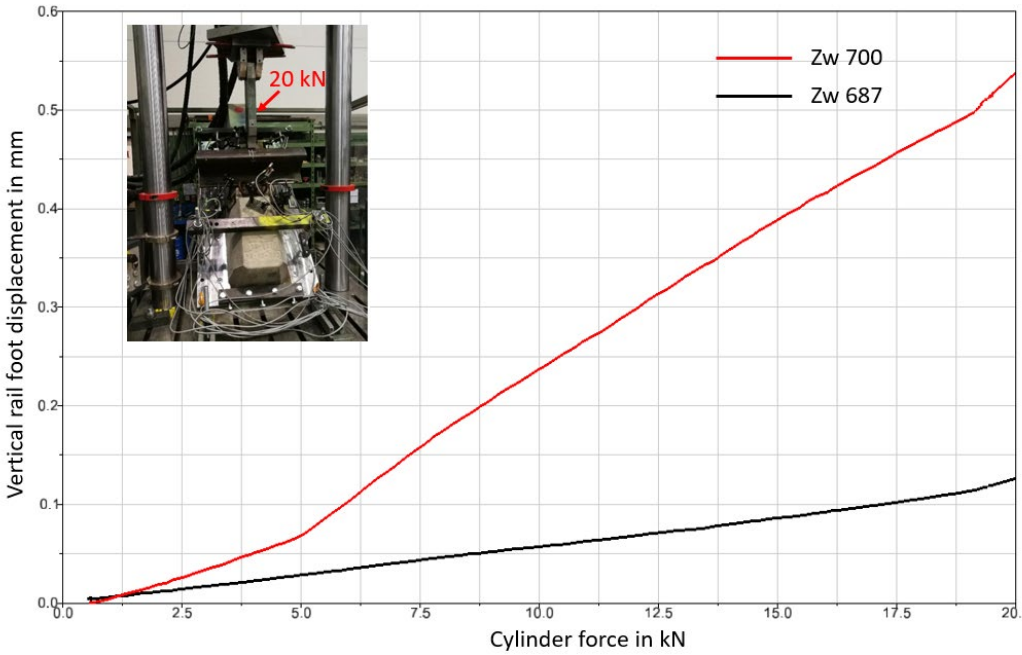

Figure: Rail foot vertical displacement vs cylinder load (field side) under different rail pad types
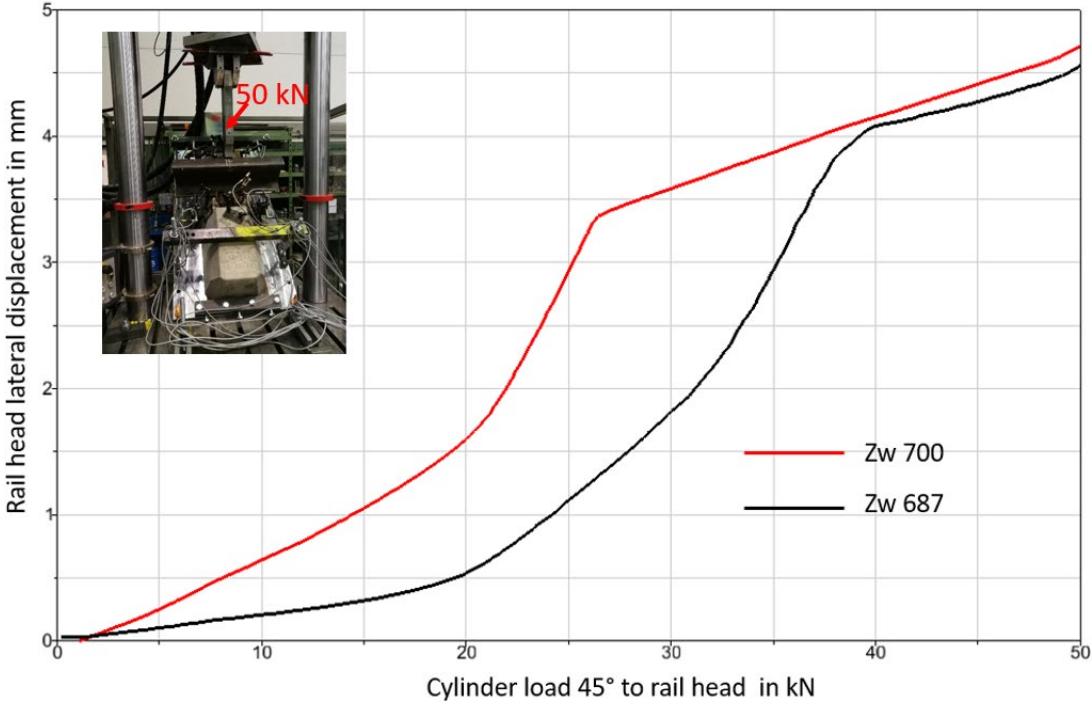
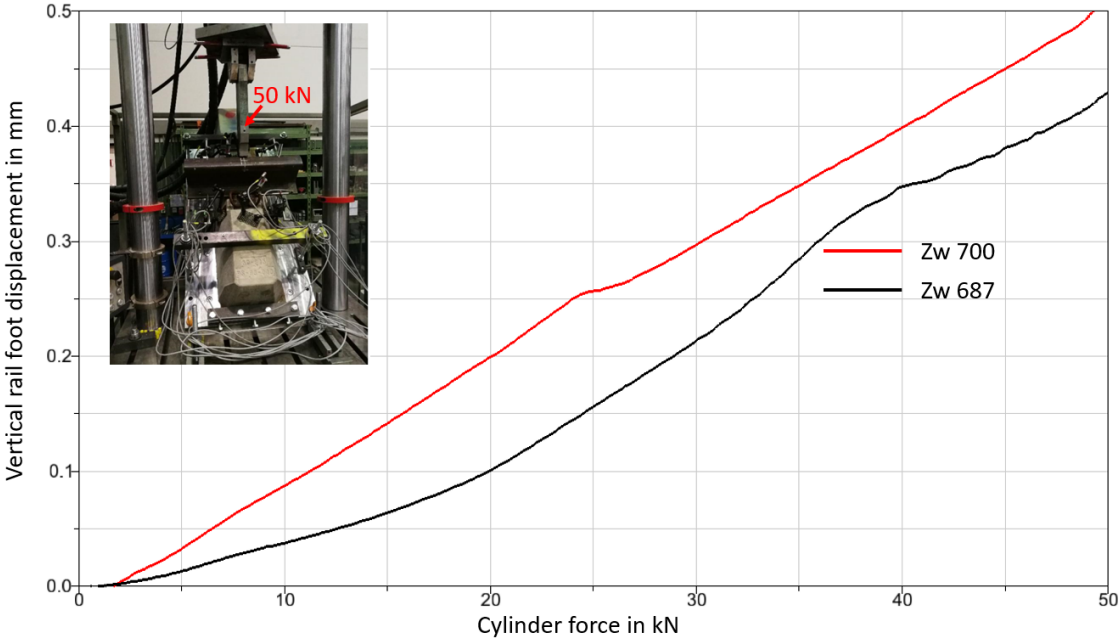**Figure: Rail head lateral displacement vs cylinder load under different rail pad types**

Figure: Rail foot lateral displacement vs cylinder load under different rail pad types
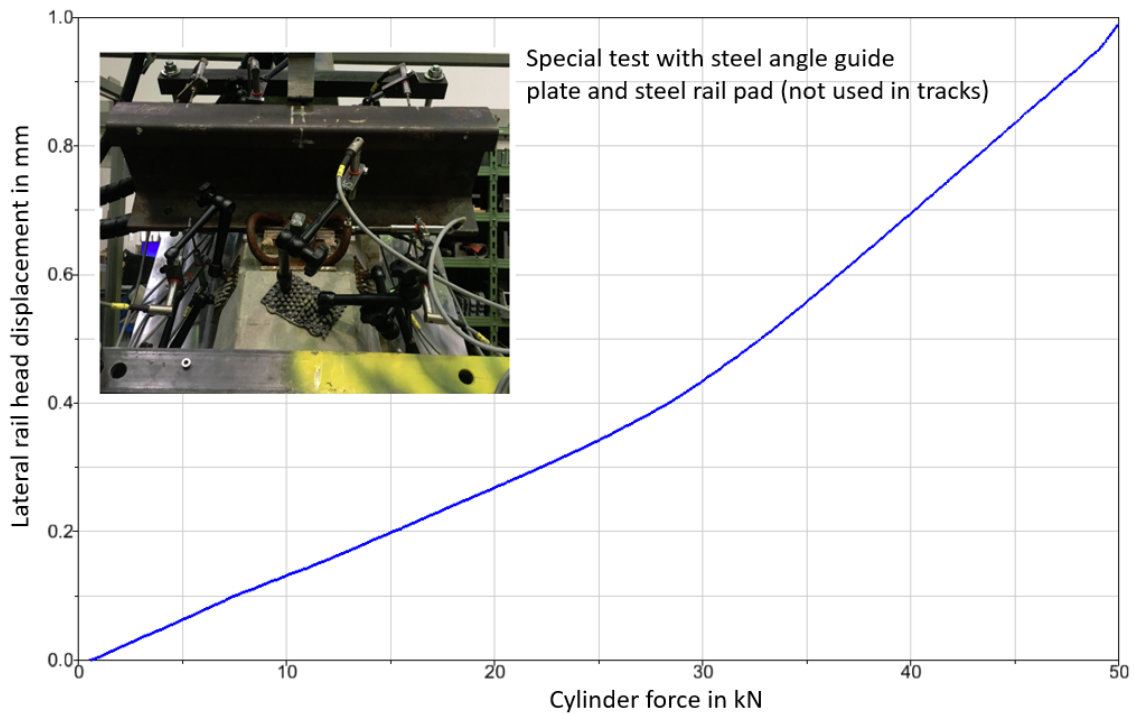
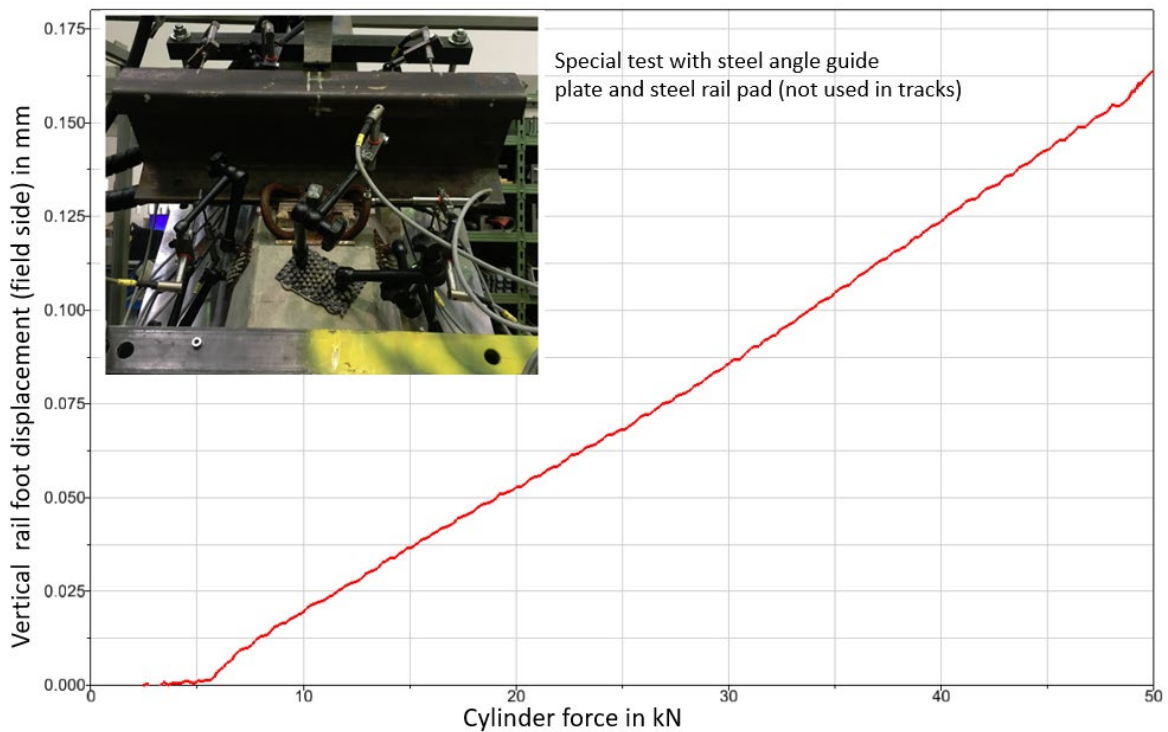**Figure: Rail head lateral displacement vs cylinder load under steel angle guide and steel rail pad**

Figure: Rail foot vertical displacement vs cylinder load (field side) under steel angle guide and steel rail pad
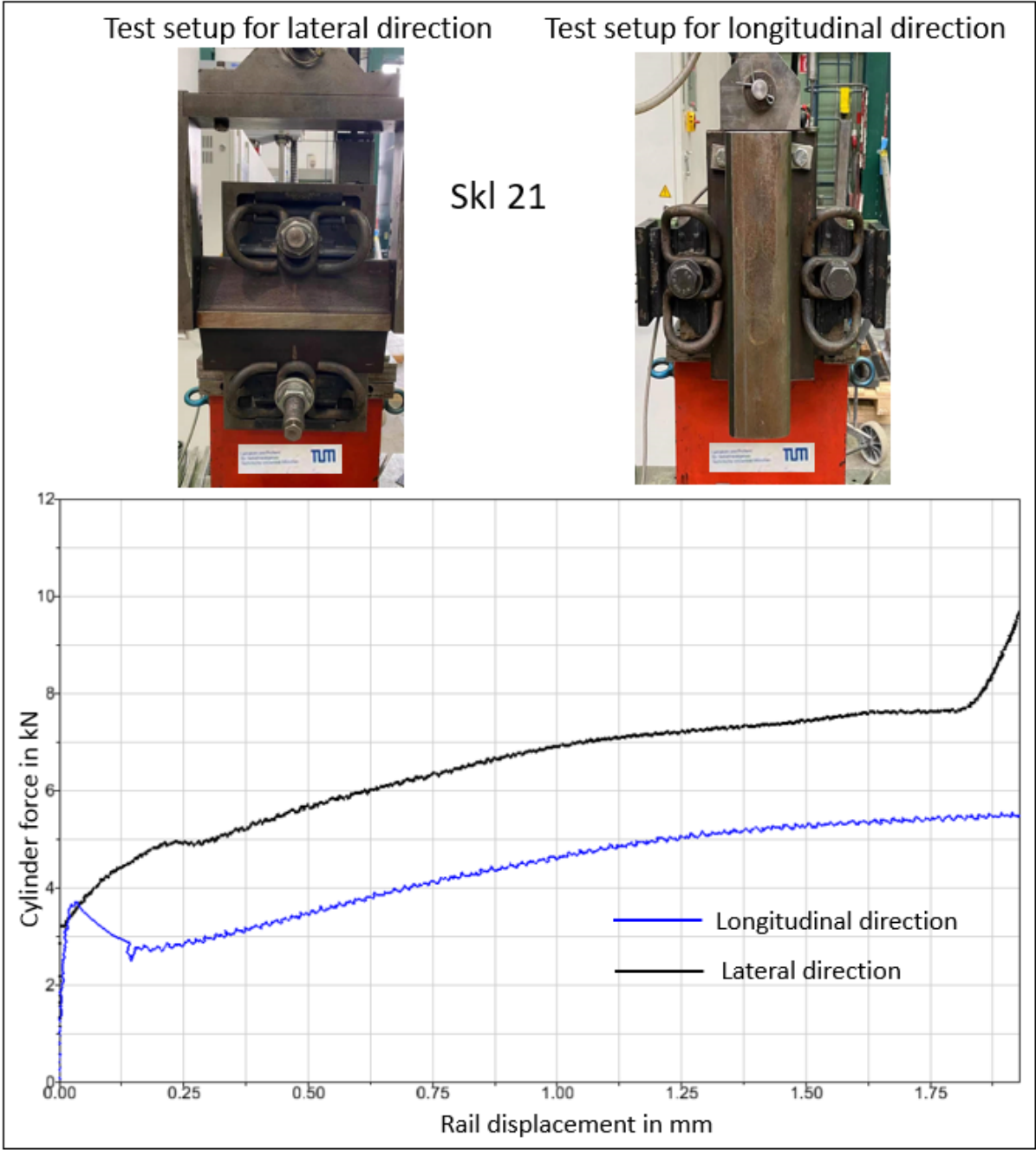
Figure: Rail displacement vs cylinder load in lateral and longitudinal direction of fastening system Skl 21 with milled angle guide plate
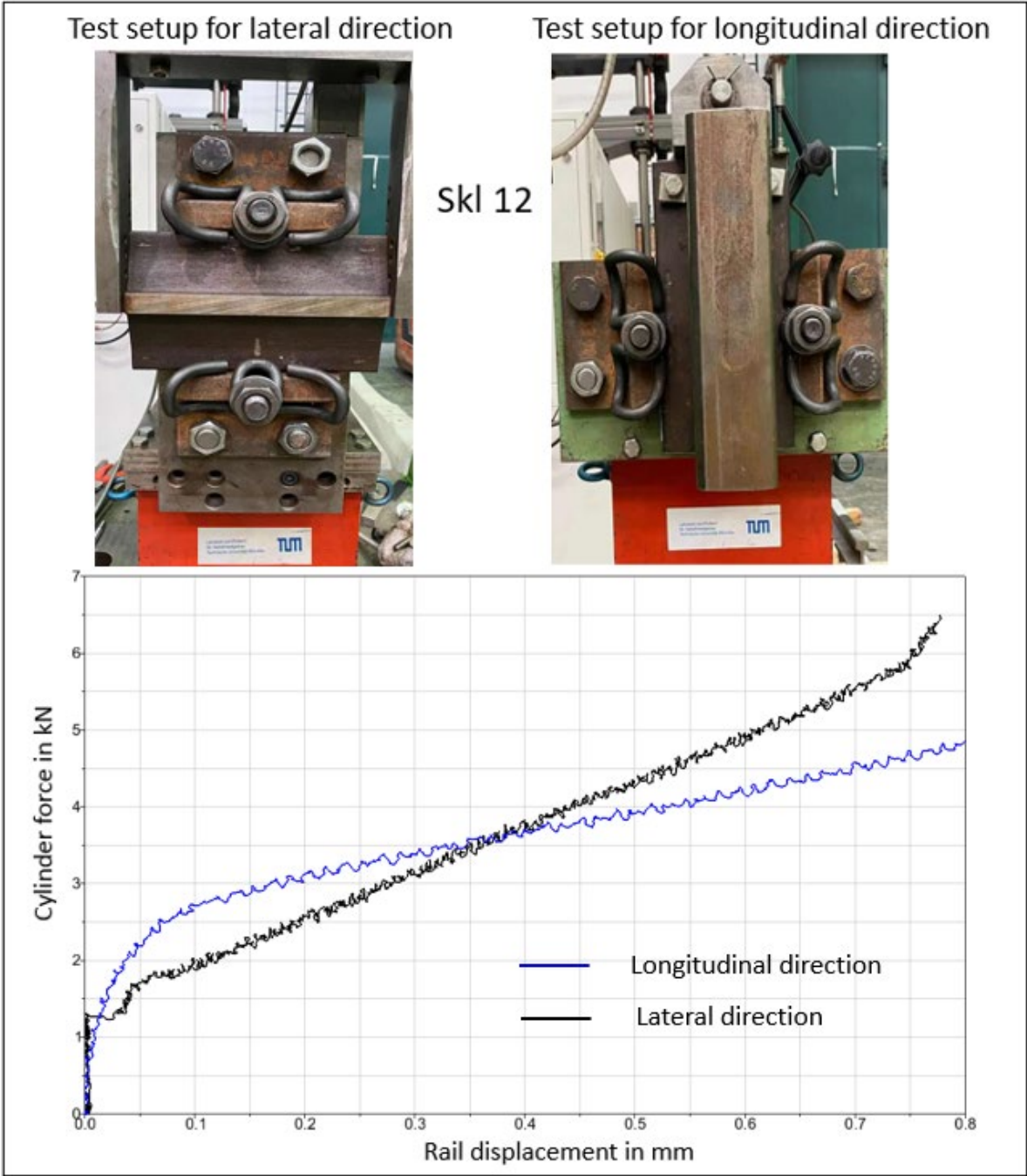
Figure: Rail displacement vs cylinder load in lateral and longitudinal direction of fastening system Skl 12
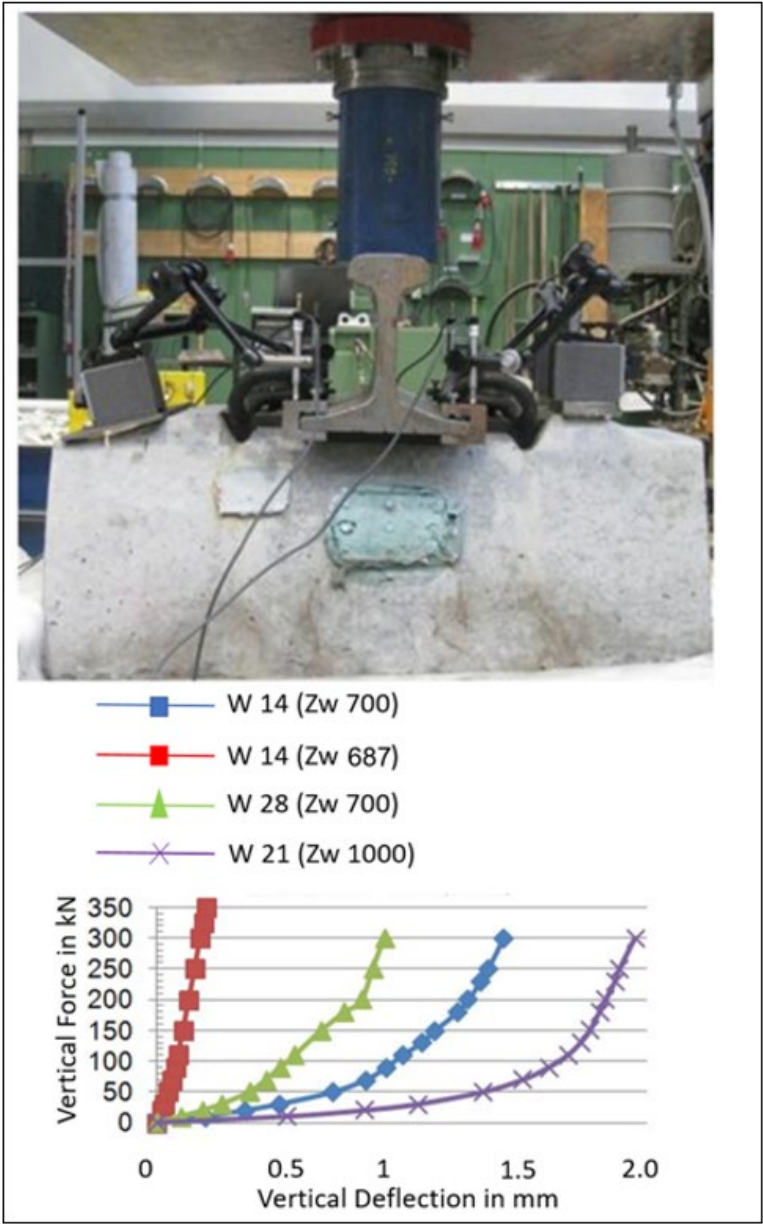
Figure: Non-linear rail pad stiffness in assembled state under vertical loading [12]

Appendix 7

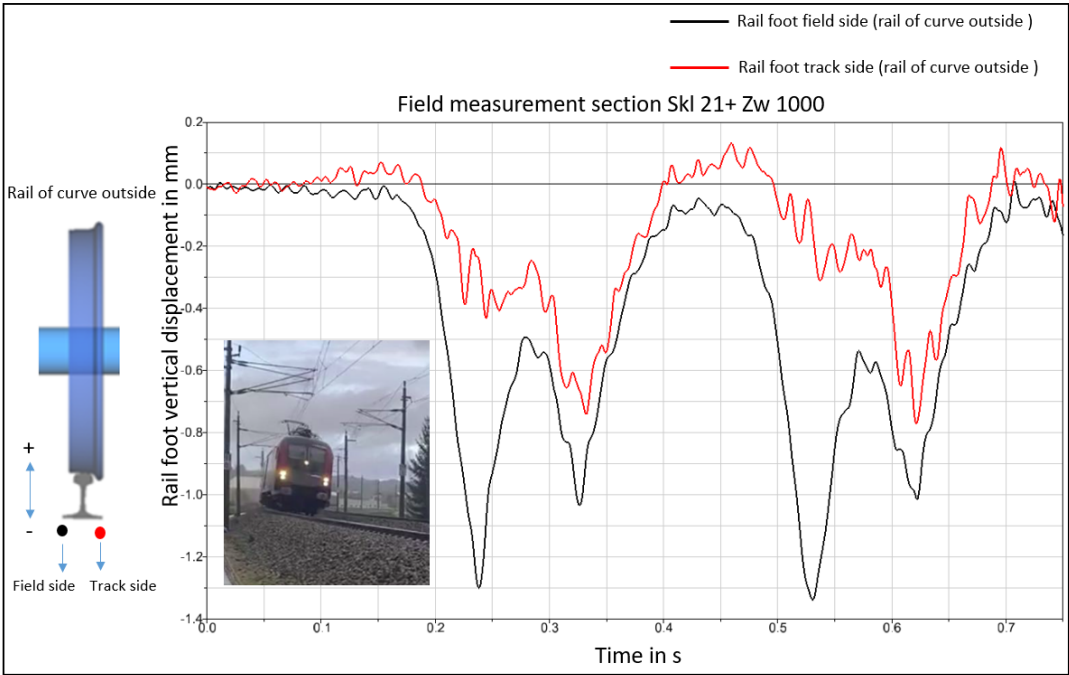**Figure: Rail foot vertical displacement measurement section Skl 21 + Zw 1000**

Figure: Rail foot vertical displacement measurement section Skl 21 + Zw 687
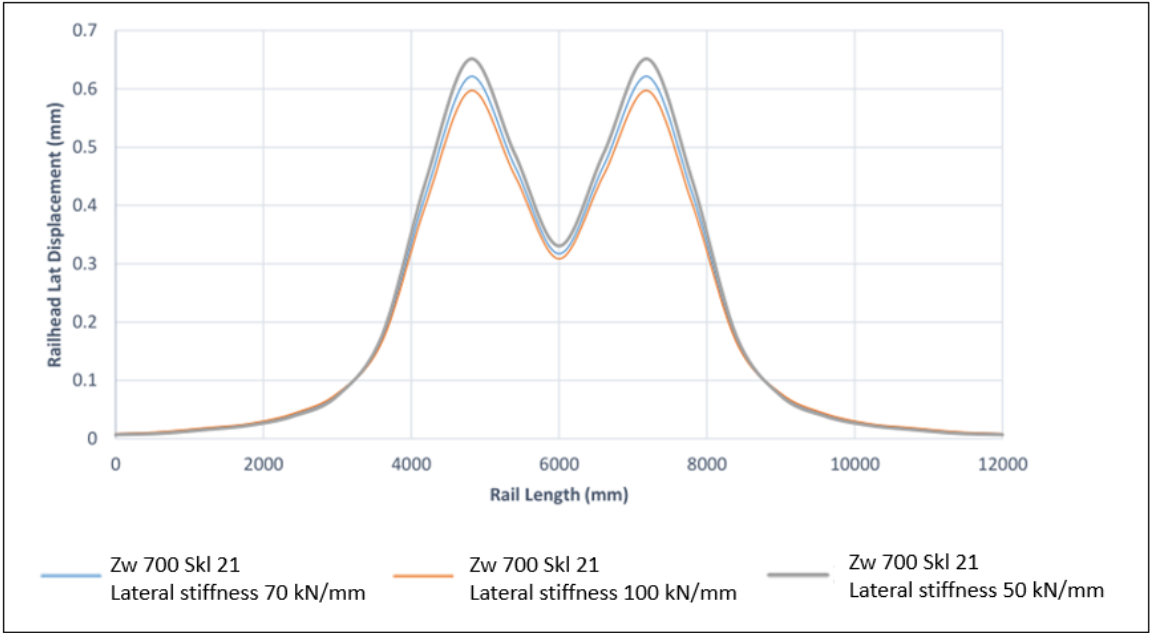
Appendix 8

Figure: Rail head lateral displacement of 12 meters rail section with Skl 21 under different lateral stiffness
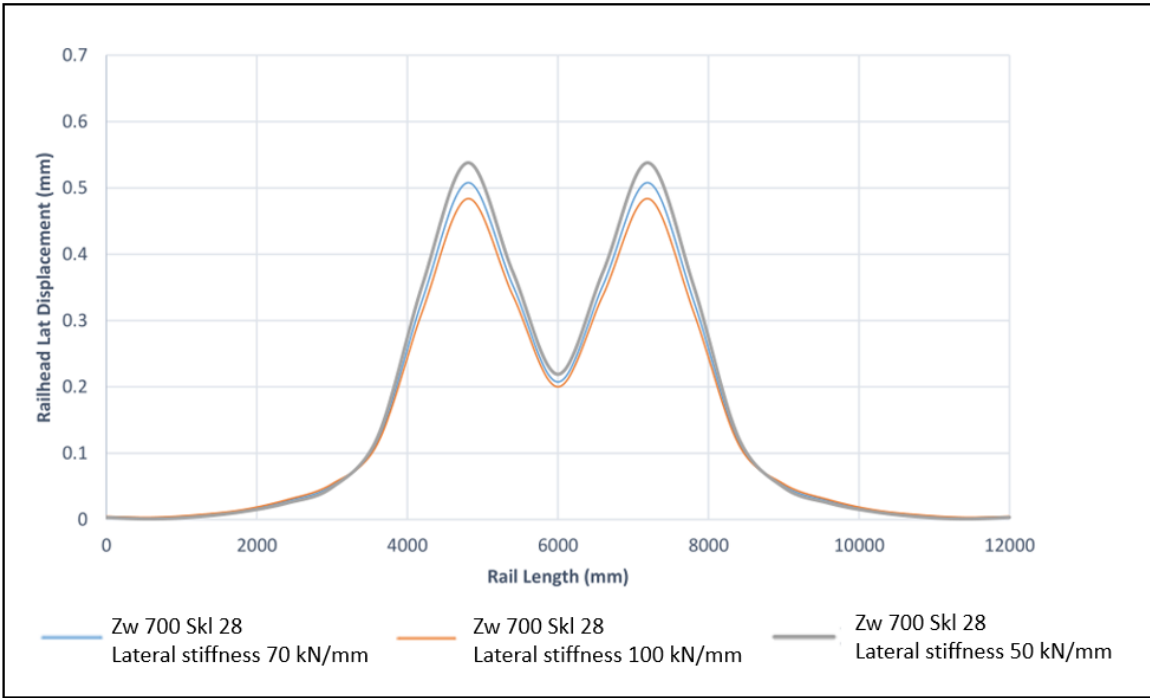

Figure: Rail head lateral displacement of 12 meters rail section with Skl 28 under different lateral stiffness

Appendix 9

Table: Average mean value of wheel/rail contact forces track scenario Redl/Zipf-Vöcklamarkt

	Skl 21+Zw 1000		**Skl 21 + Zw 687**	
	RMS Value in kN		**RMS Value in kN**	
Wheelset 1, wheel right	Y	18.33	Y	18.39
(curve outside)	Q	113.56	Q	113.54
Wheelset 1, wheel left	Y	-12.62	Y	-12.61
(curve inside)	Q	98.98	Q	98.93
Wheelset 2, wheel right	Y	7.37	Y	7.39
(curve outside)	Q	112.17	Q	112.11
Wheelset 2, wheel left	Y	5.14	Y	5.08
(curve inside)	Q	100	Q	100
Wheelset 3, wheel right	Y	16.73	Y	16.71
(curve outside)	Q	113.17	Q	113.13
Wheelset 3, wheel left	Y	-12.37	Y	-12.34
(curve inside)	Q	99.26	Q	99.23
Wheelset 4, wheel right	Y	8.38	Y	8.47
(curve outside)	Q	112.10	Q	112.06
Wheelset 4, wheel left	Y	5.22	Y	5.13
(curve inside)	Q	99.90	Q	99.90

Table: Average mean value of wheel/rail contact forces track scenario DIN EN 13481-2 category E

		Skl 21+Zw 1000 RMS Value in kN		Skl 14 + Zw 687 RMS Value in kN
Wheelset 1, wheel right (curve outside)	Y	73.17	Y	72.96
	Q	200	Q	199.95
Wheelset 1, wheel left (curve inside)	Y	-39.7	Y	-39.7
	Q	154.32	Q	154.36
Wheelset 2, wheel right (curve outside)	Y	4.79	Y	5.1
	Q	176.97	Q	176.93
Wheelset 2, wheel left (curve inside)	Y	-23.22	Y	-24.58
	Q	175.13	Q	175.1
Wheelset 3, wheel right (curve outside)	Y	62.75	Y	62.56
	Q	197.03	Q	196.92
Wheelset 3, wheel left (curve inside)	Y	-41.78	Y	-41.78
	Q	157.61	Q	157.61
Wheelset 4, wheel right (curve outside)	Y	8.58	Y	9.8
	Q	179.72	Q	179.68
Wheelset 4, wheel left (curve inside)	Y	-17.95	Y	-19.16
	Q	171.5	Q	171.48